UNIVERSITÀ DEGLI STUDI DELL'INSUBRIA

Dipartimento di Scienza e Alta Tecnologia

Academic Year 2023-2024

Master Degree in Physics

DEVELOPMENT OF COMPACT ELECTROMAGNETIC CALORIMETERS WITH ORIENTED CRYSTALS: STORM 2022 *BEAMTEST*

Author: Leonardo Perna
Matricola: 737628

Supervisor:	Prof.ssa Michela Prest Università degli Studi dell'Insubria
Co-Supervisor:	Dott.ssa Alessia Selmi Università degli Studi dell'Insubria

Science cannot solve the ultimate mystery of nature.
And that is because, in the last analysis, we ourselves are a part of the mystery that we are trying to solve.
Max Planck

Contents

Introduction

Crystal physics is a highly active and fascinating area of research; the study of the interaction between particles and crystal lattices not only offers the opportunity to investigate the structure of matter and the nature of the involved electromagnetic interactions, but also enables the development of next-generation devices for high energy physics.

The behavior of a particle crossing a crystal lattice is strongly related to its incidence angle; in fact, depending on the lattice-to-beam orientation, the crystal target can appear to the incident particle as an amorphous material (i.e. without any ordered structure) or as a periodic pattern of atoms (consisting in planes or strings of atoms). If a charged particle crosses some crystallographic direction with a small enough incidence angle, it may be trapped in these preferential channels, losing less energy and penetrating deeper in the oriented target material with respect to the not oriented ones. The first to notice this phenomenon was J. Stark, who published a paper in 1912 on the interaction between protons and crystal lattices. This phenomenon, later called channeling, was further investigated by Lindhard, who published an extensive work in the 1960s. He demonstrated, using a semiclassical treatment and introducing the potential well continuous approximation, that the crystal structure strongly modifies the electron (or positron) trajectory, forcing the particle to follow a periodic motion inside the lattice, if it impinges on the crystal axis or plane with an incidence angle not exceeding the Lindhard critical value. In the channeling condition, also the emitted radiation differs from the standard bremsstrahlung one, which occurs in amorphous materials. The periodic motion inside the lattice leads to the coherent emission of photons, whose features depend strongly on the charged particle initial energy: the spectrum nature varies from the electric dipole one, occurring when the incident electron or positron has a low initial energy ($\sim 100\,\mathrm{MeV}$), which leads to the emission of soft photons with quantized frequencies, to an undulator-like behavior for energies up to few GeV and finally, for higher energies, to a synchrotron behavior leading to the emission of hard photons.

For energies higher than few GeV, relativistic corrections have to be taken

into account; the interatomic electric field experienced by the impinging electron in its rest frame is enhanced by a factor γ (the Lorentz factor), thus reaching the Strong Field regime. In the SF regime also the pair production cross section is modified, leading to an increase in the pair production rate when the particle impinging the crystal lattice is a photon. As a net effect, the Strong Field regime leads to an enhancement in the energy deposit, and therefore to an acceleration in the electromagnetic shower development, that can be seen equivalently as a reduction of the radiation length X_0 of the crystal, in comparison with amorphous media.

This thesis work has been performed in the framework of the *STORM* (STrOng cRystalline electroMagnetic field) collaboration, whose main task was to study the acceleration of the electromagnetic shower in a $4.6X_0$ $PbWO_4$ crystal in the Strong Field regime, measuring directly the light output produced by the crystal under test.

In the first chapter of this thesis, a theoretical treatment of the effects induced by the crystal lattice on an impinging particle will be provided. After a brief introduction on the crystal structures, the channeling phenomena will be treated in detail. Then, the Standard Bremsstrahlung radiation emission process will be introduced, followed by the Coherent Bremsstrahlung one, induced by the lattice structure. The second part of the chapter focuses on the main topic of this thesis: the Strong Field regime. It will explain the underlying mechanisms that lead to the enhancement of photon emission for incident ultra relativistic electrons and positrons, as well as the increase of the pair production cross section in case of impinging high energy photons.

The second chapter will start with a brief introduction on calorimetry; in particular, the main parameters needed to characterize the energy containment of a calorimeter will be introduced. Moreover, it will be discussed how these fundamental parameters change in case of an oriented electromagnetic calorimeter, thus opening the way for the development of a compact next-generation electromagnetic calorimeter based on oriented crystals. Then, the experimental techniques, exploited by the collaborations preceding the *STORM* one, will be presented and their main results will be analyzed. In the second half of the chapter, several future applications of the crystal physics will be discussed, with a particular emphasis on the crystal-based calorimeters.

The third chapter will describe the beam facility and the experimental layout exploited during the *STORM 2022* beamtest, which took place on the CERN H2 extracted beamline. In the second part of the chapter, all the components of the experimental setup will be presented and their performances will be discussed in detail. Moreover, the main features of the $PbWO_4$ crystal samples will be introduced, as well as their light readout system based on Silicon PhotoMultipliers.

The fourth chapter will present the preliminary analysis. In the first part of the chapter, the beam angular divergence will be computed and the offline alignment of the two silicon microstrip telescopes, forming the tracking system, will be performed. Moreover, the last part of the setup, that is the calorimeter consisting of 7 lead glasses, will be calibrated and characterized in terms of lateral energy loss with the help of the Geant4 toolkit. In the end of the chapter, the beam purity will be analyzed.

The final chapter is dedicated to the $PbWO_4$ characterization as a function of the lattice-to-beam orientation, from the crystal alignment procedure to the study of the $PbWO_4$ response during the transition from the random to the axial orientation. The last part of the chapter focuses on the enhancement in the energy deposit due to the Strong Field effects and the consequent radiation length reduction.

Chapter 1

Crystal physics

When a beam of charged particles hits a solid target, many physical phenomena occur (e.g. ionization processes, electromagnetic radiation emission, Coulomb scattering) that modify the spatial and energy distribution of the incident beam. If the target material does not feature an ordered structure, such as a crystalline lattice, the physical processes are independent on the target orientation with respect to the beam and their cross section depends strongly on the density and the atomic number of the material, as well as on the incident energy.

On the other hand, if the solid exhibits a periodic structure (e.g. crystalline lattice), the beam trajectory and the energy loss distribution become strongly dependent on the lattice-to-beam orientation. J. Stark in 1912 realized that there are privileged channels in crystalline materials where protons and heavy ions can pass through and stop at much deeper depths, compared to amorphous materials (i.e. the ones without an ordered and periodic structure). This phenomenon, called channeling, occurs because the charged particle undergoes small-angle collisions losing a smaller amount of energy.

This discovery led the scientific community to wonder how a beam of charged particles interacts with an ordered crystalline structure. In the 1960s Lindhard published an extensive work on this topic [1], demonstrating that charged particles impinging on a crystalline medium with a small angle with respect to the crystallographic directions (planes or axes), can be trapped in these specific crystalline channels. In particular, the periodic interatomic potential of the crystal lattice modifies strongly the particle trajectory.

Moreover, a particle decelerating by means of the electromagnetic interaction with the solid atoms, emits electromagnetic radiation via bremsstrahlung. If the target material is amorphous, the resulting photon spectrum is the sum of the uncorrelated interactions with the solid atoms. In presence of a crystalline target, also the radiation spectrum is affected; the contributions

from individual collisions with atoms can coherently sum leading to a high intensity emission of photons with specific energies. Depending on the initial particle energy, different physical processes can occur, resulting in the emission of channeling radiation and coherent bremsstrahlung [2]. For light particles such as electrons, the coherent effects increase the probability of photon emission and consequently the bremsstrahlung cross section [2]. These effects can be explained in the framework of classical physics for energies in the MeV - few GeV range. For higher energies, relativistic corrections are needed. In fact, the electric field experienced in the rest frame of the incident particle is increased by a factor γ (the Lorentz factor), and the Strong Field regime (SF) is reached [3].

In the Strong Field regime, an electron interacting with the lattice emits synchrotron radiation with a high intensity in the hard part of the spectrum. The SF effect modifies also the pair production process for an impinging photon, despite its charge neutrality, resulting in an enhancement of the pair production cross section. The enhancement in the photon radiation and pair production modifies the electromagnetic shower development in a crystalline material oriented with the beam direction, resulting in a reduction of the interaction length X_0 (the scale-length of the electromagnetic interactions between the incident particle and the atoms of the target, as it will be explained in subsection 1.3.1).

The first part of this chapter focuses on the crystalline structures and introduces the mathematical formalism of the Bravais lattices. In the second part of the chapter the channeling processes will be treated, with particular attention on the radiative loss phenomena for a charged particle in an oriented crystal. The third part of the chapter gives a theoretical background of the Strong Field effects, focusing on the enhancement of the radiative losses for charged particles and the pair production for photons.

1.1 The crystalline structures

Before studying the physical processes which occur in a crystal lattice, a formal treatment of the periodic crystalline structures is needed. A crystal is characterized by a highly periodic and ordered structure, called crystalline or Bravais lattice [4].

The crystalline structure is characterized by the symmetry under discrete spatial translation. The step of this discrete symmetry is defined by the unit crystal cell that constitutes the building block of the lattice; its extended repetition in space forms the crystalline periodic structure. The translation from one fundamental unit to another is defined by the following equation:

$$\boldsymbol{r} = a_1\hat{\boldsymbol{a}}_1 + a_2\hat{\boldsymbol{a}}_2 + a_3\hat{\boldsymbol{a}}_3 \tag{1.1}$$

where $(\hat{\boldsymbol{a}}_1, \hat{\boldsymbol{a}}_2, \hat{\boldsymbol{a}}_3)$ are the so called primitive vectors. They are unit vectors pointing at different directions, not necessarily orthogonal between themselves, and spanning the whole crystal structure. If the unit cell is not represented by three orthogonal versors, the versors themselves would not be linearly independent and thus the choice of $(\hat{\boldsymbol{a}}_1, \hat{\boldsymbol{a}}_2, \hat{\boldsymbol{a}}_3)$ would not be unique. The convention adopted here is the following: $\hat{\boldsymbol{a}}_1$ corresponds to the shortest lattice period, $\hat{\boldsymbol{a}}_2$ to the shortest period and not parallel to $\hat{\boldsymbol{a}}_1$, and $\hat{\boldsymbol{a}}_3$ to the shortest period and not coplanar with the first two unit vectors. (a_1, a_2, a_3) are integer numbers indicating the coordinates in the 3 dimensional space, spanned by the versors. Furthermore, equation 1.1 identifies all the nodes, i.e. the intersection points between one cell and another. All the possible nodes locations in the 3-dimensional space define up to 14 Bravais lattices [4].

In the crystal lattice, subsets of atoms with a periodic structure can be identified, as represented in figure 1.1 for the $PbWO_4$ case. Among these subsets it is possible to identify the crystal planes, whose geometrical locations are described by the following equation:

$$\frac{a_1}{\overline{a_1}} + \frac{a_2}{\overline{a_2}} + \frac{a_3}{\overline{a_3}} = 1 \tag{1.2}$$

where $\overline{a_1}, \overline{a_2}, \overline{a_3}$ represent the intersection points between the plane and the axes defined by the primitive vectors.

Since $a_i \in \mathbb{Z}, \forall i \in \{1, 2, 3\}$, equation 1.2 is satisfied if and only if $1/\overline{a_i} \in \mathbb{Q}, \forall i \in \{1, 2, 3\}$, i.e. if:

$$\frac{n}{\overline{a_1}} = h, \quad \frac{n}{\overline{a_2}} = k, \quad \frac{n}{\overline{a_3}} = l \tag{1.3}$$

with n, h, k and l integers. Under these conditions, equation 1.2 becomes [4]:

$$a_1 h + a_2 k + a_3 l = n \tag{1.4}$$

The (h, k, l) triplet describes the spatial orientation of the plane and varying the parameter n, all the parallel planes are found. In particular, (h, k, l) are called Miller indices [4] and the following notation is employed in this thesis:

- (h, k, l) denotes a plane, described by its corresponding Miller indices, according to equation 1.4;
- $[h, k, l]$ denotes an axis, namely the direction perpendicular to the corresponding (h, k, l) plane;

- $< h, k, l >$ indicates the set of all the axes identical to $[h, k, l]$, due to the symmetries of the crystal structure such as the invariance under rotation.

Figure 1.2 shows the Face Centered Cubic (FCC) lattice with some axes and planes highlighted.

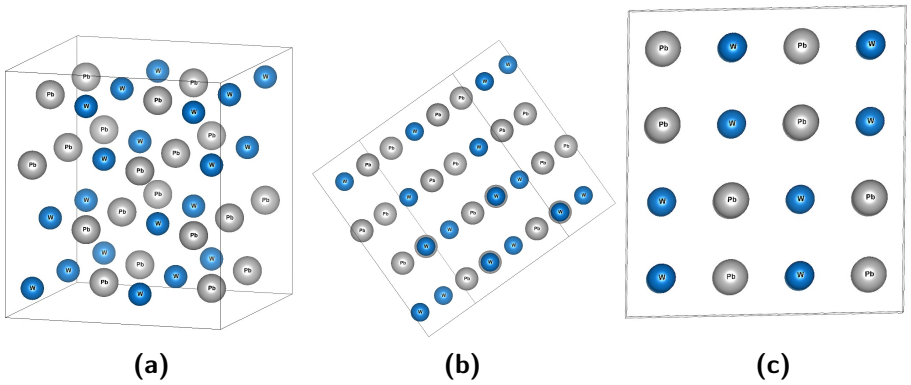

Figure 1.1: Three different points of view of the $PbWO_4$ crystal lattice: in (a) the lattice is arranged as an amorphous material, in (b) it is arranged in planes, in (c) in Pb and W strings. In the crystal lattice oxygen is neglected because its physical contribution to scattering processes is irrelevant [5].

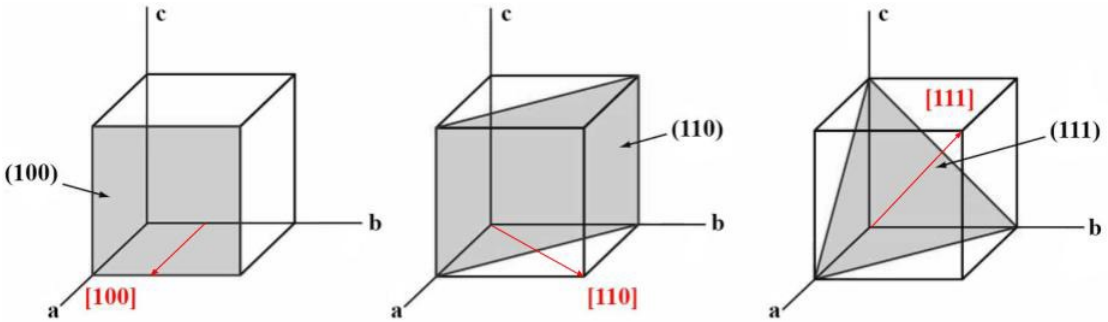

Figure 1.2: Face Centered Cubic (FCC) lattice with its main planes and axes, identified by the Miller indices [6].

1.2 The channeling effect

The existence of preferential channels along which charged particles can penetrate deeply into the material [3] is in clear disagreement with the well known behavior described by the Bethe-Bloch formula [7], for the energy deposit in an amorphous solid.

Lindhard explained in his work [1] that charged particles, entering at angles smaller than a certain critical angle, become trapped in a privileged channel formed by two crystal planes or two axes.

The charged particle whose trajectory remains channeled in a potential well interacts with fewer electrons than in an amorphous material, thus losing less energy and penetrating deeper in the material itself. In fact, the particle remains in the preferential channel (within certain limits that will be discussed in this section), undergoing many small-angle collisions with the scattering centers. Planar and axial channeling are treated below following Lindhard's footprints; both the physical phenomena will be treated in the continuous approximation in order to obtain an analytic expression for the interatomic potentials.

Furthermore, the channeling phenomenon is treated in a semiclassical framework. This is possible when the quantized energy levels reach the thermodynamic limit, i.e. when the occupation number N is $>> 1$. Since $N \propto \sqrt{M_\gamma}$, where M_γ is the relativistic mass of the incident particle, the semiclassical approximation holds for heavy ions at all energies. On the other hand, it remains reliable for lighter particles such as electrons for energies greater than 10-100 MeV [1].

1.2.1 Planar channeling

In the case of planar channeling, the interatomic potential in the continuous approximation, $U(x)$, depends only on the direction perpendicular to the $y-z$ plane and it is represented in figure 1.3. Its analytical expression is given by the following equation:

$$U(x) = N d_{pl} \int_{-\infty}^{+\infty} \int_{-\infty}^{+\infty} dydz \; V^{atom}(x, y, z) \tag{1.5}$$

where $V^{atom}(x, y, z)$ is the single atom potential, N the numerical density of atoms, d_{pl} the interplanar pitch and z the direction parallel to the plane. The potential $V^{atom}(x, y, z)$ takes also into account the interatomic screening effect. An explicit expression of this potential is given by the Fermi-Thomas formula [1]:

$$V(r) = \frac{Z_i Z e^2}{r} \Phi\Big(\frac{r}{a_{TF}}\Big) \tag{1.6}$$

where Ze is the particle charge, r the distance between the atom and the impinging particle, Z_i the crystalline atomic number, a_{TF} the Thomas-Fermi screening distance ($a_{TF} = 0.8853 a_B Z^{-1/3}$, with $a_B = 0.529$). Moreover, Φ is the screening function which takes into account the charge distribution of the atoms [1]:

$$\Phi\Big(\frac{r}{a_{TF}}\Big) = 1 - \Big(1 + \frac{3a_{TF}^2}{r^2}\Big)^{-1/2} \tag{1.7}$$

The effective planar potential, defined in equation 1.5, becomes:

$$U_{pl}(x) = 2\pi N d_{pl} Z_i Z e^2 (\sqrt{x^2 + 3a_{TF}^2} - x) \tag{1.8}$$

In the channeling condition, the transverse momentum component p_x is much smaller than the longitudinal one p_z. In fact, planar channeling occurs when $p_x/p_z \sim \theta \ll 1$, where θ is the angle between the plane direction z and the particle one, as shown in figure 1.3(a). In other words, the channeling regime is reached when the particle impinges onto the crystal almost parallel to the atomic planes.

A charged particle crossing two parallel planes at such small angles experiences the following potential:

$$U(x) \approx U_{pl}\Big(\frac{d_{pl}}{2} - x\Big) + U_{pl}\Big(\frac{d_{pl}}{2} + x\Big) - 2U_{pl}\Big(\frac{d_{pl}}{2}\Big) \tag{1.9}$$

Corrections due to thermal vibrations need to be added to equation 1.9 when the particle trajectory approaches the crystal plane. In that case atoms cannot be considered fixed but rather subject to thermal fluctuations.

In the channeling condition ($\theta \ll 1$), being E the total energy of the particle entering the crystal, the following relation holds:

$$E = \sqrt{p_x^2 c^2 + p_z^2 c^2 + m^2 c^4} + U(x) \approx E_z + \frac{p_x^2 c^2}{2E_z} + U(x) = E_z + E_x \tag{1.10}$$

where m is the particle mass, c the speed of light, p_x and p_z the transverse and longitudinal component of the momentum, $E_z = \sqrt{p_z^2 c^2 + m^2 c^4}$ and

$$E_x = \frac{p_x^2 c^2}{2E_z} + U(x) = \frac{p_z^2 \theta^2 c^2}{2E_z} + U(x) \tag{1.11}$$

For a motion in the potential $U(x)$, the energy longitudinal component E_z is conserved, thus the transverse energy E_x is conserved too. The conservation of the quantity E_x presented in equation 1.11 defines the particle trajectory in the (x, θ) plane; the trajectories are represented by a set of ellipses depending on the value of E_x. On the other hand, in the 3 dimensional space the particle motion is described by a helical trajectory, as shown in figure 1.4.

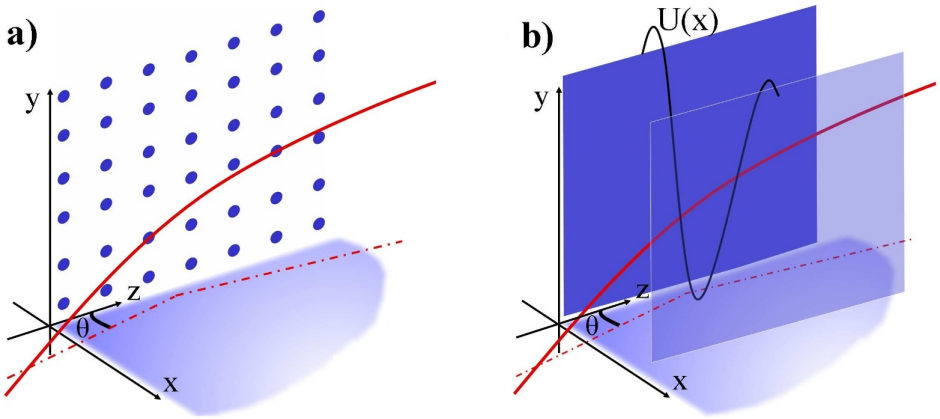

Figure 1.3: (a) Sketch of a particle crossing a crystallographic plane with a misalignment angle θ with respect to the longitudinal plane direction (z). (b) The particle is channeled by means of a potential well; the minimum is in the middle of the planes in case of positive charged particles [5].

Assuming the channeling condition $(p_x/p_z \ll 1)$, $E \approx E_z$, $p \approx p_z$ and the transverse energy becomes

$$E_x = \frac{pv\theta^2}{2} + U(x) \tag{1.12}$$

The condition for the capture of the particle into the channel is:

$$\frac{pv\theta^2}{2} + U(x) \leq U_0 \tag{1.13}$$

Assuming $U(x = 0) = 0$, the limiting angle, or Lindhard angle, of the capture is

$$\theta_L = \sqrt{\frac{2U_0}{pv}} \tag{1.14}$$

where U_0 is the potential well depth. For instance, for a (1,1,0) silicon crystal, the Lindhard angle is $\theta_L \sim 20\,\mu\text{rad}$ at $100\,\text{GeV}$ while $\theta_L \sim 7\,\mu\text{rad}$

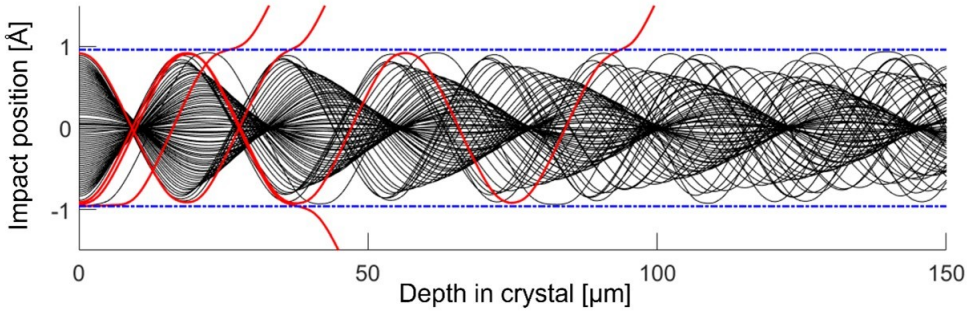

Figure 1.4: Monte Carlo simulation for a 180 GeV/c proton planar channeling. Blue lines indicate the atomic planes positions, black lines represent the channeled particles orbits and the red lines indicate the dechanneled particles [8].

at 1 TeV [9]. Equation 1.14 shows that the critical angle decreases as the square root of the energy; on the other hand the multiple scattering cross section decreases as the energy of the incoming particles [7]. This implies that the effects due to multiple scattering, which reduce the channeling efficiency, become less important at high energy.

The multiple scattering in fact can remove the particle from the channel as the particle approaches the crystal plane; the critical transverse position at which the multiple scattering becomes predominant is computed as $x = d_{pl}/2 - a_{TF}$. With this assumption the critical angle, above which the particle escapes from the channel, is computed as

$$\theta_c = \sqrt{\frac{2U_{max}}{pv}} \tag{1.15}$$

where U_{max} is the potential maximum, which is reached at the plane position itself ($x = d_{pl}/2$) for positive charged particles and in the midpoint between the two planes ($x = 0$) for negative charged particles (figure 1.5). Thus, for negative charged particles the minima of the potential are located at the planes position. The main consequence of this fact is that the potential leads negative particles to collide with the nuclei, thus not favouring the channeling phenomenon.

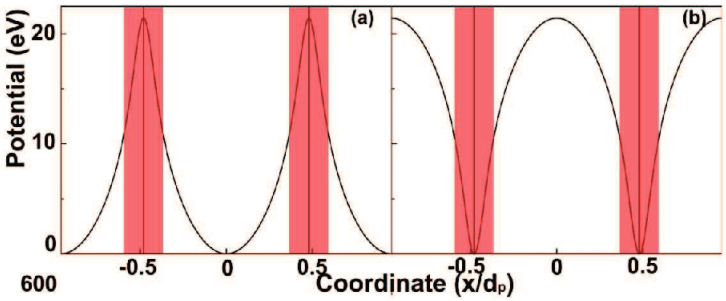

Figure 1.5: Potential well experienced by a positive (a) and a negative (b) particle channeled in <110> silicon planes [10].

1.2.2 Axial channeling

The potential generated by a string-like charge distribution smeared along the z direction (figure 1.6) features a radial symmetry along the axis direction. In the continuous approximation, the potential can be expressed as

$$U(\boldsymbol{r}_\perp) = \int_{-\infty}^{+\infty} \frac{dz}{d}\, V^{atom}(\boldsymbol{r}_\perp, z) \tag{1.16}$$

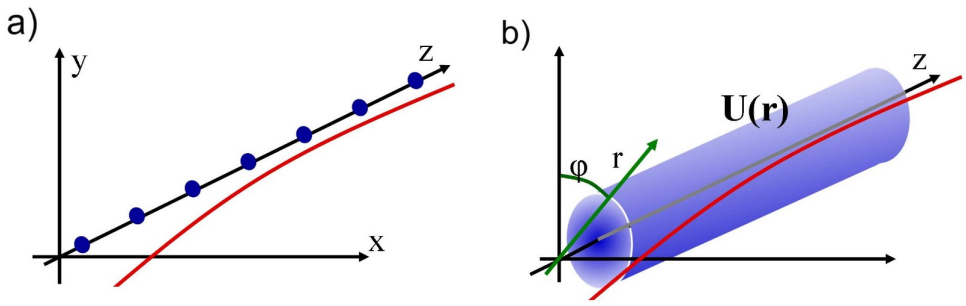

Figure 1.6: (a) Deflected trajectory by a string potential. (b) Interatomic potential $U(r)$ with a cylindrical symmetry; φ is the azimuthal angle of the trajectory [5].

where $V^{atom}(\boldsymbol{r}_\perp, z)$ is the potential of a single atom taking into account the screening effect, z the position along the string direction, $\boldsymbol{r}_\perp$ the component in the $x-y$ plane of the particle position and d the interatomic pitch.

The string potential of equation 1.16 can be computed as [1]

$$U(r_\perp) = \frac{Z_i Z e^2}{d} \ln\left(1 + \frac{3a_{TF}^2}{r_\perp^2}\right) \tag{1.17}$$

Thus, defining θ as the angle between z and the particle trajectory, it is possible to make the following cylindrical change of variables:

$$\theta = \sqrt{\left(\frac{dr_\perp}{dz}\right)^2 + \left(r_\perp \frac{d\varphi}{dz}\right)^2} = \sqrt{\theta_{r_\perp}^2 + \theta_\varphi^2} \tag{1.18}$$

where the $r_\perp$ and φ pedices indicate the radial and the azimuthal components of θ. The particle motion is characterized by the conservation of two quantities: the transverse energy $E_\perp$ and the angular momentum $J = pr_\perp\theta_\varphi$.
The transverse energy $E_\perp$ is computed in cylindrical coordinates as

$$E_\perp = \frac{pv}{2}\theta_{r_\perp}^2 + \frac{J^2}{2m\gamma r_\perp^2} + U(r_\perp) \tag{1.19}$$

The effective potential in the transverse direction is defined as follows:

$$W(r_\perp, \theta_{r_\perp}) = \frac{J^2}{2m\gamma r_\perp^2} + U(r_\perp) \tag{1.20}$$

Depending on the value of $E_\perp$, it is possible to distinguish different particle trajectories:

- $E_\perp \ll U_0$; the particle is trapped into the potential well, in a rosette-shaped orbit [11] around its axis: this condition is called hyperchanneling [12] and it is represented in blue in figure 1.7;
- $E_\perp \lesssim U_0$; the particle is still trapped into the potential well, but thermal fluctuations are strong enough to overcome the barrier and thus the particle could have enough energy to move from one axis to another (green line in figure 1.7);
- $E_\perp > U_0$; the particle is unbound and thus free to move into the crystal lattice, as depicted by the red line in figure 1.7.

Also in the case of axial channeling, positive and negative charged particles show different behaviors. In fact, the minimum of the effective potential of equation 1.17 moves farther from the axis, as the angular momentum J increases for negative particles, and nearer for the positive ones.

Similarly to the planar channeling, a critical angle can be calculated for the axial channeling (equation 1.15). Furthermore, the axial potential wells are deeper with respect to the planar case, thus the axial channeling features larger critical angles with respect to the planar channeling.

For instance the tungsten <100> axis features a well depth of $\sim 840\,\text{eV}$. At 120 GeV the critical angle is thus $\sim 110\,\mu\text{rad}$, which compared with the planar critical angle is 2-3 times larger [5].

For further details the reader is referred to [1, 2, 13].

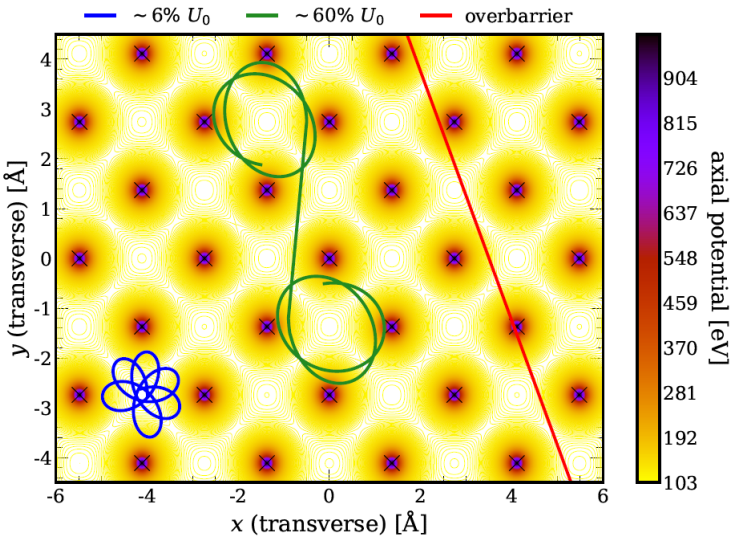

Figure 1.7: Contour plot of the tungsten <111> axis potential in the plane perpendicular to the axis direction (z). The crossmarkers indicate the string positions. The different colored lines are referred to different particle trajectories depending on the initial transversal energy [6].

1.3 The electromagnetic radiative energy loss by a charged particle

Charged particles lose energy in matter primarily because of ionization and radiation emission, which is known as bremsstrahlung. Such radiation results from the deceleration of the charged particles, caused by the electromagnetic interaction with the nuclei of the target material. Photon emission in an amorphous solid depends on the uncorrelated interactions of the particle with the solid atoms and thus coherent effects are absent. The first part of this section will focus on the Standard Bremsstrahlung (SB) which occurs in amorphous materials; then the modification of this phenomenon due to the crystal lattice will be treated in detail. The channeling radiation and coherent bremsstrahlung will be analyzed and finally the theoretical treatment of the Strong Field regime will be presented.

1.3.1 Standard bremsstrahlung

The Standard Bremsstrahlung (SB) integral cross section, in the ultra-relativistic limit and in the complete atomic screening approximation, is given by [14]

$$\Phi(\nu; E_0) = \frac{Z^2 \alpha r_0^2}{E_0^2 \nu} \, 4 \left[\left(E_0^2 + E^2 - \frac{2}{3} E_0 E \right) \log \left(183 Z^{-\frac{1}{3}} \right) + \frac{E_0 E}{9} \right] \quad (1.21)$$

where ν is the emitted photon frequency, $\alpha \sim 1/137$ the fine structure constant, E_0 the initial particle energy, E the exiting particle energy, Z the atomic number of the target material and $r_0 = e^2/mc^2$ the classical particle radius.
Several conclusions can be inferred from equation 1.21:

- the bremsstrahlung integral cross section exhibits a peak at low frequencies, leading to a pronounced emission of soft photons, as presented in figure 1.8;
- the photon emission cross section is strongly dependent on the atomic number of the target material Z;
- since the cross section $\Phi(\nu; E_0) \propto r_0^2 \propto (1/m)^2$, light particles, such as electrons and positrons, are the only particles undergoing bremsstrahlung till very high energies.

Figure 1.9 presents the lost energy fraction divided by the energy for an electron (or positron) due to the different physical processes in lead, as a function of the particle energy.
Three energy ranges can be identified [15]:

1. for energies below $\sim 10\,\mathrm{MeV}$, electrons primarily lose energy due to ionization;
2. in the $\sim 10\,\mathrm{MeV} - 1\,\mathrm{GeV}$ range, radiative loss dominates over the ionization one and it increases linearly with E;
3. for an energy above $\sim 1\,\mathrm{GeV}$, electrons lose energy primarily by means of bremsstrahlung and the lost energy fraction becomes linearly dependent on the incident particle energy.

At the energy equal to the critical one (E_c), the energy loss via ionization is comparable to the one via radiative emission.

A semi-empirical expression for the electron critical energy for solids (gases) is the following [15]:

$$E_c = \frac{610(710)\ \mathrm{MeV}}{Z + 1.24(0.92)} \quad (1.22)$$

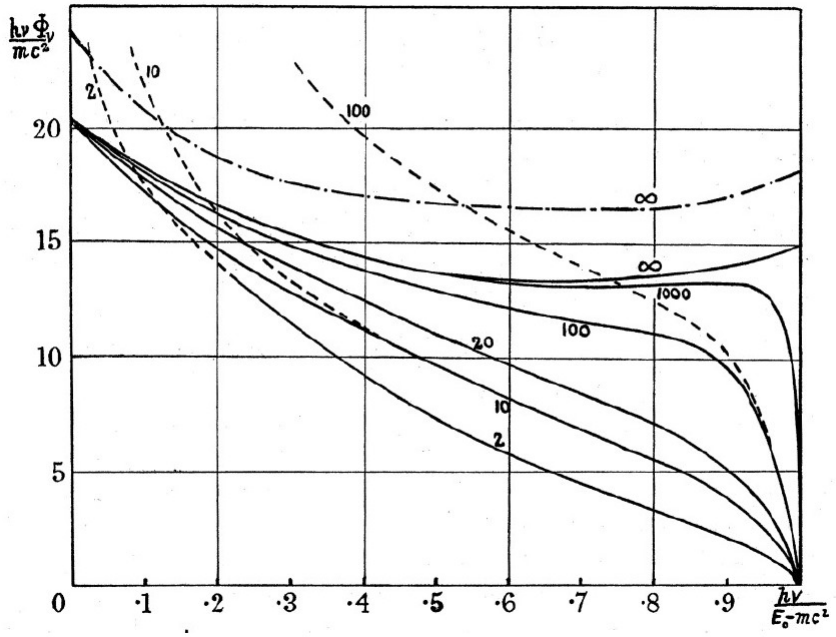

Figure 1.8: Spectral intensity of the radiation emitted by an electron impinging on a Pb target, considering the whole cross section (solid line), the cross section without the screening effect (dashed lines) and referred to H_2O (dotted dashed line). Φ_ν is the cross section in units of $Z^2 r_0^2 \alpha$. The numbers refer to the primary energy E_0 in units of mc^2 [14].

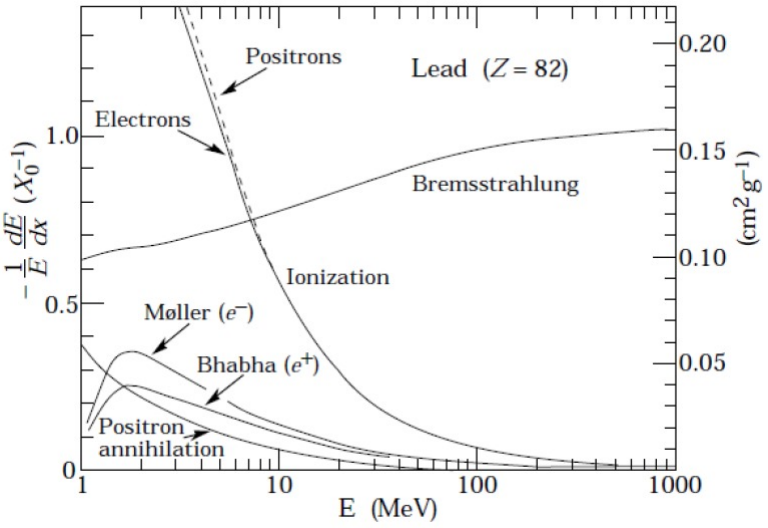

Figure 1.9: Fraction of the energy lost by an electron (or a positron), divided by the energy, for different physical processes [15].

where Z is the atomic number of the target material. The other fundamental quantity is the radiation length X_0. It represents the distance that an electron must cross in a material in order to lose all but $1/e$ of its energy via bremsstrahlung. A rough estimation of this length is the following [15]:

$$X_0 = \frac{(716\ \mathrm{g/cm^2})A}{\rho Z(Z+1)\log(287/\sqrt{Z})} \tag{1.23}$$

where ρ, Z and A are the density, the atomic number and the mass number of the target material, respectively.

1.3.2 Radiation formation length

The formation of the bremsstrahlung radiation is a physical phenomenon which occurs in a finite amount of time, and thus space. This can be seen as a consequence of the limited momentum transfer between the particle and the scattering centers. In fact, this leads to an uncertainty in the longitudinal spatial position of the charged particle due to the Heisenberg uncertainty principle [16]. This space interval is known as the formation length (l_f) or coherence length. If some external agent disturbs the charged particle dynamics during the formation period, the radiation emission process can be altered [17].

In particular a photon is considered free if separated from its parent by at least one wavelength $\lambda = 2\pi c/\omega$ [16, 18], where c is the light speed and ω the radiation angular frequency.

In fact, indicating the velocity of the incident electron as v, the radiation formation length is computed as follows:

$$\frac{l_f}{v} - \frac{l_f}{c} = \frac{\lambda}{2\pi c} = \frac{1}{\omega} \tag{1.24}$$

In the relativistic limit, $v \to c \implies \beta \sim 1 - 1/2\gamma^2$, and this implies [18]:

$$l_f = \frac{2\gamma^2 c}{\omega} \tag{1.25}$$

As a consequence of equation 1.25, photons at higher energies are formed at shorter distances (and hence in a shorter time) [17], while more energetic electrons emit a photon having a $\hbar\omega$ energy in a broader space interval.

For very high energy impinging particles, it is necessary to perform the quantum correction substituting $\omega \to \omega'$ ($\omega' = \omega E/(E - \hbar\omega)$) which takes into account the recoil experienced by the electron due to the emission of radiation [18].

However, if the electron dynamics is disturbed within the radiation formation length, the emission of electromagnetic radiation will also be altered. For instance, at high energies or high densities, the Bethe-Heitler cross-section for bremsstrahlung (and for pair production) needs to be corrected for the Landau-Pomeranchuk-Migdal (LPM) effect [17, 19]. This effect involves the partial suppression of soft photons when the trajectory of the electron, or positron, is altered by multiple Coulomb scattering. Furthermore, if an incident electron crosses the crystalline lattice, it may happen that l_f extends over several interatomic distances along an axis or a plane. This can generate various coherent effects in the radiation emission. The following sections will show that coherent effects modify both the intensity and the spectrum of the emitted radiation.

1.3.3 Channeling radiation

When an electron (or a positron) is channeled, the particle periodic trajectory leads to a coherent emission of electromagnetic radiation called Channeling Radiation (CR). The coherent features of such a radiation appear when the radiation formation length is larger than a trajectory period inside the channel.

The emission of channeling radiation is conditioned by the angular acceptance, dominated by the critical angle defined in equation 1.15.

Therefore, the resulting radiation arising from the interaction of the electron (or positron) beam with the lattice atoms, will be the convolution of an incoherent spectrum due to the particles impinging at angles larger than the critical one which produce SB radiation, and the coherent component. The channeling radiation, depending on the initial particle energy, presents different characteristics:

- for an electron with an energy below 100 MeV, a quantum description is needed because of the limited number of available energy states. It is possible to approximate the particle with an electric dipole in the plane transverse to the particle motion and its emitted radiation spectrum shows quantized peaks, as presented in figure 1.10.

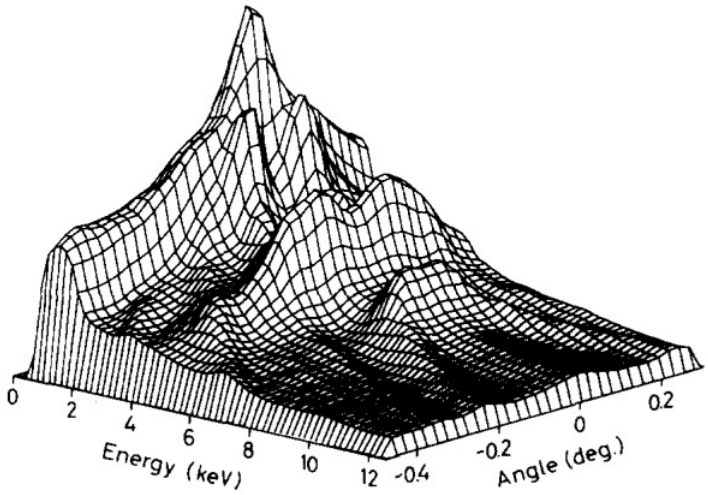

Figure 1.10: Experimental channeling radiation spectrum as a function of the energy and the angle of incidence of the electron. Experimental data are obtained with a 4 MeV electron beam on a 0.5 µm Si crystal [20].

- Increasing the electron energy up to ~ 100 MeV - few GeV, the available energy states are much more. The dipole approximation still holds but a complete classical treatment of the radiation is allowed because the thermodynamic limit of the occupation number of the energy states is reached. In the channeling condition, up to these energies, the angles between the particle trajectory and the crystallographic direction (θ, with $\theta \leq \theta_c \propto \gamma^{-1/2}$) are smaller than the opening angles of the light cone ($\sim 1/\gamma$) produced by bremsstrahlung. Therefore, electromagnetic

radiation will be emitted globally in the forward direction relative to the particle trajectory, summing up coherently as it happens in an undulator[1] [21], as shown in figure 1.11(a). The channeling radiation spectrum, as well as the undulator one, exhibits well-defined peaks at specific harmonic numbers and it is presented in figure 1.11(b).

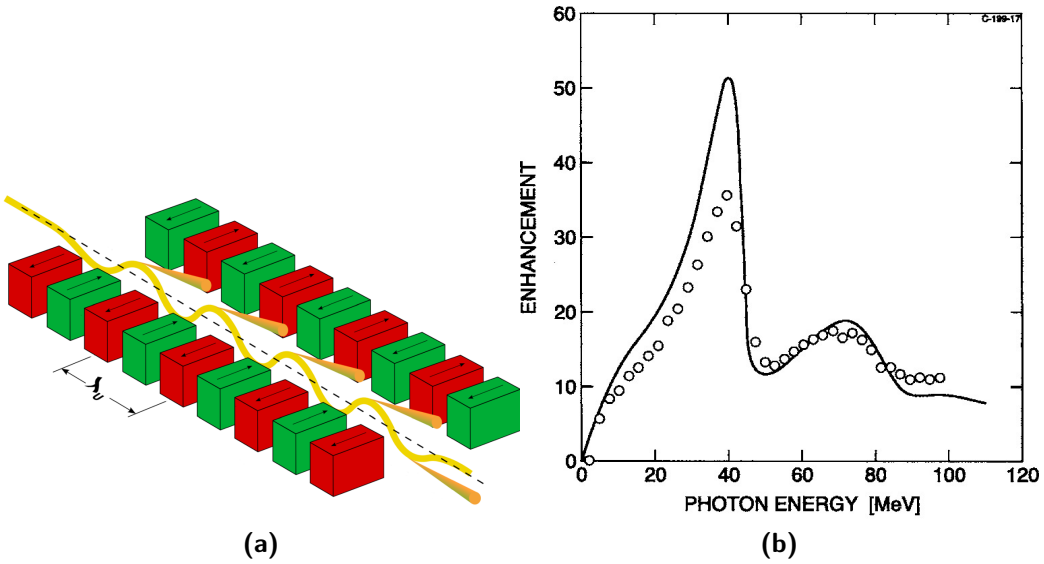

Figure 1.11: (a) Working scheme of an undulator; the colored blocks are magnets with alternating polarity, λ_u is the magnet pitch. The light cones are emitted in the forward direction. (b) Channeling radiation spectrum for a 6.7 GeV positron incident parallel to the (110) plane in a silicon crystal, rescaled to the SB value. Empty dots represent the experimental data, while the solid line represents the theoretical curve [18].

- For energies greater than $\sim$ few GeV, the angular channeling acceptance decreases and $\theta_c > 1/\gamma$. In this case, the electromagnetic radiation is no longer emitted in the forward direction relative to the particle trajectory. The transverse particle motion of the charged particle can no longer be approximated with an oscillating electric dipole. However, the channeled particle features the same behavior of a charged particle in a constant magnetic field. This leads to the emission of synchrotron radiation [22]. Figure 1.12 presents the synchrotron radiation spectrum: the harmonic peaks are no more present and the spectrum presents a hardening at high energy.

[1] An undulator is an insertion device composed by dipole magnets with alternating polarity.

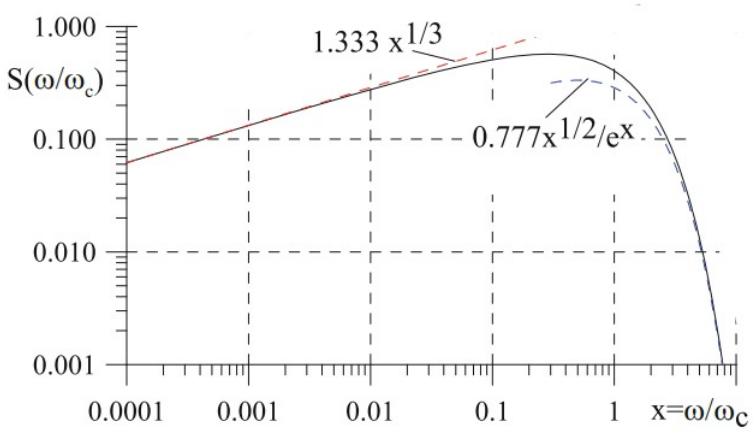

Figure 1.12: Synchrotron radiation spectrum as a function of the angular frequency normalized to the critical value. As ω approaches the critical frequency, an exponential decrease becomes evident [23].

The gamma rays emitted with frequencies that exceed the critical one (ω_c) feature an exponential suppression of their intensity (figure 1.12). The critical frequency is computed as [22]:

$$\omega_c = \frac{3c\gamma^3}{2R} \tag{1.26}$$

where R is the curvature radius of the impinging particle. In the multi-GeV energy domain, the classical treatment of the radiation emission breaks down. In fact, in this high energy range, the electron (or positron) recoil due to the photon emission becomes relevant. Schwinger pointed out that when the radiated photon momentum becomes comparable to the impinging electron one, the quantum effects are no more negligible [24]. A semiclassical method used to take into account the electron recoil consists in the substitution $\hbar\omega_c/E \rightarrow \hbar\omega_c/E(1 - \hbar\omega_c/E)$ in equation 1.26. However, a full quantum description here is needed to achieve physical results.

For further details, the reader is referred to [18, 20–22, 24, 25].

1.3.4 Coherent Bremsstrahlung

Channeling radiation is intimately associated with a new type of electromagnetic radiation: coherent bremsstrahlung (CB). CB occurs when charged

particles impinge on the solid lattice with angles extending beyond the critical value, but small enough to use the continuous potential approximation. The comparison between a positron trajectory generating CR and one generating CB is presented in figure 1.13. It represents in a pictorial way the difference between channeling radiation and coherent bremsstrahlung: the first features its coherent effects thanks to the periodicity of the particle motion along the crystallographic direction, while the latter coherent effects are due to the positron transversal periodic trajectory. In this section electrons and positrons will be considered as plane waves under the Born approximation [26, 27].

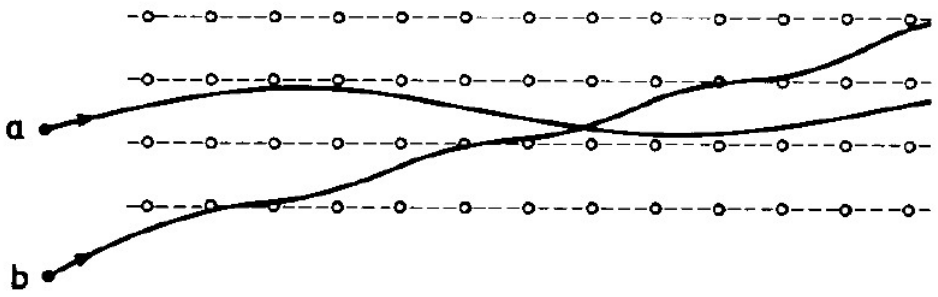

Figure 1.13: Two positron trajectories: (a) produces channeling radiation and (b) coherent bremsstrahlung [26].

Under these conditions, the total CB differential cross section is computed as [18]:

$$\left.\frac{d\sigma}{d\hbar\omega d^3q}\right|_N = \left.\frac{d\sigma}{d\hbar\omega d^3q}\right|_s \left|\sum_{i=1}^{N} e^{-i\boldsymbol{q}\cdot\boldsymbol{r_i}}\right|^2 \tag{1.27}$$

where the subscript s indicates the cross section of the interaction between the projectile and the single atom, and N refers to the CB cross section involving the interaction between the impinging particle and the N-atom lattice. $\boldsymbol{r_i}$ is the spatial position of the i-th atom and $\boldsymbol{q}$ the electron recoil momentum.

For an amorphous material in the limit $N \to \infty$, the summation on the right hand side of equation 1.27 will be equal to N. This is true because all double products arising from random phases cancel out. On the contrary, in presence of a periodic crystalline lattice, the phases add up, producing the enhancement of the differential cross section. More precisely the aforementioned summation becomes [18]:

$$\left| \sum_{n_i} e^{-i\boldsymbol{q}.\boldsymbol{r}} \right|^2 = \frac{N(2\pi)^3}{N_0 \Delta} |S(\boldsymbol{g})|^2 \sum_{\boldsymbol{g}} \delta^3(\boldsymbol{q} - \boldsymbol{g}) \tag{1.28}$$

where N_0 is the number of atoms in the unit cell of volume Δ, $\boldsymbol{g}$ the reciprocal lattice vector[2], and $S(\boldsymbol{g})$ the lattice structure function [28].

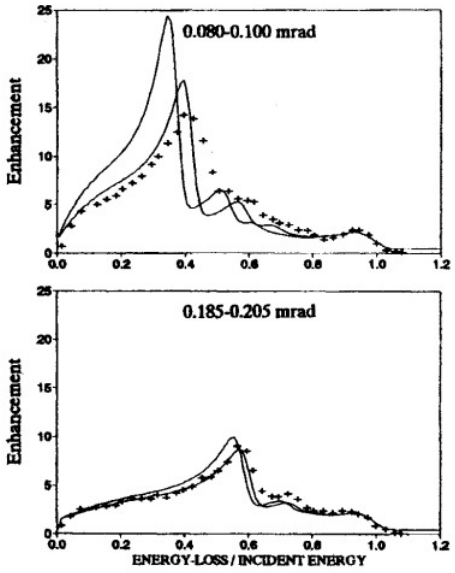

Figure 1.14: Radiation spectrum from a 150 GeV electron beam impinging on a 0.6 mm Si crystal with different incidence angles with respect to the (110) plane, rescaled to the amorphous values [18].

Equation 1.28 states that the differential cross section becomes appreciably different from zero if the recoil momentum $\boldsymbol{q}$ is equal to a vector of the reciprocal lattice $\boldsymbol{g}$, i.e. when the wavelength of the emitted radiation is an integer multiple of the direct lattice spacing of atoms [18]. As a consequence, the emitted radiation spectrum features several peaks located at specific energies of the outgoing photon (figure 1.14), whose values depend on the lattice spacing, as mentioned above.

[2]The reciprocal lattice vector is obtained performing the Fourier transform of the crystalline periodic lattice.

1.3.5 Strong Field effect

A relativistic charged particle entering the crystal lattice will perceive, along the direction parallel to the motion, the interatomic distances of the lattice reduced by a factor $1/\gamma$ in its rest frame because of the Lorentz contraction [29]. This fact, in case of a purely electric field, gives rise to the following field transform law [29]:

$$\begin{cases} \varepsilon'_{\parallel} = \varepsilon_{\parallel} \\ \varepsilon'_{\perp} = \gamma\varepsilon_{\perp} \end{cases} \tag{1.29}$$

where $\varepsilon_{\parallel}$ and $\varepsilon_{\perp}$ are the components of the electric field parallel and orthogonal to the particle trajectory in the laboratory frame, while $\varepsilon'_{\parallel}$ and $\varepsilon'_{\perp}$ are the components in the particle reference frame. As a consequence of equation 1.29, a particle traveling along the plane or axis direction of a crystal lattice experiences a stronger electric field in the transverse direction.

If the electric field in the particle rest frame ($\varepsilon'_{\perp}$) reaches the critical limit, some exotic physical processes could happen. The critical electric field (ε_c) or Schwinger electric field refers to a limit beyond which the electromagnetic field is predicted to become non linear. In that case the quantum vacuum will begin to produce real pairs of charged particles (e^+/e^- in QED), and the vacuum itself becomes dynamic [30].

These phenomena are predicted by the quantum field theories; this thesis focuses on what concerns the QED non linear effects. They become dominant for electric fields higher than the Schwinger limit, expressed by the following formula [18, 31]:

$$\varepsilon_c = \frac{m_e^2 c^3}{\hbar e} \sim 1.3 \times 10^{18}\ \text{V/m} \tag{1.30}$$

This value of the electric field is extremely high; consider that at these orders of magnitude, a proton would reach the same energy produced by the Large Hadron Collider (of the order of TeV) in a length of $\sim 1\,\mu\text{m}$. The generation of such strong fields is out of reach in the modern experiments on a macroscopic scale of lengths. They are present only in objects of astrophysical interest such as supernovae, pulsars and magnetars [32, 33]; the latter features a magnetic field exceeding the magnetic critical limit.

However, this limit has already been reached and exceeded on subatomic scales. In the ATLAS experiment at CERN the first observation of a photon-photon scattering process has been confirmed during the collisions between lead ions, generating electric fields of the order of 10^{25} V/m [34] and allowing the surrounding photons to scatter between themselves in the Strong Field regime.

Furthermore, if a charged particle impinging on a crystal lattice has a Lorentz boost large enough, it could reach the SF limit for the $\varepsilon'_{\perp}$ component. The electromagnetic processes will be altered by the QED nonlinear phenomena and matter/antimatter production discussed earlier. The parameter χ allows to define the energy regions in which the Strong Field effects are relevant. It is defined as [18]

$$\chi = \frac{\gamma\varepsilon_{\perp}}{\varepsilon_c} = \frac{\varepsilon'_{\perp}}{\varepsilon_c} \tag{1.31}$$

The effects of the Strong Field regime become evident for $\chi \gtrsim 0.1$, while they are dominant in the $\chi \gtrsim 1$ range [2].

In his work, Baier [2] provided a rough estimate for χ as a function of the main characteristics of the crystal lattice and the impinging particle:

$$\chi = \frac{U_0 \gamma \hbar}{m^2 c^3 a_{TF}} \tag{1.32}$$

with a_{TF} the Thomas-Fermi screening distance introduced in subsection 1.2.1. For instance, for an electron of 5.6 GeV entering the $PbWO_4$ <001> axis, $\chi \sim 0.2$, while for an electron of 120 GeV $\chi \sim 4$ [35].

The transverse electric fields experienced by ultra-relativistic electrons and positrons (with GeV energies) are treated under the Constant Field Approximation (CFA). Indeed, the charged particle follows a circular trajectory, similar to the one experienced by a particle within a synchrotron. Following the steps outlined by Sorensen, it is possible to estimate the angular aperture between the beginning and end of a single circular stage of the motion in a crystal lattice [25]:

$$\Delta\theta = \frac{U_0}{\gamma m c^2 \theta} \tag{1.33}$$

being θ and $\Delta\theta$ the incidence and the deflection angle and m the incident particle mass.

As explained in subsection 1.3.3, the angular aperture of the particle trajectory inside the lattice and the light cone angular spread define the type of the emitted electromagnetic radiation. To characterize the SF one, it is necessary to introduce the Baier angle [2, 18]:

$$\Theta_0 = \frac{U_0}{mc^2} \tag{1.34}$$

For $\theta \gg \Theta_0$ ($\Delta\theta \ll 1/\gamma$) the radiation has a dipole nature, instead if $\theta \ll \Theta_0$ ($\Delta\theta \gg 1/\gamma$) it has a synchrotron nature [18].

Equation 1.34 outlines that the Baier angle does not depend on the initial particle energy. In the high energy regime (GeV scale for e^+ and e^-), since $\theta_c \propto 1/\sqrt{E}$, the channeling effects are typically suppressed by the Strong Field one, governed by the Baier angle. Indeed typical values for the W <111> axis are $\theta_L \sim 100\,\mu\text{rad}$ and $\Theta_0 \sim 1.2\,\text{mrad}$ for a 120 GeV electron [5].

A quantum treatment of the SF radiation is available in [18] and a critical frequency (ω_c) for the synchrotron regime of the radiation is attained:

$$\omega_c = \frac{\chi}{\chi + 1}\frac{E}{\hbar} \tag{1.35}$$

where χ is the Strong Field parameter and E the incident particle energy. Figure 1.15 shows the SF radiation spectrum and its exponential suppression, highlighting the quantum corrections due to the spin of the incident particle.

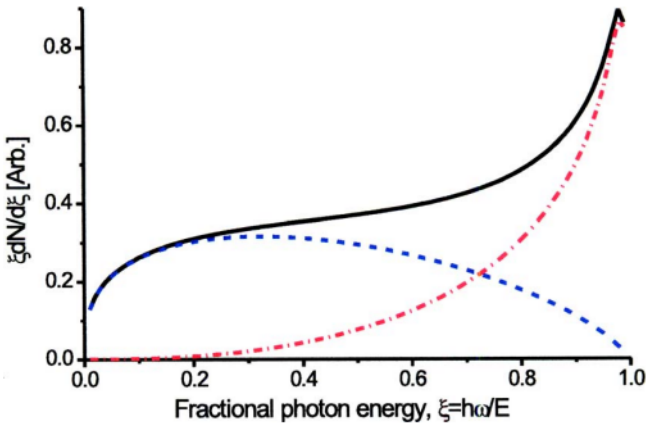

Figure 1.15: Intensity in arbitrary units of the radiation emitted in the Strong Field regime ($\chi = 100$) as a function of the fractional photon energy. The solid line is the total spectrum, the blue dashed line is the intensity profile without spin corrections and the red dotted dashed one includes the spin corrections. At $\xi = \xi_c = 100/101$, the exponential suppression starts [18].

1.4 Pair production

Another (quantum) electromagnetic phenomenon consists in the photon conversion into $e^- - e^+$ pairs. This process, occurring in amorphous materials, is known as Standard Pair Production (SPP). Unlike the radiative process

of Bremsstrahlung, pair production is a threshold process; it is allowed only for incident photon energies $h\nu$ greater than twice the electron mass ($h\nu \geq 1.022\,\mathrm{MeV}$). Its integral cross section is given by the Bethe-Heilter formula, that, in the ultra relativistic limit and in the complete screening approximation for the target material, reduces to [14]:

$$\Phi_{pair}(E_-;\nu) = \frac{Z^2\alpha r_0^2}{(h\nu)^3}\,4\left[\left(E_+^2 + E_-^2 + \frac{2}{3}E_+E_-\right)\log\left(183Z^{-\frac{1}{3}}\right) - \frac{E_+E_-}{9}\right] \tag{1.36}$$

where $E_-(E_+)$ is the electron (positron) energy, $h\nu$ the initial photon energy with the constraint $h\nu = E_+ + E_-$; Z is the target atomic number, α the fine structure constant and r_0 the classical particle radius introduced in subsection 1.3.1.
Equation 1.36 suggests the following observations:

- the SPP cross section and the SB one are related by the crossing symmetry. Indeed the SPP cross section, except for a different numerical prefactor, can be obtained from equation 1.21 swapping $E_0 \to E_-$ and $E \to -E_+$;
- $\Phi_{pair}(E_-;\nu)$ is symmetric exchanging E_+ and E_-;
- in the low energy range for the incident photon ($h\nu \lesssim 50\,\mathrm{MeV}$), it is more favorable that the daughter particles of the process (e^+ and e^-) share the same amount of energy, as shown in figure 1.16(a);
- in the high energy range for the incident photon ($h\nu \gtrsim 50\,\mathrm{MeV}$) it is more probable that one of the two produced particles carries away the majority of the initial energy (figure 1.16(a)).

It is necessary to emphasize that pair production becomes the dominant physical process only at high energies. It is possible to distinguish three energy regions for the incident photon:

- for energies $h\nu \lesssim 10\,\mathrm{MeV}$ photons lose energy primarily via the Compton and the photoelectric effect;
- for energies in the $\sim 10\,\mathrm{MeV} - 1\,\mathrm{GeV}$ range pair production becomes the dominant effect, as shown in figure 1.16(b);
- for energies $h\nu \gtrsim 1\,\mathrm{GeV}$ SPP dominates and the lost energy fraction is practically independent on the photon energy.

The intensity of a photon beam impinging on a target material is reduced to a factor of $1/e$ over a distance of $9/7X_0$, with X_0 the radiation length of the target introduced in subsection 1.3.1 [15].

1.4.1 Pair production in the lattice

The electric field, generated by the crystalline structure of a target material, can interact with the incident photon despite its charge neutrality. In fact, matter can interfere in the process while the e^-/e^+ pair is in a virtual state. The formation length of the lepton-antilepton pair is computed as [18]:

$$l_f^{PP} = \frac{2\gamma_p^2 c}{\omega^*} \tag{1.37}$$

where $\omega^* = \dfrac{\omega}{\eta_+\eta_-}$ and $\eta_\pm = E_{e^\pm}/\hbar\omega$, being $E_{e^\pm}$ the positron and electron energy, ω the photon angular frequency and $\gamma_p = \hbar\omega/mc^2$ being m the electron mass. This last factor defines the average angular aperture of the emitted pair ($\theta_{pair} \sim 1/\gamma_p$).

The enhancement of the pair production yield occurs when the emission is altered within the formation length (equation 1.37) by the lattice potential. This enhancement has a kinematic threshold ($\hbar\omega_{min}$), which can be estimated requiring the pair angular aperture to be smaller than the Lindhard angle [25]:

$$\hbar\omega_{min} \sim \frac{2(mc^2)^2}{U_0} \tag{1.38}$$

For the <100> $PbWO_4$ axis, $U_0 = 464\,\text{eV}$ thus $\hbar\omega_{min} \sim 1.2\,\text{GeV}$. A pronounced increase in the pair production probability occurs when the Strong Field regime is reached. A rough estimation of the SF threshold energy for the impinging photon is provided by [18]

$$\hbar\omega_t \sim \frac{\sqrt{2}u_1(mc^2)^2}{U_0 \lambda\!\!\!^{-}_c} \tag{1.39}$$

where $\lambda\!\!\!^{-}_c = \hbar/mc$ is the Compton wavelength, and u_1 the one-dimensional thermal displacement of the lattice atoms.

Above this energy threshold and within the SF angular acceptance ($\theta < \Theta_0$, with θ the incidence angle of the photon with respect the crystallographic direction), the enhancement of the Strong Field Pair Production (SFPP) probability with respect to the SPP one grows upon a certain limit. In fact, being W_p the Strong Field Pair Production probability per unit time, in the limit $\chi \gg 1$ it results [2, 18]:

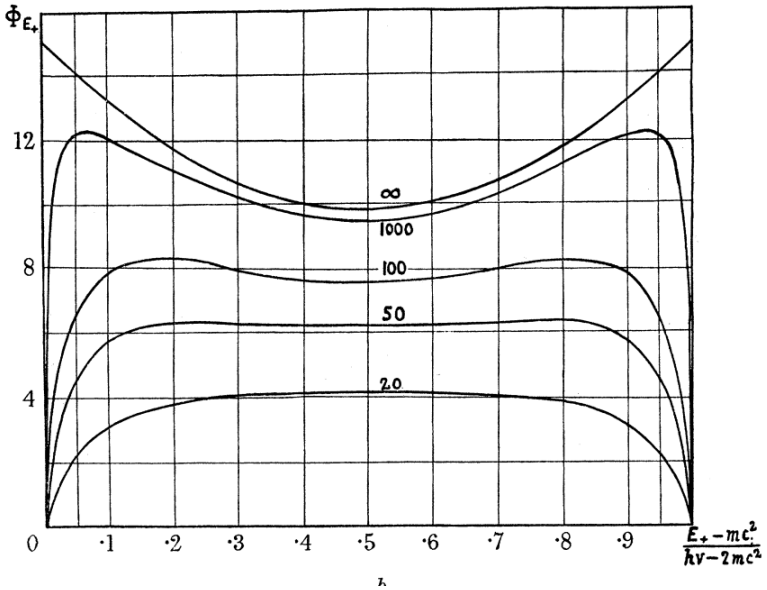

(a)

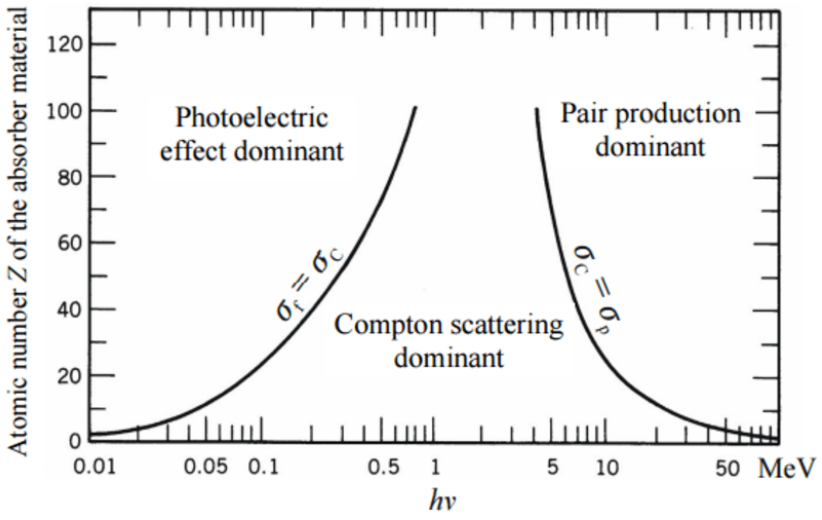

(b)

Figure 1.16: (a) Integral cross section (in units of $Z^2 r_0 \alpha$) for the pair production process. $E_+ - mc^2$ represents the positron kinetic energy, being m the electron (positron) mass. The numbers above the curves indicate the initial photon energy (in units of mc^2) [14]. (b) Diagram illustrating the dominant physical processes as a function of the initial photon energy $h\nu$ and the atomic number of the target Z. The solid lines indicate the regions in the $Z - h\nu$ plane where the different physical processes have the same total cross section.
σ_f, σ_C and σ_p are respectively the total photoelectric, Compton and pair production cross sections.

$$W_p \propto \frac{\alpha m c^2}{\hbar \chi^{1/3}} \tag{1.40}$$

The probability W_p becomes lower than the SPP one once the energy reaches the region where $\chi \gtrsim 10$ [18]. On the other hand, in the limit $\chi \ll 1$, W_p is exponentially suppressed. However, the maximum enhancement factor (η_{max}^{PP}) is computed as follows [2, 18]:

$$\eta_{max}^{PP} = \frac{W_{CFA}^{max}}{W_{BH}} \sim \frac{U_0 m a_{TF} d}{3Z^2\alpha^2\hbar^2 \log\left(183Z^{-1/3}\right)} \tag{1.41}$$

where W_{CFA} is the probability per unit time of the SFPP process under the Constant Field Approximation and W_{BH} is the probability per unit time of the SPP, obtained using the standard Bethe-Heitler formulation; a_{TF} is the Thomas-Fermi screening distance, d the lattice spacing, Z the target atomic number and m the electron mass.

The factor η_{max}^{PP} typically reaches values up to ~ 150 for photon energies $\hbar\omega \sim 100\ \hbar\omega_t$, which correspond to the multi-TeV energy region. For higher energy the enhancement is self suppressed and W_{CFA} decreases as $1/(\hbar\omega)^{1/3}$, according to equation 1.40 [18, 36].

Figure 1.17 shows the trend of the SFPP probability per unit distance as a function of the incident photon energy, for different target materials.

For angles $\theta \gg \Theta_0$, the CFA breaks down. However, it is possible to develop a perturbative treatment using the Born approximation that describes the relative enhancement in the photon energy loss. Further details are provided in [2, 6, 18, 25, 27, 36].

In this chapter, several physical phenomena involving the interaction between particles and the crystal lattice have been discussed, with a special emphasis on the energy loss mechanisms of charged electrons (positrons) and photons. The next chapter will explain how these physical phenomena allow the development of compact electromagnetic calorimeters and how the new generation crystal-based technology can be applied in the high energy physics field.

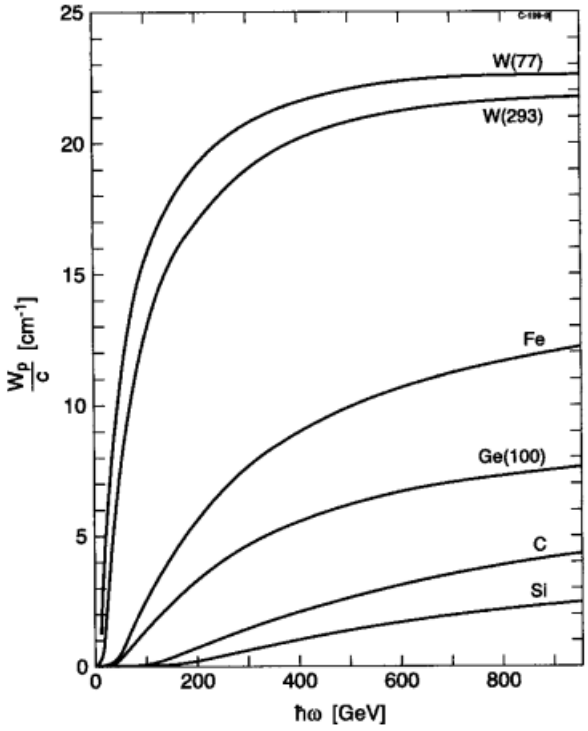

Figure 1.17: SFPP total probability for unit distance as a function of the incident photon energy. The photon impinges along the <111> axis for C, Si, Fe, and W and along <110> for Ge. The temperatures different from the room one are indicated in brackets [2].

Chapter 2

Applications of crystals and experimental techniques

The interaction between particle beams and crystalline structures is a highly active and fascinating area of research for a variety of reasons. It not only offers invaluable insights into the fundamental properties of matter but also drives the development of technological devices for high energy physics.

This chapter deals with the experimental techniques used for the investigation of the electromagnetic shower development within crystal lattices and the technological application of oriented crystals.

The first part of the chapter will present the physical parameters needed to characterize the development of an electromagnetic shower within matter. Moreover, it will be explained how these quantities undergo modifications when the target material is a crystal oriented with the particle beam direction. Then, the main results obtained by the AXIAL (Axial and quasi-axial coherent interaction between charged particle beams and crystals) and ELIOT (ELectromagnetic processes In Oriented crysTals) collaborations will be presented, followed by an overview of the goals of the *STORM* (STrOng cRystalline electroMagnetic field) project. The chapter ends summarizing several possible future applications of oriented crystals.

2.1 Electromagnetic showers in oriented crystals

When a high energy particle interacts with matter, whether it is charged (as in the case of electrons or positrons) or neutral (such as photons), it can generate an electromagnetic shower in the target material. Electrons in the electromagnetic shower generate photons via bremsstrahlung, which, if they

have an energy large enough, can produce e^-/e^+ pairs. As the process unfolds, the particles are generated with decreasing energies. When the involved energies approach the critical energy, defined in equation 1.22, energy losses due to non radiative processes become dominant, stopping the electromagnetic shower development. If the beam impinges on an amorphous material or on a not oriented crystal sample, the maximum number of secondary particles is generated at a depth which can be approximated as follows [37]:

$$t_{max} = \log\left(\frac{E_0}{E_c}\right) + t_0 \tag{2.1}$$

where E_0 is the initial energy, E_c the critical one, t_0 a parameter depending on the particle starting the shower (-0.5 for electrons, 0.5 for photons) and t_{max} is expressed in units of X_0. Another fundamental parameter in the field of calorimetry, where destructive techniques are employed to measure the energies of incident particles, is t_{95}. This parameter represents the length in units of X_0 required for a calorimeter to contain 95% of the energy produced in the electromagnetic shower and it is computed as follows [37]:

$$t_{95} \simeq t_{max} + 0.08Z + 9.6 \tag{2.2}$$

where Z is the target atomic number. Typically, in calorimeters with a thickness of $\sim 25X_0$, the shower longitudinal leakage beyond the end of the detector is less than 1% up to incident electron energies of 300 GeV [37].

On the other hand, the characteristic scale of the transversal spread of an electromagnetic shower is given by the Molière radius (R_M). The Molière radius, as the radiation length, is a parameter which depends only on the properties of the material the particle beam interacts with and it is independent on the initial particle energy. 90% of an electromagnetic shower is contained within an infinitely long cylinder with a radius equal to 1 R_M, while 95% is contained within 2 Molière radii.

If the target is an oriented crystal, the development of the electromagnetic shower has a different behavior. In such case, the enhancement in the energy deposit due to the effects induced by the Strong Field regime leads to a reduction in the shower length, as sketched in figure 2.1. The reduction of the shower length can be seen equivalently as the reduction of the effective radiation length with respect to the value obtained in the case of a randomly oriented material. The X_0 reduction could be exploited to design a new type of compact electromagnetic calorimeter, composed of oriented crystals. In fact, the main goal of this thesis is to estimate in a quantitative way the X_0 reduction for a $PbWO_4$ crystal sample, tested during the *STORM* 2022 beamtest with a high energy electron beam. The results will be presented

in subsection 5.2.3.

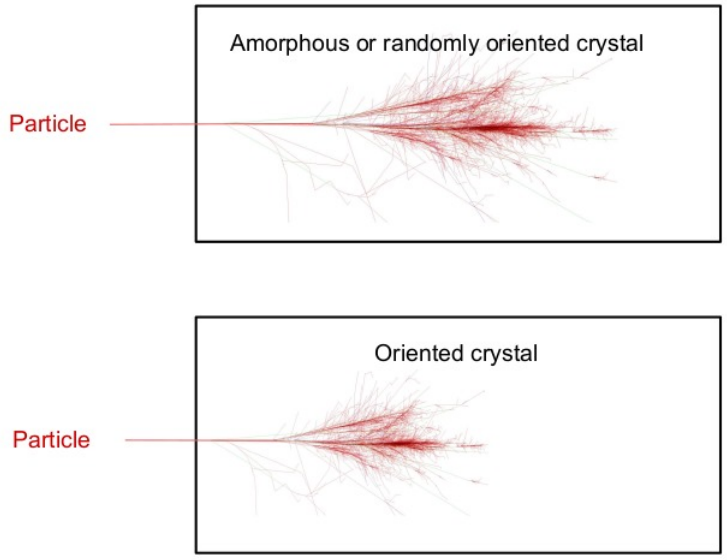

Figure 2.1: Sketch of the electromagnetic shower development in an amorphous medium (top) and in a crystal aligned with the beam direction (bottom) [5].

Moreover, as represented in figure 2.2, in the 1 GeV-1 TeV energy range the t_{max} parameter, which in an amorphous material depends logarithmically on the initial particle energy (equation 2.1), depends only weakly on E_0.

Since t_{max} is almost independent on the incident particle energy, and thus also t_{95}, not only it will be possible to produce a compact calorimeter (thanks to the reduction of the electromagnetic shower length), but also the calorimeter thickness needed to contain the entire electromagnetic shower will be practically independent on the incident energy.

Finally, the lattice-to-beam orientation affects primarily the first part of the electromagnetic shower. After the first few radiation lengths, the angles involved exceed the angular acceptance of the Strong Field regime (Θ_0), thus losing the coherent effects in the energy deposit processes. As a consequence, the radiation length reduction will be more pronounced when the object under test has a smaller longitudinal dimension, as it will be pointed out in subsection 5.2.3. It must be emphasized that this fact is not in contrast with the possibility to develop an oriented calorimeter: particles crossing thinner crystals experience a greater enhancement in the energy deposit

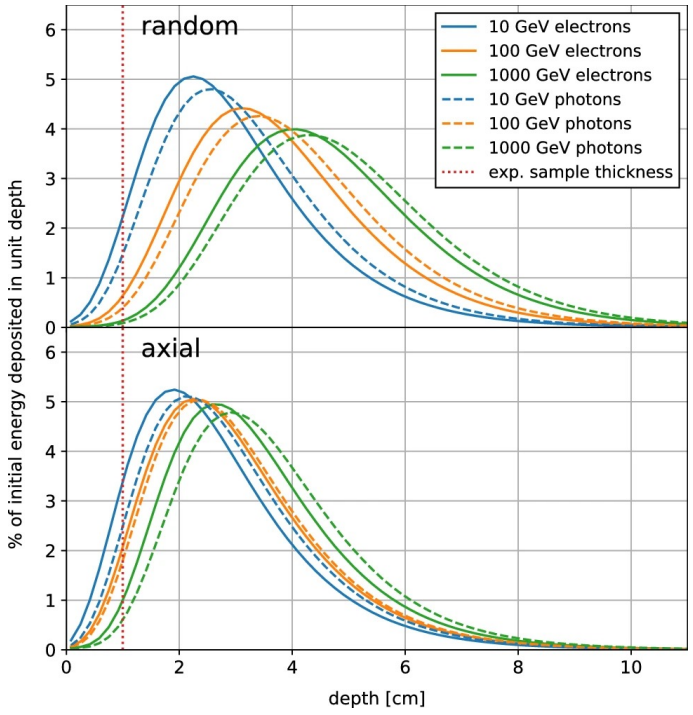

Figure 2.2: Simulated energy deposit in a crystalline tungsten medium aligned with the <111> axis, normalized to the primary particle energy, as a function of the material depth, for different types of incident particles and different energies [38].

because the emitted secondary particles do not have space enough, within the target material, to exit from the angular acceptance of the SF effects; nevertheless also in thicker oriented crystals the e.m. shower will undergo an acceleration in its development in the first radiation lengths, thus leading to a better longitudinal containment of the energy and a X_0 reduction.

The main aspects and parameters characterizing the development of an electromagnetic shower, in amorphous and oriented materials, have been introduced. The next sections will present the main collaborations that have investigated and are investigating the Strong Field effects in crystals.

2.2 Experimental techniques and main results

It is well known since the 1950s that the crystal lattice may strongly modify both the pair production cross section and the bremsstrahlung emission spectrum [39, 40]. A theoretical overview of these physical phenomena has already been provided in the first chapter. The following sections will present the state of the art of the experimental techniques used to investigate such effects. The main experimental results will be examined with a particular focus on the *STORM* project, that is the framework in which this thesis has been performed.

2.2.1 The AXIAL/ELIOT collaboration

The first preliminary tests on a 4 mm ($0.45X_0$) thick $PbWO_4$ crystal sample have been performed during the 2017-2018 beamtests. The experimental investigations took place at the CERN North Area H2 and H4 extracted beamlines and at the DESY T21 beamline [35, 41].

The main purpose of the AXIAL and ELIOT collaborations, two INFN (Istituto Nazionale Fisica Nucleare) projects of the CSN5 (Commissione Scientifica Nazionale 5), was to estimate the acceleration of the e.m. shower development due to the Strong Field effects induced by the crystal lattice of the $PbWO_4$, a high-Z crystal widely used for the development of electromagnetic calorimeters. The experimental setup exploited in the CERN North Area is depicted in figure 2.3. The trigger was generated by two plastic scintillators (S1-2). The two microstrip telescopes (SD1-2), whose features are described in subsection 3.2.2, reconstructed the impinging electron trajectory while the $PbWO_4$ sample was mounted on a high precision remotely controlled goniometer, whose performances will be presented in subsection 3.2.5. The multiplicity counter (SD3) estimated the number of charged particles generated in the crystal sample, which were swept away by the bending magnet

(the white triangle in figure). The surviving photons interacted with the downstream electromagnetic calorimeter (γ CAL), depositing their energy. The scintillation light produced in the $PbWO_4$ crystal under test was readout by a Silicon PhotoMultiplier (SiPM).

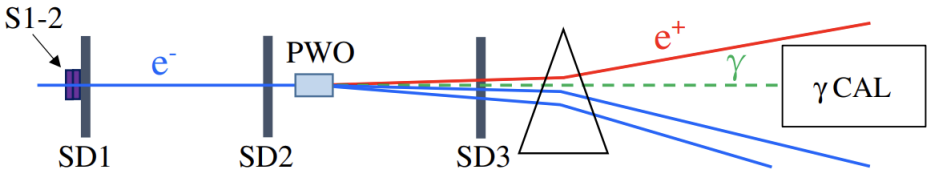

Figure 2.3: Experimental setup used during the tests on a 4 mm thick $PbWO_4$ crystal at the CERN North Area: S1-2 represent the two plastic scintillators for the trigger generation, SD1 and SD2 the two tracking telescopes, SD3 the multiplicity counter, the white triangle the bending magnet, while γ CAL is the downstream electromagnetic calorimeter. Figure from [41].

Figure 2.4 shows the calorimeter spectra obtained collecting all the photons originated in the $PbWO_4$ crystal when 120 GeV electron beams impinged on it, in three different lattice-to-beam orientations. In the random configuration (when the beam was not aligned with any crystallographic direction of the lattice), the energy spectrum decreases, according to the Bethe-Heitler formulation of the e.m. radiation emission by a charged particle.

On the other hand, in axial and planar alignment the calorimeter spectrum was strongly modified: the photon spectrum, in both cases, showed a hardening in the high energy region. This confirmed that the development of the electromagnetic shower undergoes an acceleration along a crystalline axis or plane.

2.2.2 The *STORM* project

The promising results obtained from the collaboration in 2017-2018 have led to another project called *STORM*. *STORM* was a two year project, started in 2021, which aimed at further investigating the $PbWO_4$ performances when oriented with the beam direction. During the beamtest performed in August 2021 by the *STORM* team at the CERN North Area H2 beamline, two $PbWO_4$ crystal samples with a thickness of 1 and 2 X_0 were tested. The experimental setup is sketched in figure 2.5. The two scintillators (S1+S2) generated the trigger when crossed by a particle. The two telescopes (T1 and T2) were used

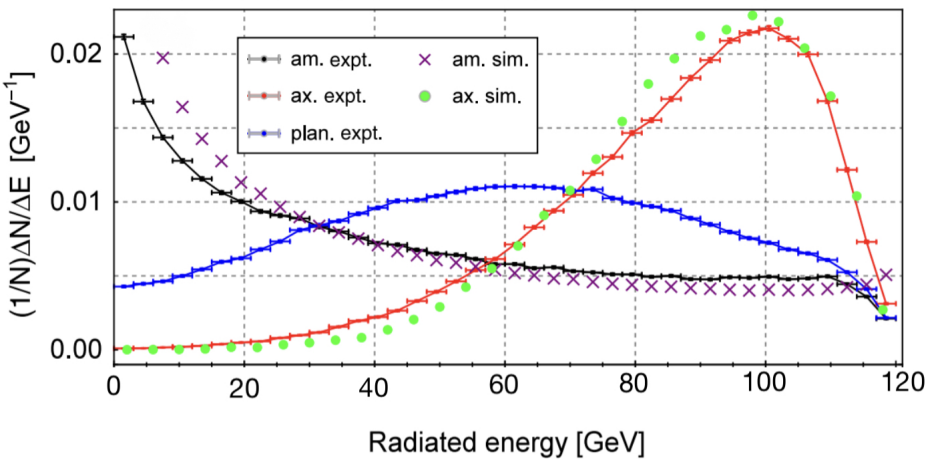

Figure 2.4: Experimental and simulated calorimeter spectra with 120 GeV electron beams in three different orientations: random, axial (the beam was aligned with the <001> axis) and planar (the beam was aligned with the (100) plane). Figure edited from [41].

for the particle tracking, to measure the misalignment angle with respect to the crystallographic direction. The crystal sample under test was mounted on a high-precision goniometer and the scintillation light was readout by SiPM matrices, whose main properties will be presented in subsection 3.2.4. Moreover, the multiplicity of the electrons and positrons generated in the interaction of the beam with the crystal was measured by a plastic scintillator used as a multiplicity counter (MC): the MC output was exploited to estimate the enhancement of charged particles production within the oriented crystal samples. The generated particles crossed the first beam chamber (BC1) and a bending magnet (BM) which swept away the charged particles. The remaining photons crossed the second beam chamber (BC2) and interacted with the downstream electromagnetic calorimeter (GENNI), depositing their energy. Further details on the experimental setup are available in [5].

Both the crystal samples in axial lattice-to-beam orientation showed a substantial enhancement in the energy deposit, readout directly by the SiPM matrices. Figure 2.6 shows the SiPMs spectra, for different lattice-to-beam angles, for the $2X_0$ sample. The spectrum acquired in axial orientation (i.e. when the beam was perfectly aligned with the <001> crystal axis), was ~ 3 times larger than the one acquired in random orientation. Moreover, the random spectrum and the axial one differ in shape: the former can be described by a Landau distribution while the latter by a Gaussian curve [5]. A

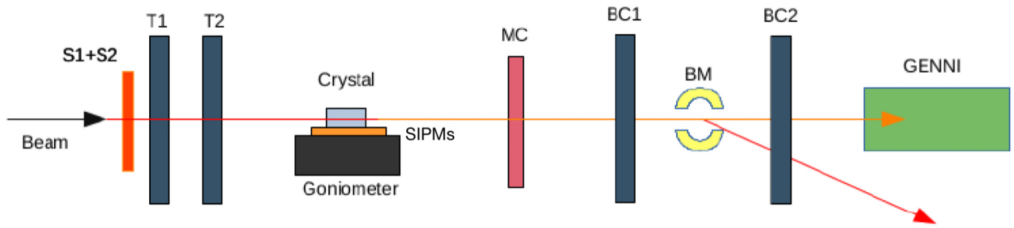

Figure 2.5: Experimental setup used during the 2021 *STORM* beamtest: S1+S2 are the scintillators used for the trigger, T1 and T2 the silicon telescope modules of the tracking system, MC the scintillator readout by a PMT used to count the multiplicity of the crossing particles, BC1 and BC2 are the beam chambers in the midst of which the bending magnet (BM) was used to sweep the charged particles. In the downstream part of the setup an electromagnetic calorimeter (GENNI) was present. Figure from [5].

comprehensive treatment regarding the experimental results obtained during the *STORM 2021* beamtest is available in [5, 6]. During the last *STORM* beamtest, which took place in August 2022 at the CERN H2 extracted beamline, another $PbWO_4$ crystal ($4.6X_0$ thick) was tested. The experimental setup and the data analysis are the main subject of this thesis and they will be discussed in the next chapters. The main task of the *STORM 2022* beamtest was to further investigate the acceleration of the e.m. shower development in an oriented crystal, quantifying analytically the reduction of the radiation length due to the effects induced by the crystalline structure in the Strong Field regime, and thus evaluating the feasibility of a calorimeter composed by $PbWO_4$ crystals oriented with respect to the particle source. Moreover, the data analysis will be supported by the Monte Carlo simulation toolkit Geant4 [42] (details in Appendix A).

2.3 Oriented crystals applications in physics

Oriented crystals exhibit unique properties that make them ideal for the development of technological devices for high energy physics and astrophysics. The following sections will present a few possible future applications of oriented crystals. The development of such technologies is still underway, as further tests are required to:

- expand the knowledge on the underlying physical phenomena which occur in crystal lattices when they are oriented with a particles source;

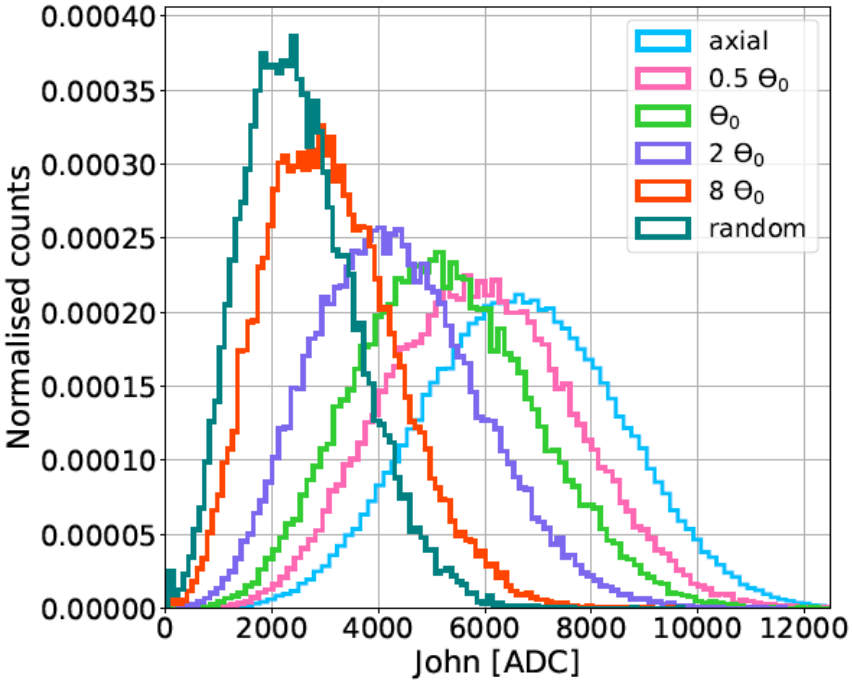

Figure 2.6: Normalized energy spectrum readout by one of the SiPM matrices. Different colors correspond to different lattice-to-beam orientations: the angles are shown in the figure label and they are expressed in units of the Baier angle [5].

- obtain the parameters required by the simulations to improve their capability to reproduce the experimental outcome;
- find an efficient system capable of aligning the particle source with the required crystallographic direction with high precision.

2.3.1 A positron source for the future e^+/e^- colliders

Despite their small center of mass energy, lepton-antilepton colliders are well suited for high precision measurements of the Standard Model (SM) mechanisms, given that the colliding particles are elementary thus offering a very clean collision environment [43]. An efficient positron source is a key element in the design of a e^+/e^- collider. While the electrons can be stripped from hydrogen atoms, the production of antiparticles is a more challenging task. The current scheme, typically used for the production of positrons to be injected into the accelerating system, is depicted in figure 2.7(a). It consists in a thick (several X_0) target material with high-Z and high-density, such as tungsten, within which an impinging electron starts an e.m. shower: photons are produced via bremsstrahlung and in turn create electron-positron pairs. Positrons are then selected with bending magnets and injected into the accelerating system. However, this conventional method for the positron production presents several drawbacks caused by the high thermal dissipation of the energy deposited within the target and by the material damages induced by the high radioactivity [44]. Moreover, the target heating due to the high intensity of the electron beam impinging on the target itself is not uniform along the beam direction. In fact, the maximum number of particles is generated along the e.m. shower at a depth into the material equal to t_{max} (equation 2.1). As a consequence, the energy deposit is not uniform along the target material thus resulting in a temperature gradient [43]. As already observed in the SLC (SLAC Linear Collider) target, the temperature gradients cause mechanical stresses that may break the target itself [45].

Given the severe issues related to the heating of the target and its becoming radioactive, the conventional method for the positrons generation is not suitable for the future high intensity lepton-antilepton colliders, such as the FCC-ee (Future Circular Collider) one[1] [46]. Nowadays, a new type of positron source based on oriented crystals is under study. This new technology exploits a working scheme composed of two stages: a crystal-based radiator which generates photons and a conventional high-Z and high-density photon converter for the positrons production.

The working scheme of such a hybrid positron source is represented in

[1]For the FCC-ee a positron bunch intensity of 2.1×10^{10} particles is required.

figure 2.7(b). As previously described, when an axis or a plane of the crystal radiator are oriented with respect to the electron beam direction, the emission of radiation undergoes an enhancement due to channeling radiation and coherent bremsstrahlung, thus improving the positrons production in the second stage. Moreover, separating the radiator from the converter, the thermal dissipation and thus the mechanical stresses are attenuated [43]. The crystal-based positron source can be further optimised inserting between the radiator and the target converter a collimation system (figure 2.7(c)) or a bending magnet (figure 2.7(d)). The former can be used to cut the beam tails while the latter to sweep away all the charged particles from the target converter angular acceptance [47]. The e+BOOST (intense positron source Based On Oriented crySTals) italian project is a two year Italian collaboration funded by MUR (Ministero dell'Università e della Ricerca), which will test the feasibility of a crystal-based positron source for generating intense unpolarized positron beams. This new positron source could be potentially employed in the Future Circular Collider project.

2.3.2 OREO

The OREO (ORiEnted calOrimeter) INFN project, started in 2023, represents the continuation of the *STORM* one, and focuses on the investigation of oriented $PbWO_4$ crystals. The OREO project aims not only at improving the study of the performances of $PbWO_4$ crystals but also at assembling a prototype of a homogeneous electromagnetic calorimeter composed of oriented crystals. OREO will develop a prototype of a PWO-UF ($PbWO_4$ Ultra Fast) calorimeter, as presented in figure 2.8.

It consists in [48, 49]:

- a 3×3 array of $5X_0$ $PbWO_4$ crystal samples with a transverse area of 2.5×2.5 cm^2 [6], which will have the <100> crystal axes aligned with the beam direction;
- a conventional 3×3 array to contain completely the electromagnetic shower.

Despite the promising results of the preliminary studies on $PbWO_4$ crystals, which unequivocally demonstrate the acceleration of the development of the electromagnetic shower within the crystals themselves, the construction of a prototype calorimeter based on these oriented crystals presents technical issues that need to be overcome. The biggest challenge lies in the simultaneous alignment of 9 crystals, which must have the same lattice-to-beam angle. In order to achieve such an alignment the crystals should be glued together

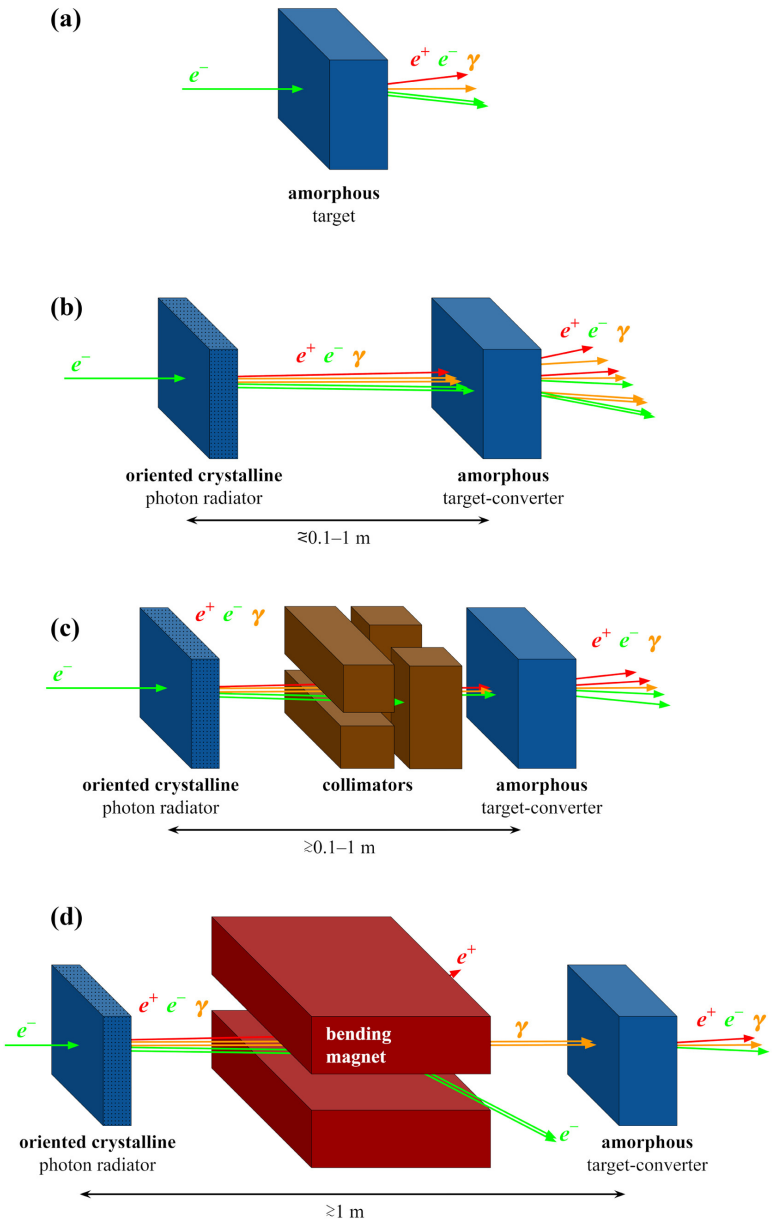

Figure 2.7: (a) Conventional positron source, consisting in a high-Z, high-density material within which an e.m. shower generates positrons. (b) Hybrid scheme for the positron generation: an oriented crystal works as a radiator while an amorphous target-converter generates an e.m. shower. (c) Hybrid positron source optimized with collimators and (d) with a bending magnet. Figure from [47].

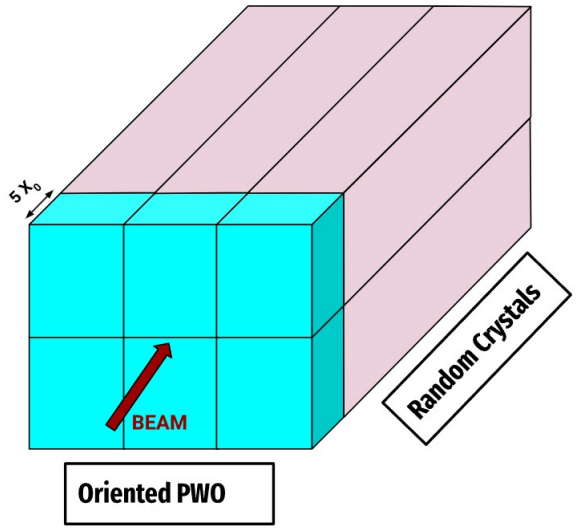

Figure 2.8: Schematic representation of the OREO prototype. The first five radiation lengths will be covered by a 3×3 matrix of oriented crystals while the downstream stage is composed by not oriented crystals (in random orientation).

with their <100> axes aligned between themselves, and then placed inside a plastic holder in order to prevent misalignments caused by external agents [6]. During two different beamtests the OREO collaboration tested two crystal arrays: a 3×1 row and a 2×2 matrix. Highly encouraging results on the feasibility of the simultaneous alignment of more crystal samples have been obtained; the data analysis is being performed to publish the first results.

2.3.3 High energy physics and satellite-borne calorimeters

Electromagnetic calorimeters are devices widely used in high energy physics. The employment of oriented crystals for the development of electromagnetic calorimeters would bring several advantages, the main one being the reduction of the material budget required to fully contain an electromagnetic shower, as explained in section 2.1. Moreover, such next-generation crystal based calorimeters would also improve the effective performances with respect to the current-generation ones. For instance, the reduction in the shower length in oriented crystals would improve the crystal-based calorimeter energy resolution, that will be briefly introduced in subsection 4.2.3, thanks to a

better longitudinal energy containment.

Another aspect that makes the crystal technology appealing for the development of the next-generation e.m. calorimeters is that it could improve the discrimination efficiency between charged leptons and charged hadrons and between photons and neutral hadronic particles (e.g. neutrons). In fact, the coherent effects induced by the crystal lattice affect only the electromagnetic processes and not those mediated by the strong force. As a net effect, the radiation length X_0 is reduced by the lattice orientation while the nuclear interaction length λ_{int}, i.e. the longitudinal scale of the inelastic hadronic processes, is unaffected by the lattice orientation.

Since only the energy deposit of the first radiation lengths crossed by an incident particle is influenced by the lattice-to-beam orientation, as explained in section 2.1, the prototype of a calorimeter based on oriented crystals, able to perform particle identification would feature a hybrid design: the first radiation lengths would be covered by a layer of oriented crystals aimed at performing the discrimination between hadrons and leptons, followed by a stage of several radiation lengths of thickness, consisting in an e.m. calorimeter composed by not oriented crystals to measure the initial particle energy.

The working scheme of such a hybrid calorimeter, capable to perform the lepton-hadron discrimination, coincides with the OREO one, presented in figure 2.8.

However, the OREO second stage, composed by an e.m. homogeneous calorimeter, is not ideal to perform an efficient particle identification since it provides a limited information on the longitudinal development of the electromagnetic shower. A possible improvement would consist in replacing the second stage of the hybrid calorimeter with a "sampling-like" e.m. calorimeter, composed by not oriented crystals, as sketched in figure 2.9. Such a calorimeter would allow to reconstruct the shower profile, with an accuracy determined by the longitudinal and transverse sampling pitches, further improving the discrimination efficiency between different types of particles.

Since their improved capability to fully contain an electromagnetic shower, the crystal based electromagnetic calorimeters are well suited also for the development of satellite-borne γ-ray detectors, whose working scheme is depicted in figure 2.10:

- the impinging photon hits high-Z and high-density conversion foils within which it undergoes pair production. Silicon detectors reconstruct the electron and positron tracks, allowing to determine the opening angle between the pair of charged particles and thus the γ direction;

- a calorimeter is used to measure the energy of the electron-positron

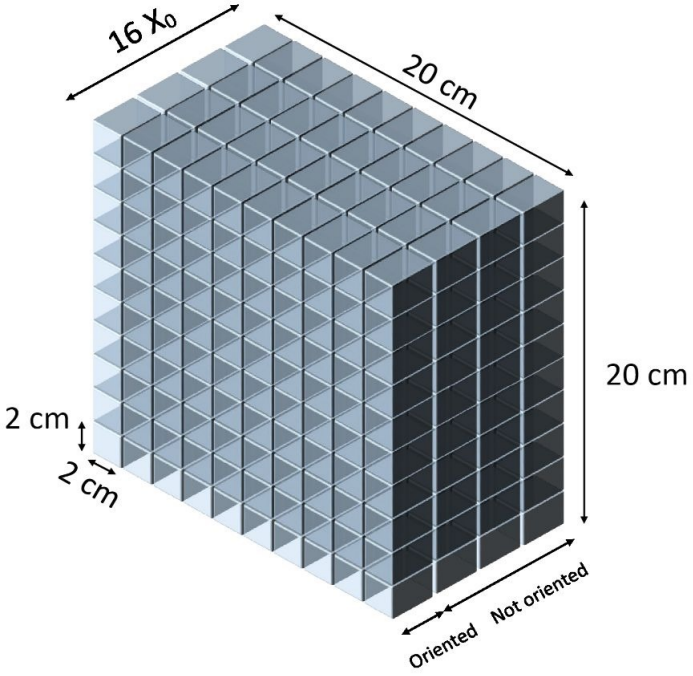

Figure 2.9: Schematic representation of a next-generation e.m. sampling calorimeter: the first 4 radiation lengths would consist in a layer of oriented crystals aligned with the particle beam, while the following layers in a "sampling-like" e.m. calorimeter not oriented with the beam. Figure from [48].

pair, generated in the conversion foils, and thus to compute the initial photon energy;

- the telescope module is surrounded by segmented tiles of plastic scintillators working in anti-coincidence mode, in order to reject the background of charged particles[2].

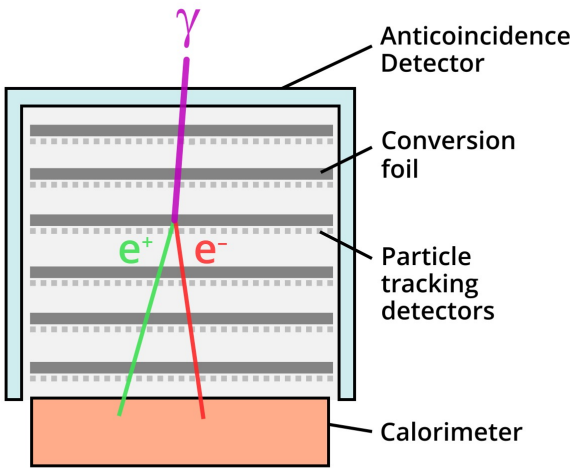

Figure 2.10: Working scheme of a γ-ray satellite-borne detector.

The current most performing satellite-borne γ-ray detector is the Fermi Large Area Telescope (LAT) [51] (figure 2.11). It consists of 16 telescope modules, each one made of W converting foils and silicon tracking detectors, followed by a $10X_0$ CsI electromagnetic calorimeter [50].

A possible improvement to the operating scheme of a satellite-borne telescope could be the use of tungsten crystalline conversion foils and a source-pointing calorimeter based on oriented crystals. This choice would yield the following benefits [53]:

- the crystalline lattice of the W conversion foils, when perfectly aligned with the γ source, would enhance the pair production rate, according to the theoretical framework presented in subsection 1.4.1;

[2]The typical value of the charged cosmic rays background flux experienced by a low-orbit γ-ray telescope is $\sim 10^5$ times larger than the γ one [50].

Figure 2.11: Illustration of the Fermi telescope in orbit around the Earth [52].

- the acceleration of the electromagnetic shower development in the electromagnetic calorimeter, when aligned with the γ source, would lead in a better energy containment thus reducing the longitudinal energy loss due to the finite length (in units of X_0) of the calorimeter, with the improvement of the calorimeter energy resolution;
- the employment of oriented crystals would lead to a better photon-hadron discrimination.

Such a crystal-based telescope may be employed to further investigate the unidentified Fermi γ-ray sources and multimessenger sources, as well as to point the galactic center for the dark matter decay lines detection [53].

In this chapter, the main aspects regarding the feasibility of the oriented calorimeters development have been discussed, including the key experimental results obtained from the collaborations preceding the *STORM* one, and the potential practical applications of such next-generation technology. The next chapter will introduce the beam facility and the main components of the experimental layout exploited during the *STORM 2022* beamtest.

Chapter 3

STORM 2022 Beamtest

To explore the development of electromagnetic showers in oriented crystals, an appropriate scintillating crystal sample and a light detection system are essential. They have to be tested on a particle beam to measure the performance and the improvement with respect to a calorimeter consisting of not oriented crystals. This chapter will focus on the facility where the tests have been performed describing all the elements of the setup.

3.1 The CERN North Area

The beamtest took place in August 2022 in the CERN North Area to investigate coherent effects in crystals (such as the Strong Field ones). CERN is the largest and most important laboratory for high energy physics in the world, located along the Swiss-French border. The CERN accelerator system is presented in figure 3.1 and consists in several stages:

- the Linac4, a linear accelerator that accelerates hydrogen H^- ions up to 160 MeV;
- the Proton Synchrotron Booster (PSB) in which the protons, obtained from the H^- atoms, are injected and accelerated up to 2 GeV;
- the Proton Synchrotron (PS), that increases the energy up to 24 GeV;
- the Super Proton Synchrotron (SPS), which is a 7 km diameter accelerator, with 1317 hot (not superconducting) magnets. The SPS increases the energy up to 450 GeV [54];
- the Large Hadron Collider (LHC), a 27 km ring where protons are accelerated up to 7 TeV for physics collisions.

Both the PS and the SPS provide particles to extracted beamlines for detector tests and physics experiments. In particular the SPS has 6 extracted lines, two of which feed the NA62 and COMPASS experiments. The remaining ones are the H2, H4, H6 and H8 beamlines which are located in the Experimental Hall North 1, on the French site, more precisely in Prévessin [55]. Even though the primary beam consists of protons, it is possible to produce many other particle types. Along the acceleration lines, fixed targets of different materials and thickness can be placed to allow protons interact with matter and produce different particle types with different energies. The collimators, located on the beamlines, allow to shape the beam, while dipoles and quadrupoles allow to select the energy and type of charged particles.
For the 2022 beamtest, electron beams were selected, with an energy between 20 and 120 GeV. The beam was expected to have a high purity with an acceptance $\Delta(p)/p = 2\%$, where p is the electron momentum and $\Delta(p)$ its variation [56].
In fact the 2022 H2 beams were less pure, both in particle type and in energy spectrum, as will be described in section 4.3.

3.2 The beamline layout

The beamline is presented in figure 3.2(a) while the schematic representation of the whole experimental setup is shown in figure 3.2(b).
The latter consists of:

- two plastic scintillators for the trigger system;
- two microstrip silicon detectors (T1, T2) for particle tracking;
- a uniform field bending dipole magnet, which allows to horizontally sweep the charged particles of the primary beam, if needed;
- two $PbWO_4$ crystal samples of $4.6X_0$ assembled very close to each other along their longest side, coupled to Silicon PhotoMultipliers (SiPMs). The crystals are mounted on a goniometer placed on a XSCA table, both remotely controlled;
- seven lead glass calorimeters of the *OPAL* experiment readout by PhotoMultiplier Tubes (PMTs).

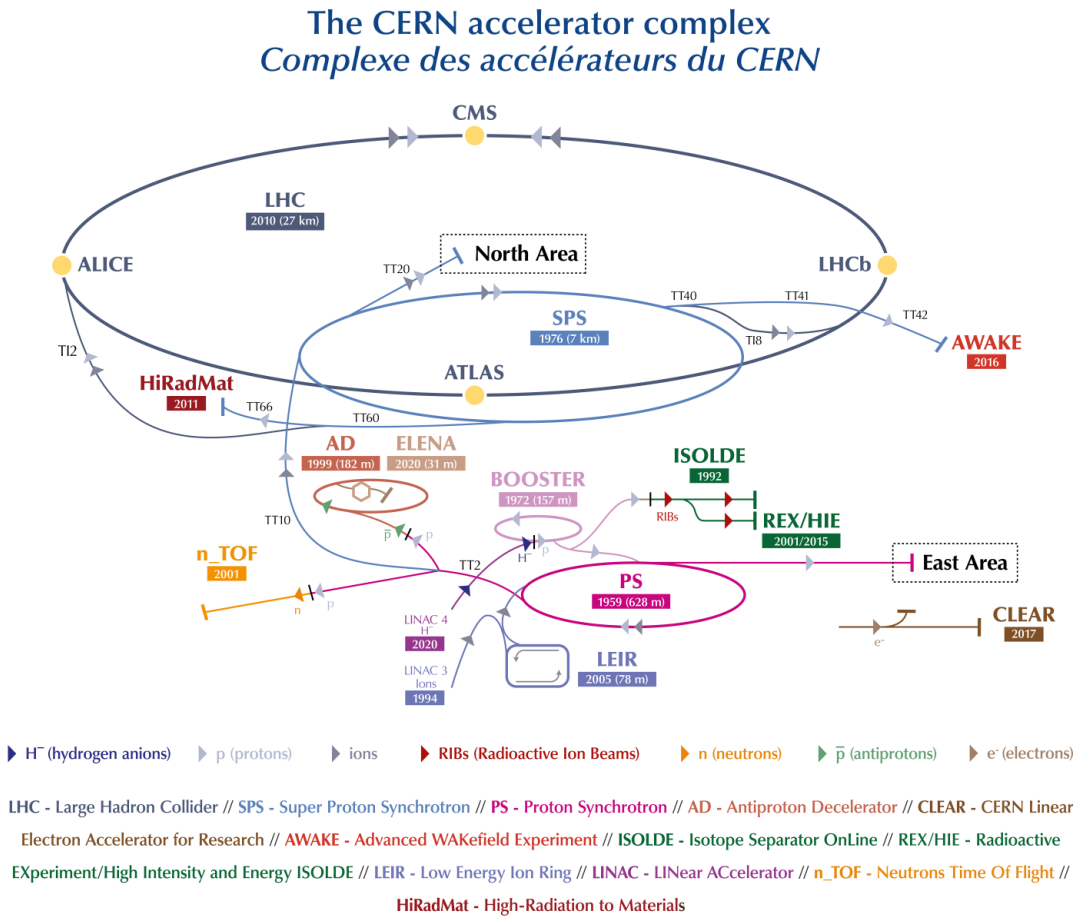

Figure 3.1: CERN accelerating system [54].

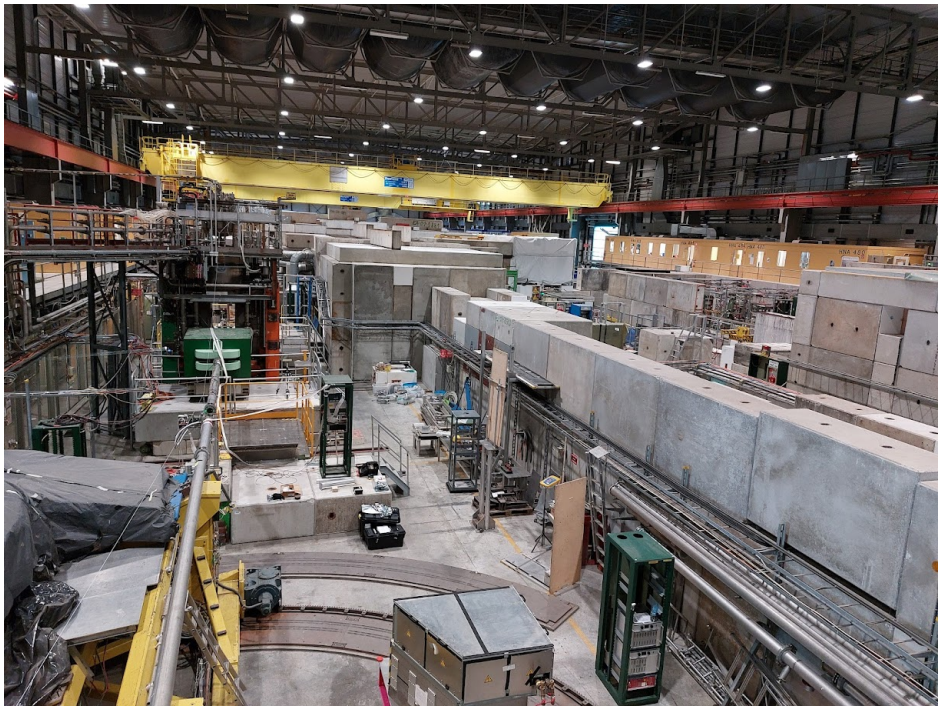

(a)

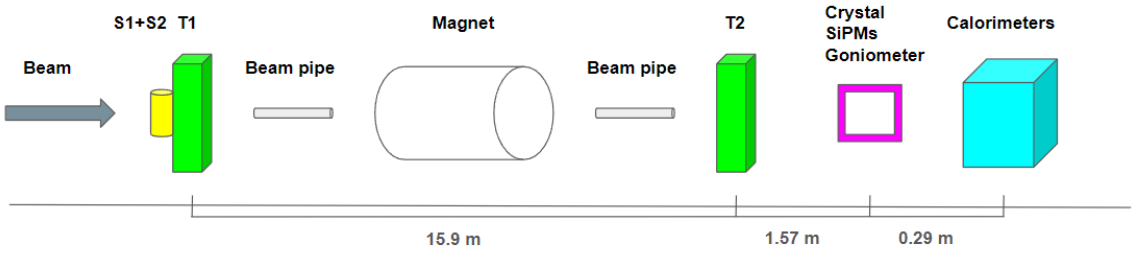

(b)

Figure 3.2: (a) Top view photo of the beamline in the H2 experimental area. (b) Sketch of the experimental setup along the beamline. S1+S2 are the trigger scintillators, T1 and T2 the telescopes for the tracking system; the vacuum beam pipes (the gray cylinders) reduce the air multiple scattering contribution. The rectangular frame represents the crystal-SiPM setup, and the large cyan box the lead glass calorimeters.

3.2.1 The trigger system

The trigger system is a fundamental part of the acquisition chain. The system designed for the *STORM* beamtest has a dimension that allows to select the central part of the beam in order to maximize the number of events in the crystal area.
During the 2022 beamtest, the trigger system was composed of two plastic scintillators (S1 and S2) in direct contact with the first telescope (T1) as shown in figure 3.3. The scintillator thickness is 7 mm and its section 4×9 cm^2. The first scintillator met by the beam has a hole in the center with the shape of a slit, with a width of 3.5 mm [5], in order to have the two scintillators working in anticoincidence: the trigger is generated when there is no signal in S1 and a signal in S2, defining in this way a trigger region corresponding to the slit.

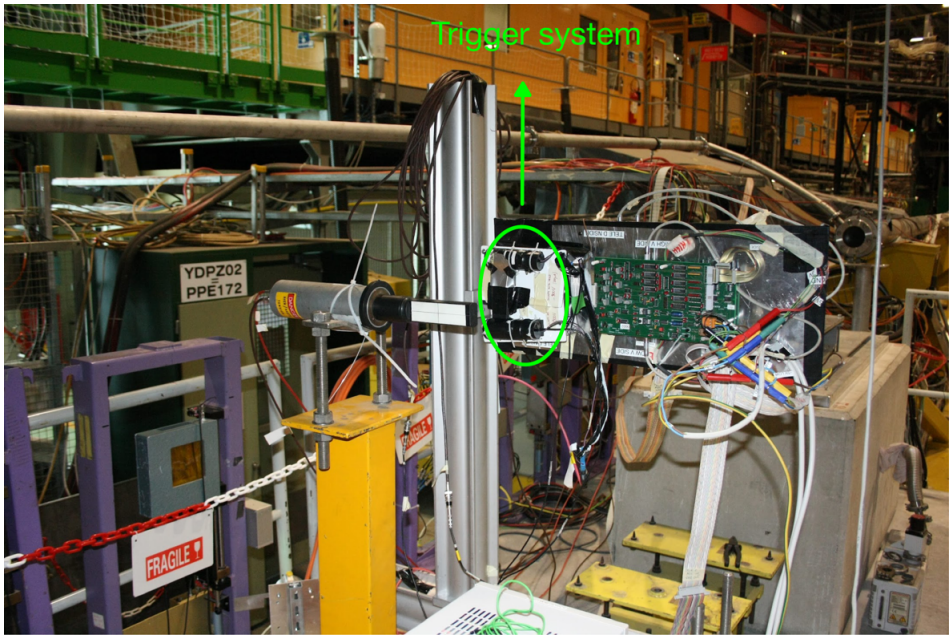

Figure 3.3: T1 telescope module, with the trigger system highlighted, consisting of plastic scintillators readout by two PMTs (the black cylinders).

Furthermore at CERN particles are sent in bunches and the single bunch is called spill. A single spill lasts about 4 s in a cycle of 20-45 s[1]. The accelerator monitoring system provides the spill signal that is used in the

[1]The cycle duration depends on the machine settings and on the priorities among the experiments.

trigger generation to acquire particles only during the spill. Thus the trigger is given by the coincidence of the spill with $\overline{\text{S1}} \wedge \text{S2}$, where $\wedge$ denotes the logic and.

3.2.2 The tracking system

The tracking system consists in two 300 µm thick double-side silicon strip detectors, with a sensitive area of 1.92×1.92 cm^2, produced by CSEM [57]. One module is shown in figure 3.4(a) and the main features are listed in table 3.1. Such detectors allow a very good spatial resolution without introducing a too large contribution of the multiple scattering due to their small thickness [58].

The telescope junction side (p^+ side of the Si substrate) has 384 strips with a readout pitch of 50 µm, while the implant pitch is 25 µm. Between two readout strips there is a floating one, not readout by the electronics, with the aim of improving the spatial resolution [59]. On the other hand the ohmic side, perpendicular to the junction one, has 384 physical strips with a pitch of 50 µm, with no floating ones, separated by p^+ blocking strips. The depletion voltage is in the range 36-54 V and the leakage current is $\sim$ 1.5-2 nA [60]. Each silicon module is readout by three VA2 ASICs, produced by IDEAS [61] and shown in figure 3.4(b).

The VA2 ASIC is a 128 channel radiation tolerant integrated circuit built with the 1.2 µm N-well CMOS technology.
Each ASIC consists of:

- a low power folded cascode preamplifier;
- a CR-RC shaper;
- a sample & hold circuit to sample the analog signal and save its value in a capacitor upon receiving the hold digital signal.

The analog signals are multiplexed on a single output line, with a clock with a maximum frequency of 10 MHz. The telescope silicon detectors are DC coupled; for the AC coupling with the electronics, external quartz capacitors are used.

The detector silicon tile and the ceramic hybrid (which houses the ASICs) are mounted on a fiberglass support, as shown in figure 3.4(b). The fiberglass support and the first part of the readout electronics are contained in an aluminum box.

The frontend electronics of each detector is composed of the repeater boards (one per side) and of the optocoupler board. The repeater board tasks are the following:

- biasing the tracking detectors and the ASICs;
- performing the initial signal conditioning;
- amplifying the multiplexed analog output coming from the hybrid.

The silicon detectors on the ohmic side do not have a ground level at 0 V but they are referenced to the bias voltage (in the range $18 - 54$V), in order not to have a large potential difference across the coupling capacitor. For this reason, optocoupler boards are used as level adapters: they shift the DC level of the signals to and from the n-side of the junction.

The signals are then processed by the acquisition electronics. The readout phase can be summarized as follows:

1. the analog sampled signals are sent to the ADC (Analog to Digital Converter) boards. Each ADC board is located close to a telescope and can read out up to 4 silicon planes with an AD9220 12 bit ADC (Analog Devices [62]) [60];
2. the digitized signals are sent to the VME Readout Boards (VRBs) as low-voltage differential signals. The digital signals are stored in a dedicated buffer and sent to the Data AcQuisition (DAQ) PC by means of the VME bus [63] in the interspill period. The VRBs are able to operate in zero-suppression mode: only the strips with a signal larger than a user defined threshold are stored [60].

3.2.3 $PbWO_4$ crystal samples

Lead tungstate crystals are ideal detectors for electromagnetic calorimetry, because of their large atomic number and density. Table 3.2 presents the main physical properties of $PbWO_4$.
The small values of the radiation length and the Molière radius allow to build compact calorimeters, whose output, which is the scintillation light emitted by the crystals, can be read out by photodetectors such as Silicon PhotoMultipliers. Lead tungstate calorimeters are typically assembled in random orientation. However, if the crystals strongest axes (such as <100>, the axis under study in this thesis) were oriented with the beam direction, particles would experience a stronger lattice potential with respect to the not oriented configuration, as described in subsection 1.3.5. This effect makes particles stop in a shorter distance, allowing to produce compact oriented calorimeters. Table 3.3 presents the crystal properties while figure 3.5 shows the PWO periodical crystal lattice, with superimposed two axes.

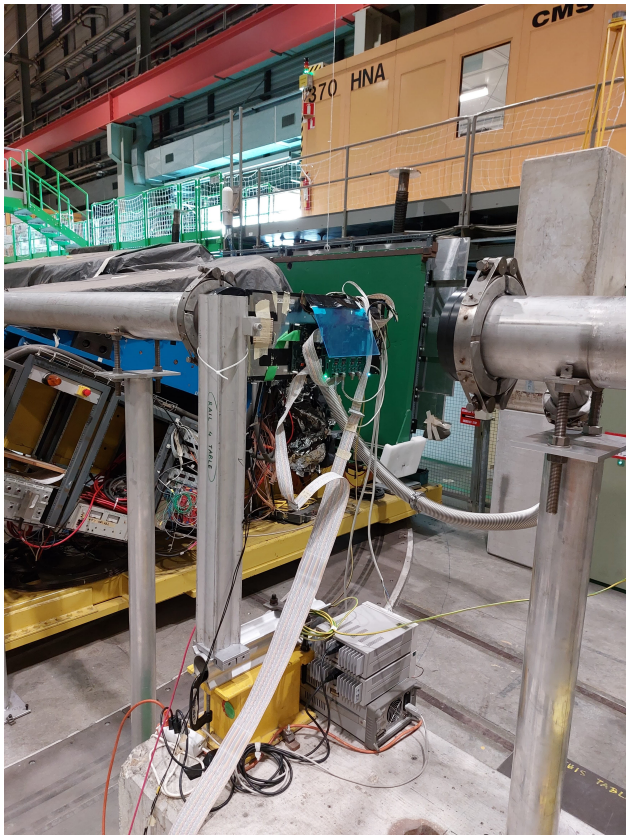

(a)

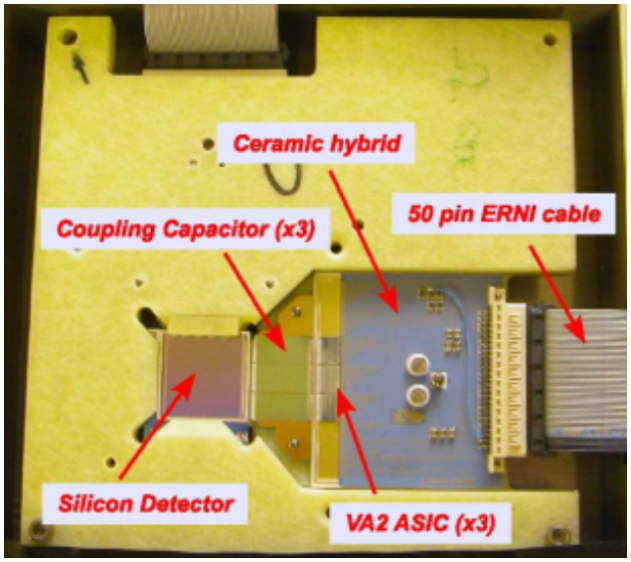

(b)

Figure 3.4: Telescopes silicon detectors. (a) The telescope between two beam pipes in the H2 experimental area. (b) The telescope silicon detector on the fiberglass with the ASICs and coupling capacitors.

Table 3.1: Main physical properties of the double side telescope [60].

Detector	Double side
Manufacturer	CSEM
Detector dimensions [cm^2]	1.92×1.92
Number of readout channels	384
Bulk thickness [µm]	300
Resistivity [kΩ·cm]	> 4
Leakage current [nA/strip]	> 1.5-2
Full depletion voltage [V]	36-54
p-side	
Physical pitch [µm]	25
Readout pitch [µm]	50
Floating scheme	yes
Spatial resolution [µm]	~ 5 [60]
n-side	
Physical pitch [µm]	50
Readout pitch [µm]	50
Floating scheme	no
Spatial resolution [µm]	~ 11.6 [60]

Table 3.2: Main physical properties of $PbWO_4$ [64].

Radiation Length [cm]	0.8903
Pion interaction length [cm]	24.04
Molière radius [cm]	1.959
Z/A	0.41315
Density [$g \cdot m^{-3}$]	8.3
Light Yield (rel. NaI) [%]	0.3

From table 3.3, it can be observed that the acceptance angle for the Strong Field effect (Θ_0) is of the order of 1 mrad, which is the reason why a small beam divergence is required.
Table 3.4 presents the properties of the crystals under test (figure 3.6).

Table 3.3: Main properties of the $PbWO_4$ crystal [5, 6].
$d_{lattice}$ is the interatomic pitch, U_0 the electromagnetic potential depth, Θ_0 the Strong Field angular acceptance, and SF threshold the energy limit below which the effects of the Strong Field are negligible (see subsection 1.3.5).

axis	<100>	<001>
d_{lattice} [Å]	5.456	12.020
U_0 [eV]	464	420
Θ_0 [mrad]	0.908	0.822
SF threshold ($\chi = 1$)	$\sim 30\,\text{GeV}$	$\sim 30\,\text{GeV}$

Table 3.4: Main physical properties of the $PbWO_4$ crystal samples under test. The main axis considered in this thesis to study coherent effects is the <100> one.

Axis	<100>
Lattice geometry	Tetragonal [10]
Thickness [mm]	41
Thickness [X_0]	4.6
Transversal size [mm^2]	30×30
Surface mosaicity [µrad]	250

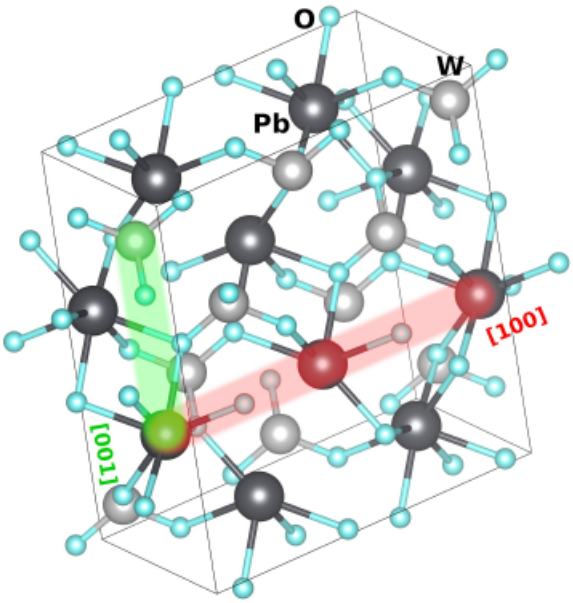

Figure 3.5: Lead tungstate crystal lattice with its strongest axes highlighted (<001>, <100>) [65].

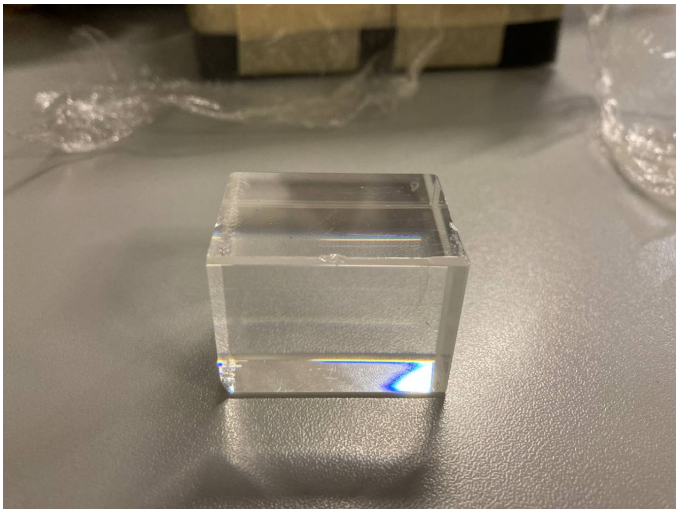

Figure 3.6: Photo of the PWO crystal sample.

3.2.4 The photodetectors

The light generated by the energy deposited in the PWO crystals is readout by SiPMs. SiPMs can be defined as the last generation photodetectors. They are composed by a matrix of pixels on a common substrate with a common output, as schematically presented in figure 3.7. Each pixel is a SPAD (Single Photon Avalanche Diode) that is a reverse biased diode operated in Geiger mode. A SPAD is a digital device: an avalanche is generated whenever one or more photons hit the detector itself. Thus the output signal does not depend on the number of photons. On the other hand, a SiPM consists of a matrix of SPADs connected to the same output. In this way the output becomes proportional to the number of active pixels and thus to the number of photons, but up to a certain limit of saturation: if more photons in fact hit the same pixel, the output will be always the one of a single pixel. If the light intensity is too large with respect to the number of cells, the proportionality is lost. The number of fired pixels (N_{fp}) follows the following relation [66]:

$$N_{fp} = N\Big[1 - \exp\Big(-\frac{N_\gamma \times PDE}{N}\Big)\Big] \tag{3.1}$$

where N is the total number of pixels, N_γ the number of incident photons and PDE is the Photo Detection Efficiency, namely the probability that the detector produces an output signal in response to an incident photon. To switch off the avalanche, a quenching resistor is added to each pixel (poly-Si in figure 3.7).

SiPMs are highly performing detectors, and the main features that make them attractive in a wide range of fields, such as particle and nuclear physics, are the following [66, 68, 69]:

- they are operated at low bias voltages (below 50 V for the newest devices);
- they are insensitive to magnetic fields;
- they have a large intrinsic gain, of the order of $10^5 - 10^6$;
- they have a high PDE defined as:

$$PDE = QE \times P_t \times \varepsilon_f \tag{3.2}$$

  where QE is the detector quantum efficiency, namely the fraction of incident photons which are converted into electrical signals by the detector, P_t the probability that a free charged carrier starts an avalanche, and ε_f the geometrical fill factor that is the ratio between the active area of the

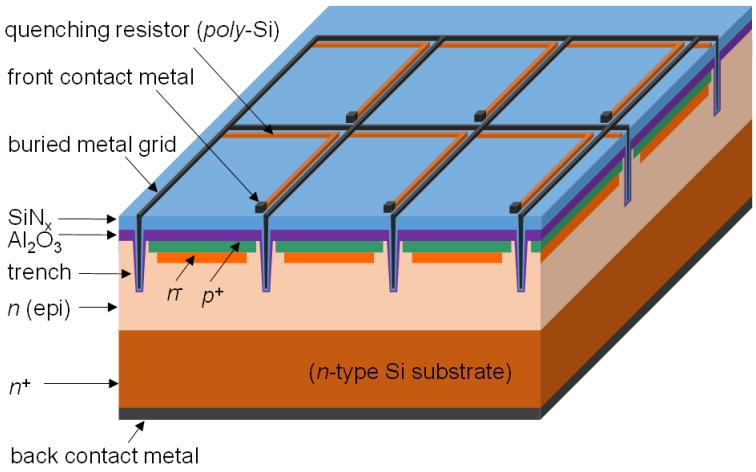

Figure 3.7: Schematic representation of a Silicon PhotoMultiplier detector, with its main elements [67].

pixel and the overall one. Typical PDE values are $20 - 50\%$ depending on the detector features and the incident radiation wavelength;

- they have a wide dynamic range;
- they have an optimal time resolution: nowadays, such detectors can reach values of a few tens of ps.

As far as the limits of SiPMs are concerned, they can be listed as follows:

- limited linearity if the light source is too intense;
- a dark count rate, due to thermal agitation, that is typically in the 100 kHz - a few MHz range at the half photoelectron threshold [70]. To reduce this noise term and maintain it constant, SiPMs can be cooled;
- the optical cross talk [71] that occurs when photons emitted during an avalanche in one cell start a new avalanche in a nearby cell. To limit these spurious events, trenches and grooves for the optical insulation of the single pixel are used [72].

The photodetectors used during the 2022 beamtest are shown in figure 3.8; the board[2] houses 3 SiPM matrices model ARRAYC-60035-4P-BGA [73]

[2]Designed by E.Vallazza, INFN-Sezione di Milano Bicocca, Milano, Italy.

produced by ONSEMI [74], whose main features are listed in table 3.5, while its schematic is presented in figure 3.9. The single ARRAYC-60035-4P-BGA has 4 individual C-series single sensors of 6 mm × 6 mm, arranged in a 2 × 2 geometry. The C-series features low noise, high gain and low voltage sensors, with 18980 35 × 35 µm^2 pixels and a 20 mA maximum current. It is a blue-sensitive SiPM with a high gain in the UV-to-visible region [75].

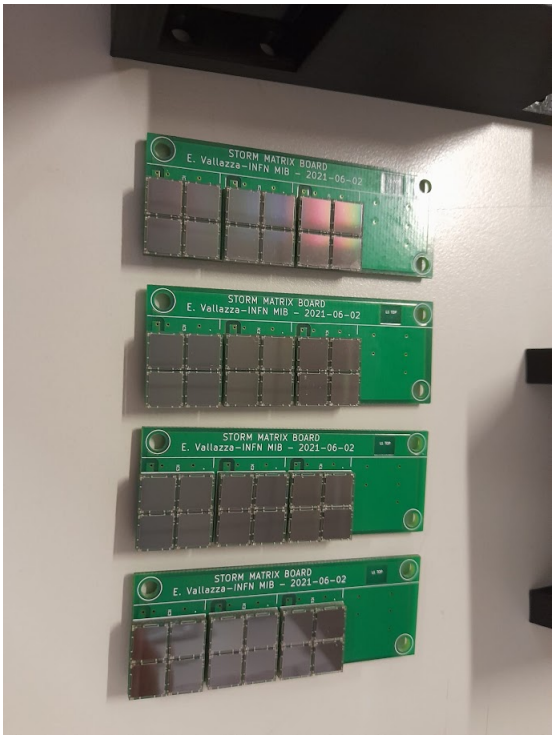

Figure 3.8: *STORM* SiPM matrices; the signal of each matrix is coupled to a 100 nF capacitor and is taken to the readout system with a Hirose connector [5].

All sensors are mounted on a PCB with the Ball Grid Array (BGA) technology; all the anodes are connected to ground while all the cathodes of a single matrix are connected together and to a high pass filter (C = 100 nF, R = 50 Ω that is the input impedance of the digitizer). Sensors have been assembled on the readout board by SCEN S.r.l [76]. The 2 layer PCB (figure 3.10) has a dimension of 63 × 23 mm^2, with a thickness of 1.5 mm [5].

SiPMs work in Geiger discharge mode and thus they are operated at voltages higher (typically 10%-25%) than the breakdown one. The difference between the bias voltage (V_{bias}) and the breakdown voltage (V_{br}) is called overvoltage (V_{over}); for these sensors V_{br} is in the 24.2 V - 24.7 V range [75].

Table 3.5: Main features of the ARRAYC-60035-4P-BGA [73].

Array Size	2×2
Sensor Type	60035
Readout	Pixel
Board Size	14.2×14.2 mm^2
Pixel Pitch	7.2 mm
No. Connections	9
No. Connectors	3×3 BGA

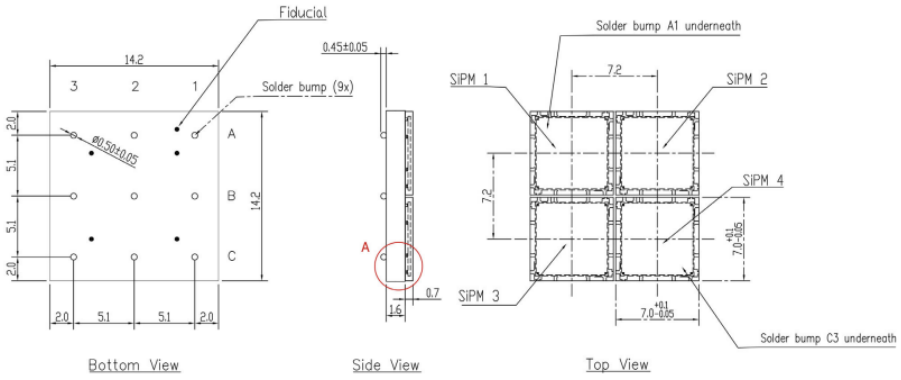

Figure 3.9: Schematic of the SiPM matrix. A1, A2, B1, B2 are the anodes, while A3, B3, C1-C3 are the cathodes connected together [73].

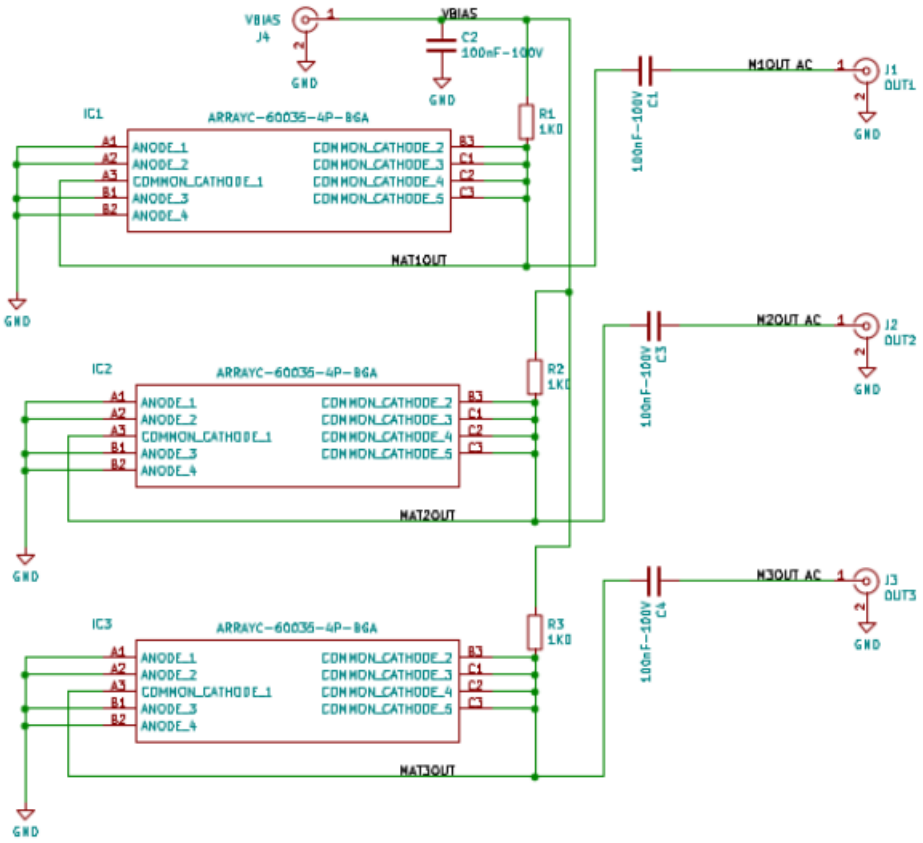

Figure 3.10: Schematic of the readout board: all the anodes (A1, A2, B1, B2) are connected to ground while the cathodes of the single matrices (A3, B3, C1-C3) are connected together thus forming common outputs. The latter are AC-coupled with the digitizer, which has an input impedance $Z = 50\,\Omega$. The biasing circuit includes a 100 nF filtering capacitor and a 1 kΩ limiting resistor for each matrix, to decouple the common bias (VBIAS) for the three arrays.

Figure 3.11 presents the 4 SiPM boards IV curves; during the beamtest the SiPM bias was 30 V.

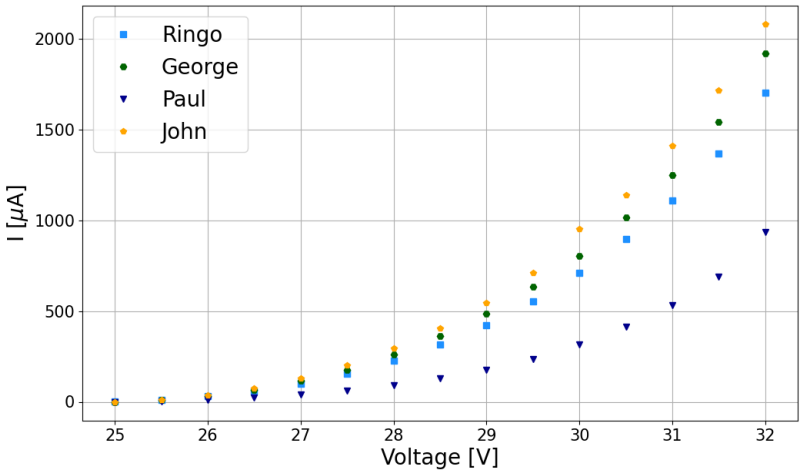

Figure 3.11: The IV curves of the 4 boards (Ringo, George, Paul, John).

As shown in figure 3.12(a), just four matrices were needed to readout each crystal, given its dimension. Figure 3.12(b) presents the sensors location and table 3.6 illustrates their geometry.

Table 3.6: Photodetectors geometry with the SiPM matrices name. The colored ones read out the crystals, while matrices with the same color are connected in parallel thus providing a single current output. NORTH and SOUTH denote the opposite sides, along the x-axis, of the plastic holder housing the SiPMs.

NORTH					
		Ringo1	**George3**	George2	George1
		Ringo2	**Paul3**		
		Ringo3	**Paul2**		
John1	John2	**John3**	**Paul1**		
SOUTH					

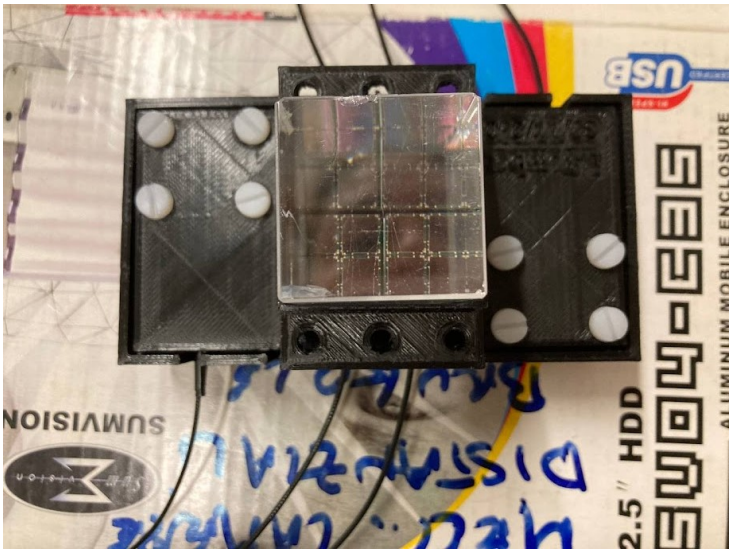

(a)

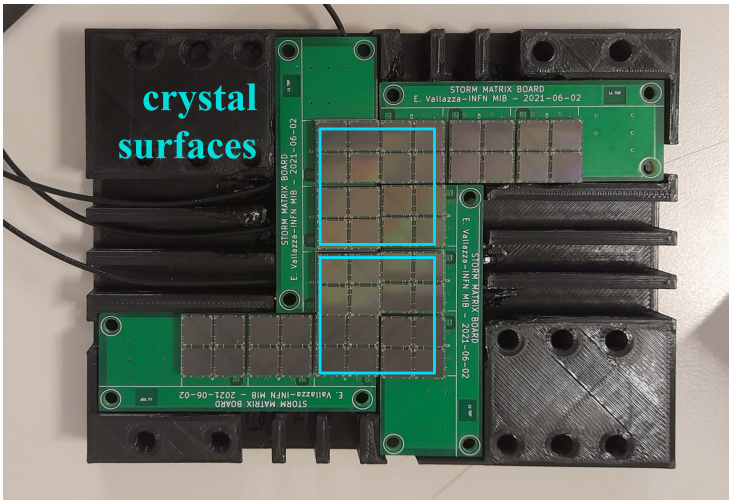

(b)

Figure 3.12: (a) Top view of a PWO crystal sample mounted inside the plastic holder and placed above 4 SiPM matrices. (b) SiPM matrices used for the light readout. The blue lines indicate the regions where the crystals are positioned to be coupled with SiPMs [6].

During the beamtest, only 8 matrices were connected to the digitizer. Additionally, the photosensors were connected in parallel, two by two, thus forming 4 pairs. The parallel-connected pairs are renamed as follows:

- Ringo1 + Ringo2 = Mat1
- Ringo3 + Jhon3 = Mat2
- Paul1 + Paul2 = Mat3
- Paul3 + George3 = Mat4

Figure 3.13 presents a waveform acquired with a 120 GeV electron beam, coming from the third sensor matrix (Paul1 and Paul2). The time window is 500 ns given the fact that signals were sampled by the digitizer at 500 Msample/s. The Data AcQuisition performs the baseline subtraction, storing all the information (the maximum, the time of the maximum with respect to the trigger and the waveform) in the output files.

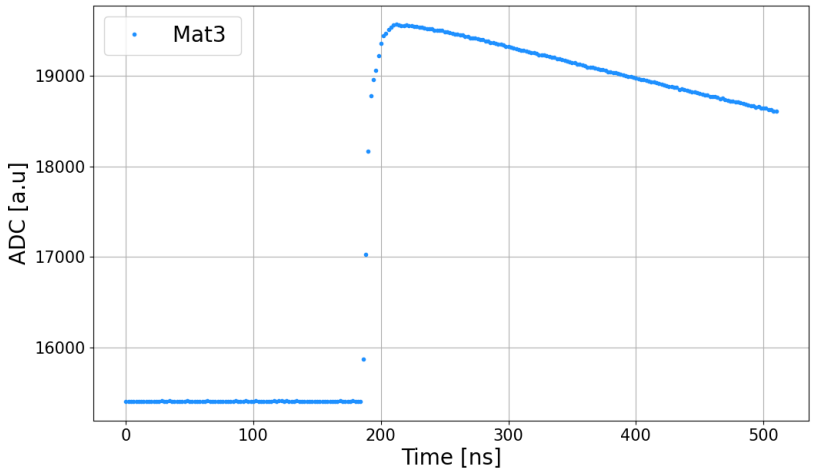

Figure 3.13: Mat3 integrated signal waveform (Paul1 and Paul2) on a 120 GeV electron beam.

As shown in figure 3.13, the *STORM* matrices feature a large time to restore the baseline (recovery time), of the order of a µs. However for this data taking a fast recovery time was not needed because timing measurements were not scheduled.

3.2.5 The goniometer

The angular acceptance of the main effects a particle can experience crossing a crystal requires a system able to align the crystal planes to the beam direction. The Strong Field angular acceptance, for the $PbWO_4$ sample under test, for instance, is ~ 1 mrad (table 3.3). Crystals, during the beamtest, were located on a dedicated goniometer, placed over a remotely controlled XSCA table, as shown in figure 3.14. The goniometer consists of several stages [77]:

- two translational stages, which allow to control the position along the x-direction, perpendicular to the beam one (z). They feature micrometric movements with a 1.5 µrad accuracy, a 2 µrad bidimensional repeatability and a 5 µrad resolution. The range of the upper stage is 102 mm while the range of the lower stage is 52 mm;

- two rotational stages which allow the sample alignment. The lower one (angular stage) performs the rotation in the $x - z$ plane with a range of 360°; the upper stage (cradle) rotates in the $y - z$ plane. Both the stages have an average accuracy of 1 µm, a 1 µm repeatability and a 0.25 µm resolution.

The goniometer is remotely controlled by the DAQ system, which saves the information on the position of each stage in the data files.

3.2.6 The Lead Glasses

The PWO crystals do not contain the complete shower since their length is not enough. To understand the behaviour as a calorimeter, one has to measure the energy not contained in the PWO crystals themselves. For this reason, a set of lead glass calorimeters has been positioned after the crystals.

These calorimeters have been developed for the OPAL (Omni-Purpose-Apparatus at LEP) experiment [78]. They are made of Schott SF57 glass with 76% of lead: the shower generated by the particle produces Cherenkov light[3]. Each block is 37 cm $\sim 24.7X_0$ long, being $X_0 = 1.50$ cm [80]. They have a trapezoidal shape, with a front face of 10×10 cm^2 and a rear one of 11×11 cm^2, as shown in figure 3.15. The calorimeters are covered by black cardboard to protect them from the environmental light. The calorimeter light is read out by a Hamamatsu R9880U-110 PMT [81], a high gain PhotoMultiplier

[3]Cherenkov radiation is a phenomenon that occurs when a charged particle crosses a medium at a superluminal velocity in the medium itself, resulting in the emission of light, typically in the blue-UV region of the electromagnetic spectrum [79].

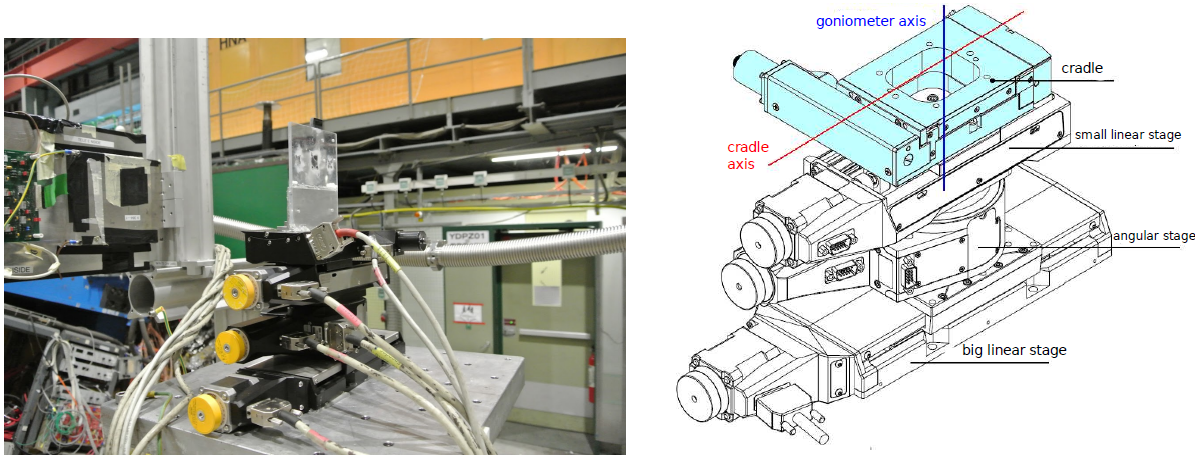

Figure 3.14: (a) Photo of the goniometer on the H2 line during the 2021 *STORM* beamtest. (b) Schematic of the goniometer with its main stages: two linear and two rotational ones [5].

Tube, biased in the 900-1000 V range. The block transverse half-size is $\sim 5.5\,\text{cm} \sim 2.13\ R_M$, being the Molière radius $R_M = 2.578\,\text{cm}$ [82].

As it will be explained in subsection 4.2.2, the lateral energy loss of each lead glass is not negligible, and for this reason all the seven lead glasses will be considered as a single calorimeter during the entire data analysis. Figure 3.16(a) shows the calorimeters on the beamline, while figure 3.16(b) their geometry.

3.2.7 The DAQ system

The Data AcQuisition procedure during the beamtest is the following (figure 3.17):

- the S1 and S2 signals are discriminated by a NIM (Nuclear Instrumentation Module) discriminator and, together with the SPS spill signal, are sent to a custom VME trigger board to generate the trigger;

- the trigger signal is sent to the "master" VME Readout Board (VRB) (connected to the first telescope), that generates the busy signal. The busy acts as a trigger for the other "slave" VRB, connected to the second telescope;

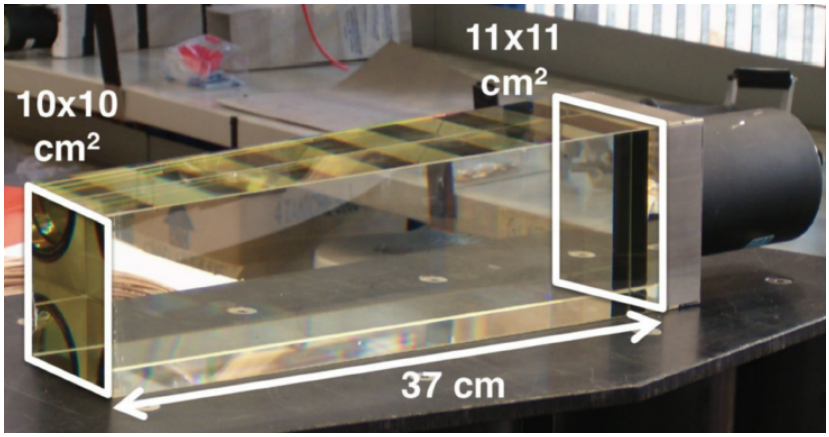

Figure 3.15: Single OPAL scintillating-Cherenkov lead glass block with its dimensions.

- The VRBs generate a hold signal that stores the telescope strip analog information;
- The VRBs work in zero suppression: each channel pedestal is subtracted from the stored analog information and the result is compared with a threshold defined on the basis of the channel rms noise. Only the channels above the threshold are stored in dedicated RAMs (Random Access Memories) and saved in data files in the interspill period;
- the busy signal is used by the digitizer to save the SiPMs and calorimeters waveforms in dedicated arrays that are read on an event by event basis. During the beamtest two 14 bit 8-channel digitizers were used. The one that digitized the SiPMs signals was the CAEN DT5730 which had a 500 MHz sampling rate [83], while the CAEN V1724 featured a 100 MHz sampling frequency [84] and digitized the calorimeters signals. The Data AcQuisition software performs a fast analysis on the digitizer data, computing the maximum amplitude of the waveform and the time with respect to the trigger at which such maximum is reached;
- during the interspill period, data are saved in HBOOK n-tuples;
- an online procedure selects events with a single track in the tracking detectors, reconstructing the cluster, that is the group of strips in which the crossing particle has deposited energy. The hit position is computed using a Center Of Gravity (COG) method [85]. The selected events are written in ASCII files, in which each row corresponds to a single

(a)

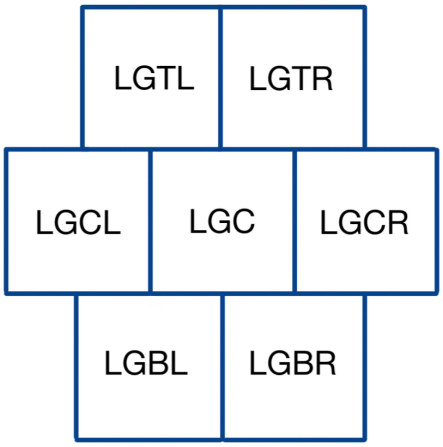

(b)

Figure 3.16: (a) Photo of the lead glass calorimeter block on the beamline during the *STORM* beamtest. (b) The lead glass block front side geometry. The labels correspond to the acronyms used in the data analysis.

event while the columns correspond to different physical information, as presented in table 3.7. A second online procedure merges all the ASCII data corresponding to a single run into a HDF5 (Hierarchical Data Format 5) file [86].

Table 3.7: Description of the columns saved in the ASCII files.

Name	**N° of columns**	**Description**
Nevent	1	Event number
Nstrip	4	Total number of cluster strips, for each microstrip silicon detector side
Nclu	4	Number of clusters for each microstrip silicon detector side
Xpos	4	Impact positions in the x and y directions for each microstrip silicon detector side
Gonio	4	Positions of the goniometer along its four degrees of freedom: two rotational ones and two translational ones
DigiBase	16	Baselines of each channel of the two digitizers
DigiPh	16	PH of the channels of both digitizers
DigiTime	16	Times of the channels of both digitizers

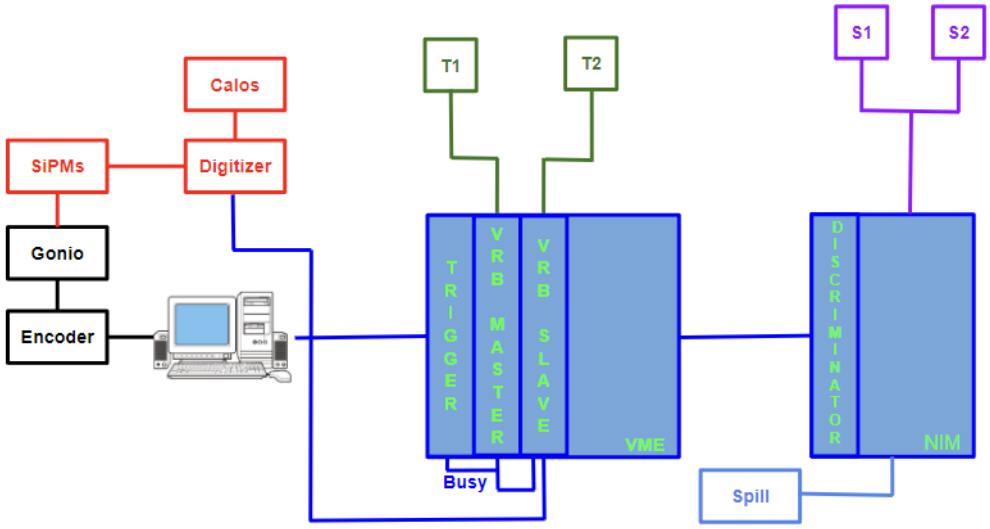

Figure 3.17: Data acquisition scheme.

Chapter 4

Preliminary measurements and analysis

The study of the behavior of the PWO samples requires a few preliminary steps in the analysis[1], to characterize both the beam and the setup. This chapter will focus on the beam features (angular divergence and dimensions) and on the calorimeter performance. The chapter will describe in detail the offline alignment procedure of the tracking detectors (which is fundamental to understand where and with which angle the particle impinges on the crystal), and the evaluation of the beam purity, which will be investigated combining the information coming from all the detectors present on the beamline.

4.1 Beam divergence and telescopes alignment

The two telescopes, placed at different positions along the beamline, acquired the particle hit position in the plane orthogonal ($x-y$ plane) to the beam direction (z). Combining the spatial information of both telescopes, the beam angular opening (θ_i), sketched in figure 4.1, is computed event by event:

$$\theta_i = \arctan\left(\frac{\Delta_i}{D_{Tele}}\right) \tag{4.1}$$

where $i = x, y$ are the directions orthogonal to the beam, Δ_i denotes the difference between the i-position acquired by the second telescope and the one

[1]The data analysis has been performed using Python3 packages such as numpy [87], matplotlib [88] and scipy.optimize [89].

acquired by the first telescope, and $D_{Tele} = 15.9\,\text{m}$ is the distance between the silicon modules.

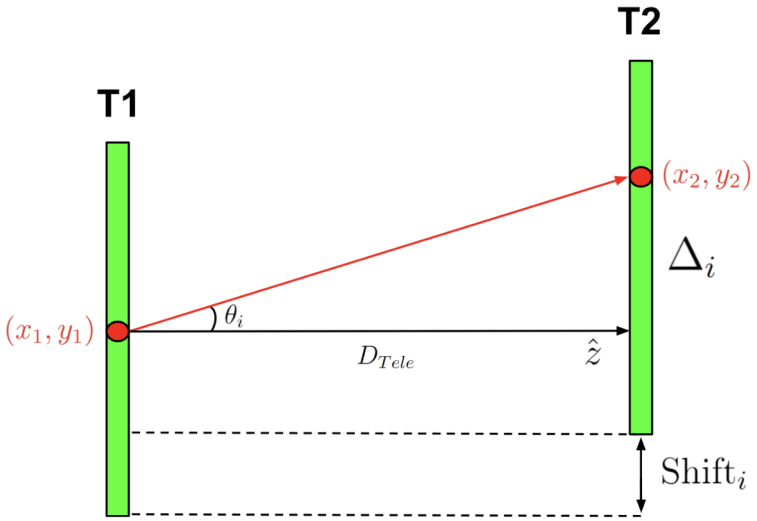

Figure 4.1: Schematic representation of the θ_i $(i = x, y)$ angular opening: the red arrow indicates the particle trajectory, the red circles highlight the impact points on the two telescopes (T1 and T2), D_{tele} the distance between them in the z direction while (x, y) the positions acquired by the telescopes. In the scheme the spatial shift of T1 and T2 along the i direction is also present, due to a not perfect alignment of the two telescopes in the $x - y$ plane.

The θ_i distributions are then fitted with unnormalized Gaussians for both $i = x, y$. The standard deviations of the curves (σ_x and σ_y), obtained in the Gaussian fit procedure, allow to measure the angular divergence of the beam, in both the x and y directions.

Figure 4.2 presents the θ_x and θ_y distributions for a 120 GeV electron beam, with the Gaussian fits superimposed.
The θ_x distribution features an asymmetric shape, probably due to the collimators settings.

Moreover, as illustrated in figure 4.2, the angular distributions are not centered at the origin. This is due to a not perfect alignment of the silicon detectors along the x and y directions (figure 4.1), thus requiring an offline alignment procedure.

The offline alignment is performed by subtracting the mean value of the Gaussian fit $(\mu_i, i = x, y)$ from the angular distribution (θ_i), as shown in

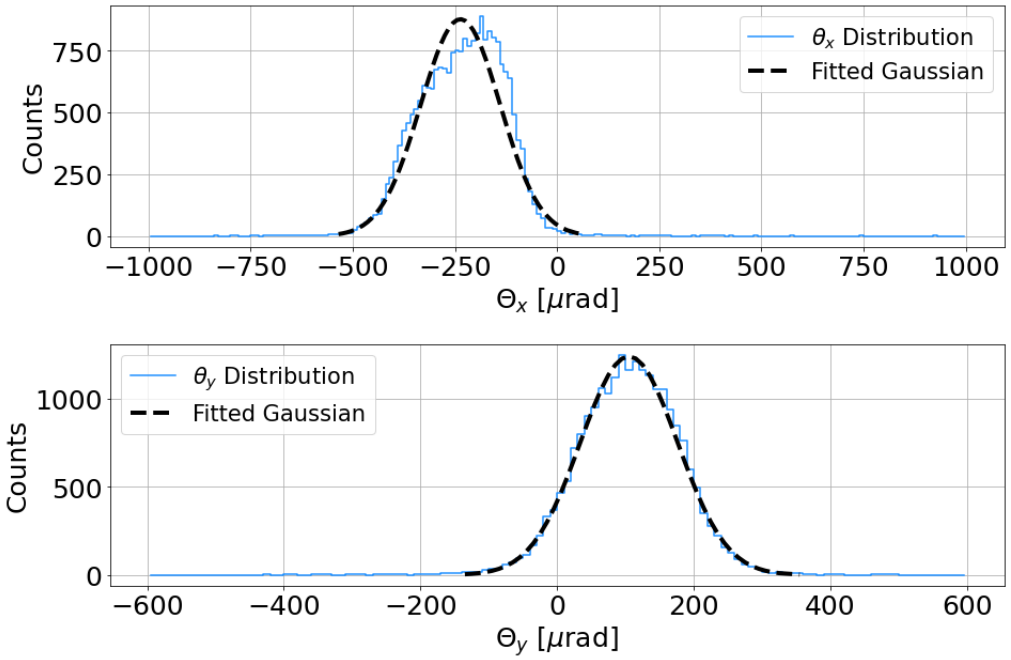

Figure 4.2: Angular distributions acquired with a 120 GeV electron beam with the Gaussian fits superimposed. θ_x and θ_y are not centered at 0, thus highlighting the misalignment between the two telescopes in the $x - y$ plane.

figure 4.3. Once the angular offset μ_i is obtained, it can be converted into a spatial offset (inverting equation 4.1), thus centering the spatial distributions of the impact points along x and y, as shown in figure 4.4.

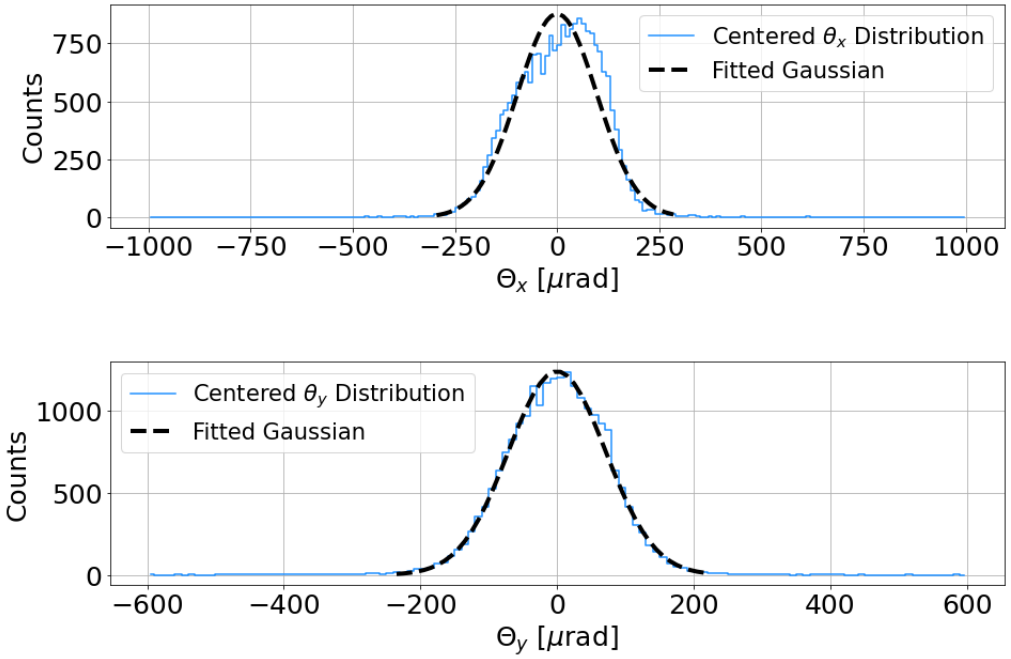

Figure 4.3: Angular distributions acquired with a 120 GeV electron beam with their Gaussian fits, once the mean values of the fits in figure 4.2 have been subtracted.

Figure 4.5 shows the decreasing trend of the divergence as the energy increases; on average the beam was more collimated along the y direction.

The smallest divergences are obtained for the 120 GeV electron beam: $\sigma_x = 97.22\,\mu\text{rad} \pm 0.47\,\mu\text{rad}$, $\sigma_y = 71.19\,\mu\text{rad} \pm 0.35\,\mu\text{rad}$. These values are optimal to measure coherent effects in crystals, given their small angular acceptances of the order of ~ 1 mrad.

4.2 Calorimeter characterization

In this section, the equalization of the lead glasses and the calibration of the whole calorimeter will be described. Moreover, the lateral energy leakage of each lead glass block will be analyzed, thus justifying the decision to consider the set of 7 lead glasses as a single calorimeter. Finally, the energy resolution will be computed.

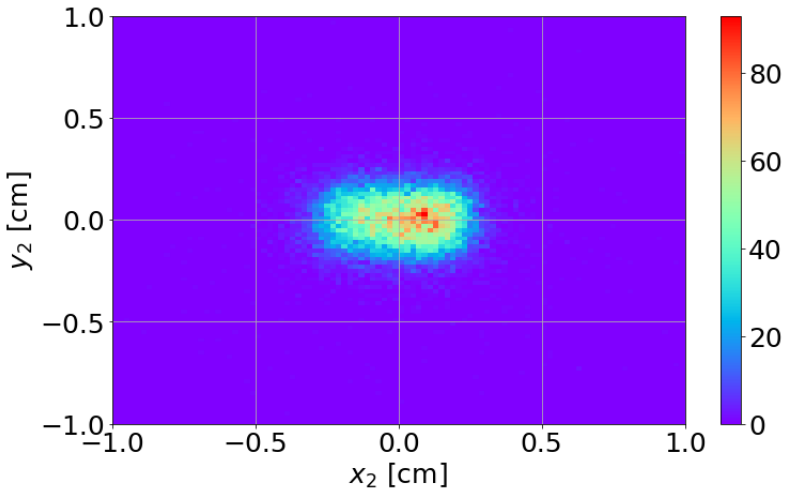

Figure 4.4: 2D histogram of the aligned hit positions on the T2 module, for a 120 GeV electron beam.

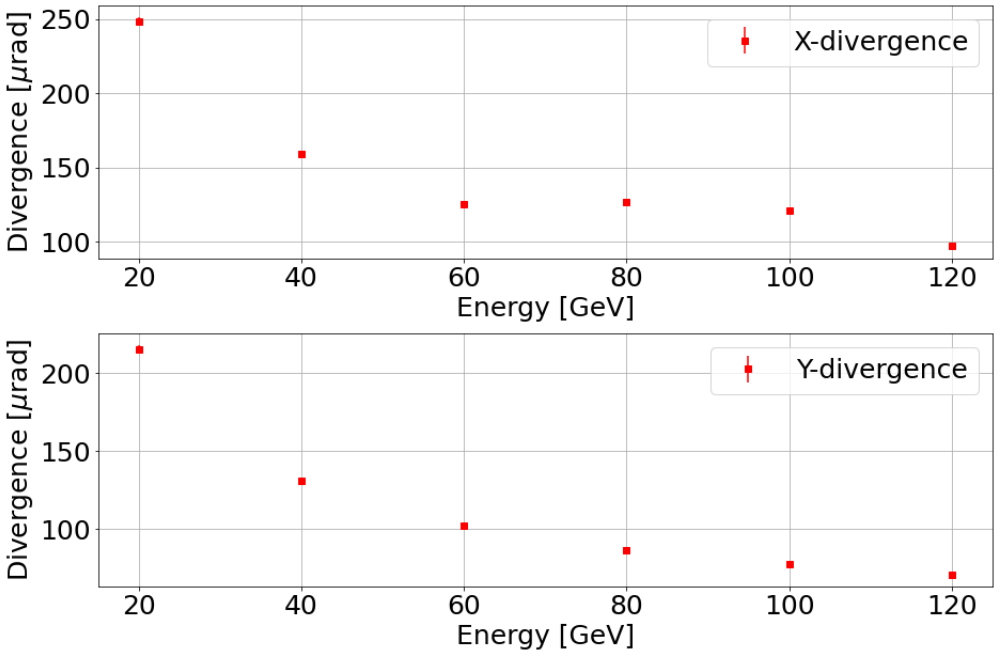

Figure 4.5: Angular divergence along the x and y directions as a function of the beam energy; as the energy increases, the beam divergence decreases.

4.2.1 Equalization and calibration

The calorimeter has to be calibrated in order to find the correspondence between the Pulse Height (PH, measured in a.u.) and the energy (measured in GeV) deposited by the incoming particles. At first, the calibration was performed calibrating separately each individual lead glass detector. However, it has been noted that the lateral spread in the shower development for the single lead glass was not negligible (details in subsection 4.2.2).

Due to the incomplete containment of the electromagnetic shower, it was not possible to directly calibrate each individual lead glass. Therefore, it was decided to calibrate the whole calorimeter, composed of 7 lead glasses, rather than the individual detectors. To do this, an equalization procedure of the lead glasses has first to be applied.
The procedure consists of the following steps:

1. an equalization run is considered for each lead glass, using a 60 GeV electron beam impinging directly onto the center of the lead glass itself. Each lead glass was positioned on the beam moving the Desy table on which the lead glasses were located.

2. Cuts in time (i.e. the peak time of the lead glass signal with respect to the time when the trigger was generated) and Pulse Height are performed to discard spurious triggers. As shown in figure 4.6, most of the events with a high PH populate a very narrow time interval (~ 20 ns). Only physical events, namely those crossing the trigger scintillators and the calorimeter, have the same arrival time. Low energy out-of-time events are caused by spurious triggers due to noise or to the particles that have crossed the trigger but not the calorimeter. On the other hand, high energy out-of-time events could be due to multiple particles in which the one that crosses the lead glass is not the one that has triggered the event.

3. The Pulse Height distributions of the selected events are fitted with unnormalized Gaussians, as shown in figure 4.7(a). From these curves the mean values μ_j are extracted, where the j label denotes the considered lead glass (j = LGC, LGCL, etc.).

4. The equalization factor is given by:

$$\mathrm{eq}_j = \frac{\mu_j}{\mu_{\mathrm{LGC}}} \tag{4.2}$$

where μ_j is the mean value extracted from the Gaussian fit of the j-th lead glass spectrum and μ_{LGC} is taken as a reference. Finally, the

equalization is performed dividing event by event the Pulse Height of the j-th calorimeter by eq_j. Figure 4.7(b) shows the equalized energy spectra while in table 4.1 the computed equalization factors are listed.

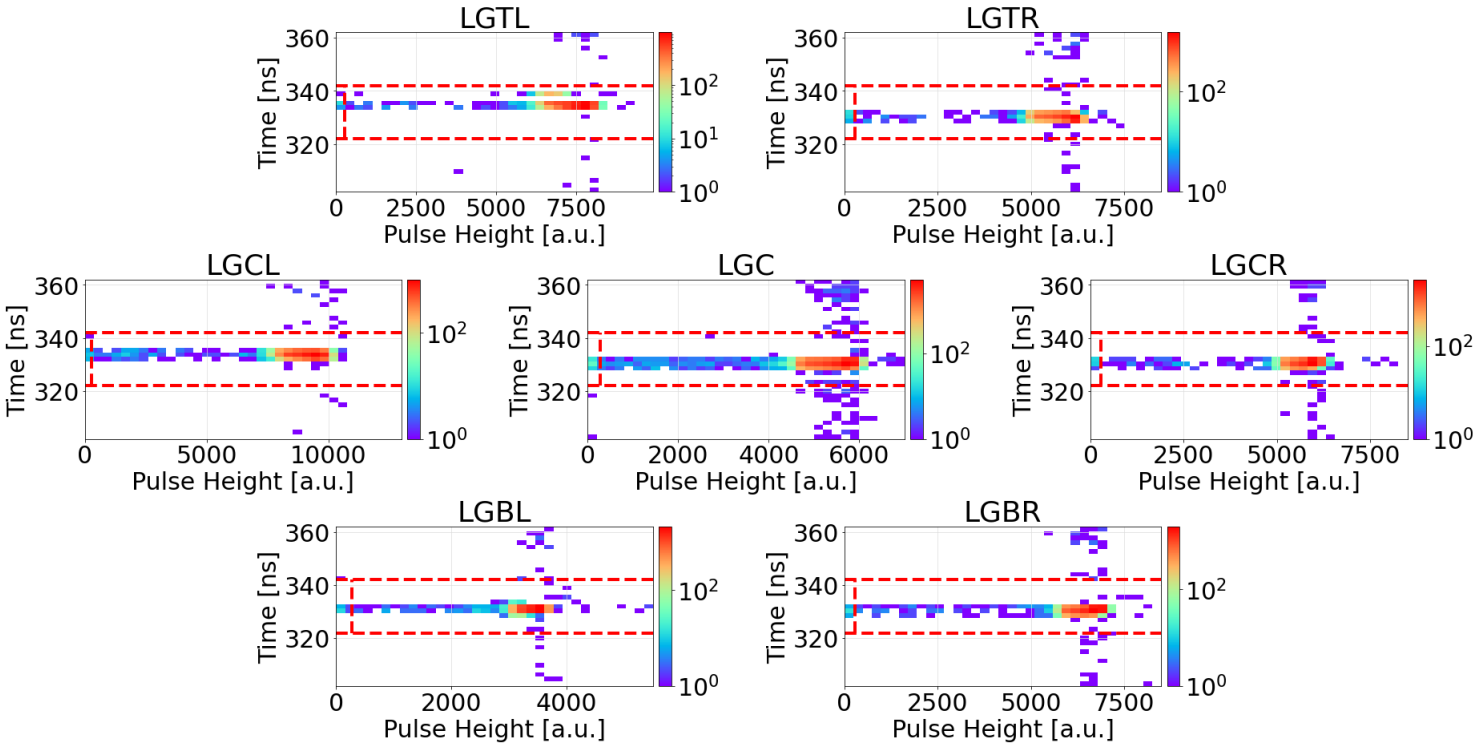

Figure 4.6: Correlation between the PH and the time of the lead glasses; the red dotted lines show the cuts in time and PH, performed to discard spurious triggers.

Once the equalization factors are computed, it is possible to calibrate the calorimeter. In order to do it, events coming from 6 calibration runs are considered: data were acquired with the electron beams centered with the LGC front face in the 20 GeV-120 GeV energy range, in steps of 20 GeV. The equalized PHs of each individual lead glass are then summed on a event by event basis, and the total spectrum is fitted with a Gaussian curve for every calibration run. The correspondence between the calorimeter energy values expressed in arbitrary units ($E_{a.u}$) and the beam energy expressed in GeV (E_{GeV}) is established performing a linear regression:

$$E_{a.u} = m \cdot E_{GeV} + q \tag{4.3}$$

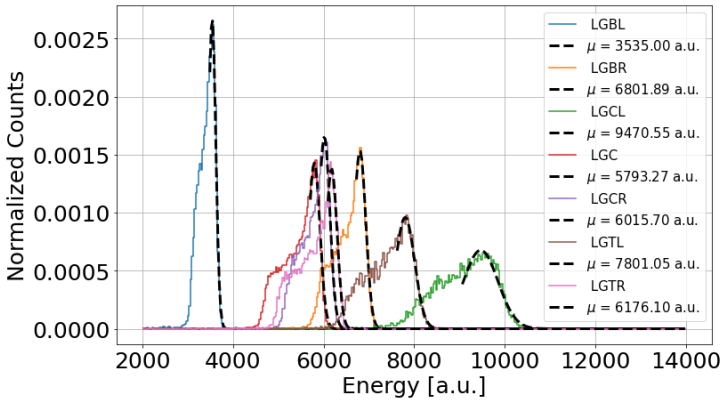

(a)

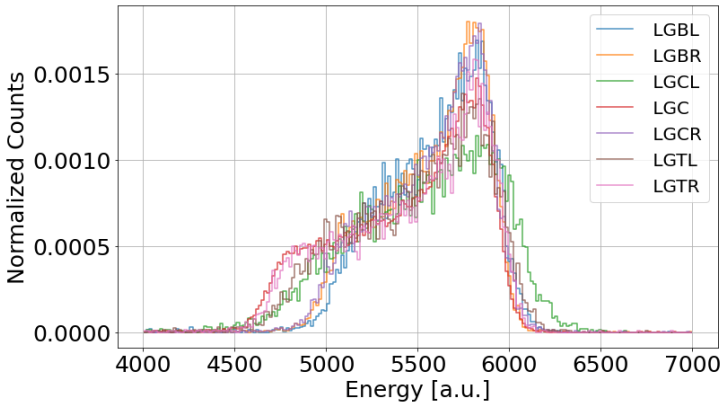

(b)

Figure 4.7: (a) Fitted energy spectrum of each lead glass for the 60 GeV equalization runs. The mean values extracted from the fitted Gaussians of each lead glass spectrum are listed on the plot. (b) Equalized spectrum of each lead glass. In both plots the energy distributions are normalized in order to have a unitary area.

Table 4.1: Equalization factors computed for each lead glass.

Lead Glass	Equalization factors
LGBL	0.61 ± 0.001
LGBR	1.17 ± 0.001
LGC	1 ± 0
LGCL	1.64 ± 0.002
LGCR	1.04 ± 0.001
LGTL	1.35 ± 0.002
LGTR	1.06 ± 0.003

Moreover, the percent residuals of the linear regression are computed as $\text{res}[\%] = 100 \cdot (y_{fit} - y_{exp})/y_{fit}$, where y_{fit} are the ordinates (in a.u.) predicted by the linear fit, and y_{exp} the ones measured by the calorimeter.

Figure 4.8 shows the linear regression with the extracted parameters and the residuals of the fit. The point at 20 GeV has a percent residual of $\sim 10\%$, and therefore it has been excluded from the fit.

4.2.2 Lateral energy leakage

The characteristic scale of the lateral spread of an electromagnetic shower is given by the Molière radius. As pointed out in section 2.1, 95% of the electromagnetic shower energy is contained within 2 R_M [37]. Since the transverse size of the lead glasses used during the beamtest was approximately $2R_M$, using the Molière radius value of the standard lead glass [82], one would expect a lateral energy leakage of $\sim 5\%$. However, this is not the case. To estimate the mean energy lateral spread, the following analysis has been performed:

- the data acquired using electron beams aligned with the center of LGC and with an energy in the 20 GeV-120 GeV range are selected;
- fiducial cuts are applied, as shown in figure 4.9(a), in order to select only the particles crossing the center of the lead glass front face. The fiducial area is 0.2×0.2 cm^2;
- the percentage lateral leakage (δE) is computed event by event, for each beam energy value, as follows:

$$\delta E = 100 \cdot PH_{lat}/PH_{tot} \tag{4.4}$$

  where PH_{lat} is the sum of the equalized Pulse Heights of the lateral lead glasses (the ones surrounding LGC), while PH_{tot} is the equalized Pulse Height of the whole calorimeter composed by 7 lead glasses;
- the δE distribution is fitted with a Gaussian for each energy, as shown in figure 4.9(b).

As shown in figure 4.10(a), the mean energy loss due to the finite transverse size of the calorimeter is always greater than 5%; the values of the points at 60 GeV and 120 GeV are almost twice the remaining values. This fact suggests that during these 2 runs the beam was not perfectly aligned with the LGC center. In fact, as it will be explained below, the Monte Carlo simulated data predict a constant lateral energy leakage even increasing energy, as

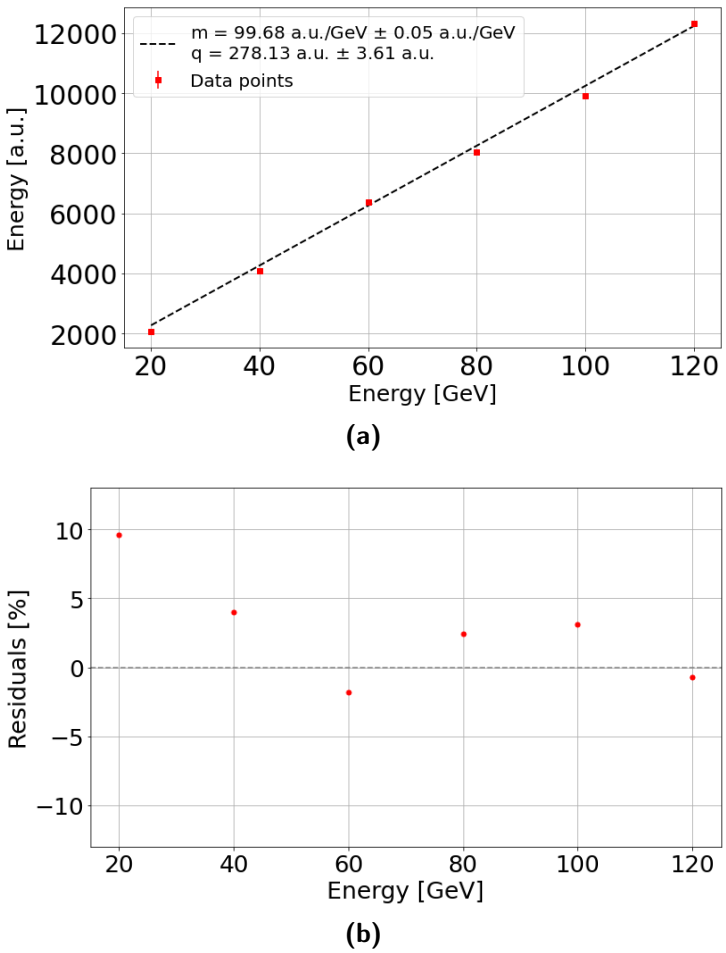

Figure 4.8: (a) Calorimeter calibration curve: the points are the experimental values while the dashed line is the fitted curve. The uncertainties on the data points are the Gaussian fitting errors and they are smaller than the points themselves. The parameters and their errors extracted from the fitting procedure are listed on the plot. (b) Percent residual scatter plot. The point at 20 GeV presents a residual value of $\sim 10\%$, and therefore it has been excluded from the fit.

expected. The hypothesis of a misalignment between the beam and the center of LGC is supported by the fact that the 60 GeV and the 120 GeV runs have been performed consequently in time and thus a misalignment issue may have affected both the sets of data. Moreover, the remaining 4 points of figure 4.10(a) feature on average a mean lateral energy leakage equal to 6.48%.

In order to compare the performances of the calorimeters used during the beamtest with standard lead glasses, the same procedure explained above has been performed with the simulated data. The Monte Carlo simulations have been performed using the Geant4 toolkit, reproducing the beam spatial and angular distributions, the experimental calorimeters geometry and the standard lead glass material (the main physical features of the standard lead glass can be found in [82, 90]). 12 simulations have been performed, using as beam files the electron beams with mean energies in the range 10 GeV-120 GeV[2].

Figure 4.10(b) shows the results: a standard lead glass presents on average a mean energy leakage of 3.89%, which is practically constant with the energy. The material used during the beamtest and the simulated one have different characteristics: the former features on average a mean energy leakage ~ 1.7 times larger than the latter. The discrepancy between the experimental and the simulated results could be due to the fact that the OPAL lead glass may have a larger Molière radius compared to the standard lead glass one [82]. A lateral energy loss of 6.5% is not negligible, and for this reason the OPAL lead glasses have been considered as a single calorimeter for the entire data analysis. This choice also prevents the loss of information on the energy deposit in case the center of LGC and the beam were not perfectly aligned with each other.

4.2.3 Energy resolution

The fundamental parameter for characterizing a calorimeter is the energy resolution, which represents the accuracy with which the energy of a particle can be measured. The percentage energy resolution is defined as:

$$R = 100 \cdot \frac{\sigma_E}{\overline{E}} \tag{4.5}$$

where σ_E is the standard deviation of the energy deposit distribution and $\overline{E}$ its mean value. Several factors influence the energy resolution of calorimeters, including the intrinsic properties of the detector materials, the design of the calorimeter and the readout electronics. The behavior of the

[2]The simulated beams feature a Gaussian energy spectrum, with a standard deviation equal to 2% of the mean value.

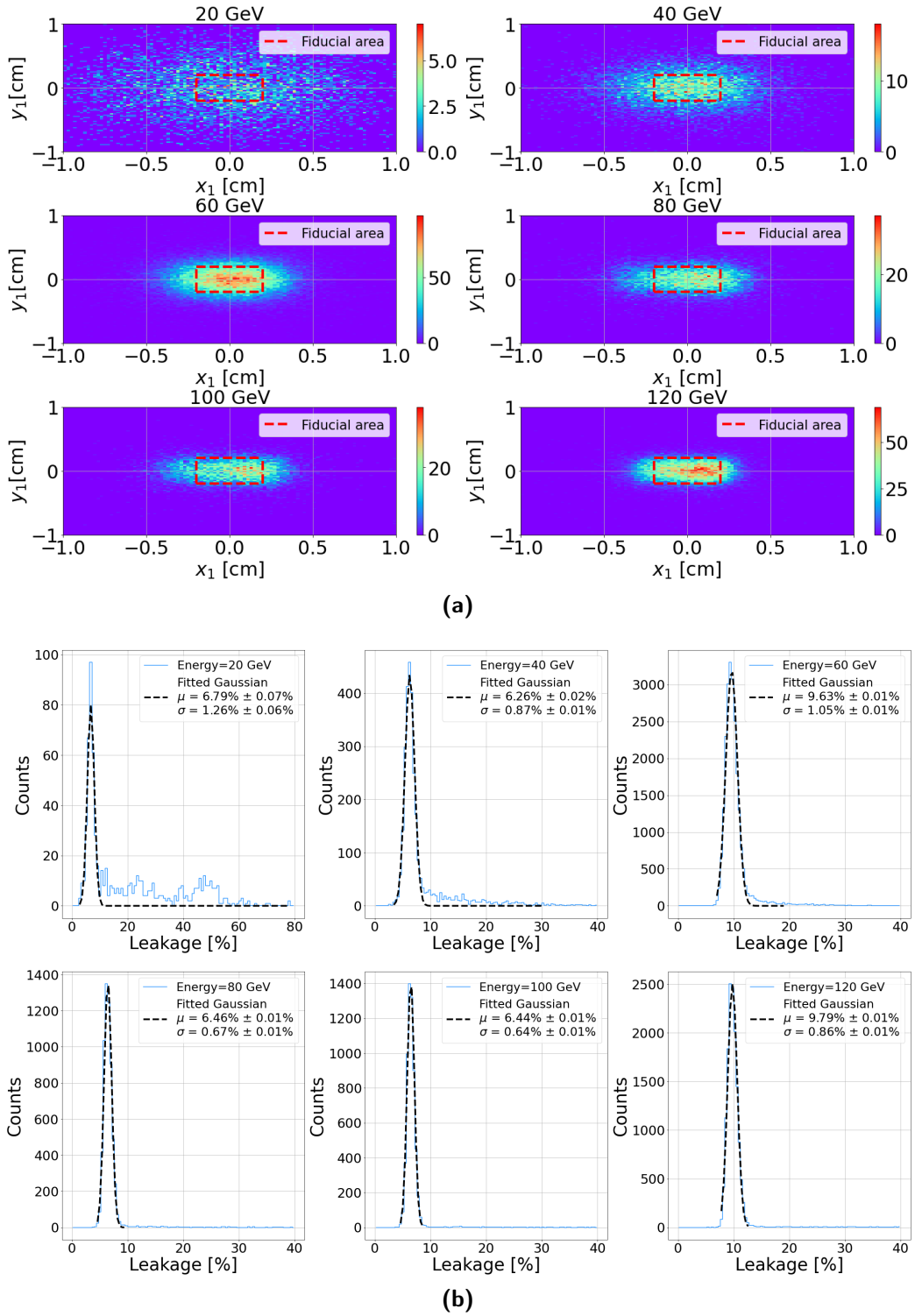

Figure 4.9: (a) Particle tracks on the calorimeter face for different energies: the red dotted squares are the fiducial cuts used to select the central area of the beam. (b) Lateral energy leakage distributions with the Gaussian fits. In the boxes the Gaussian fit parameters are listed.

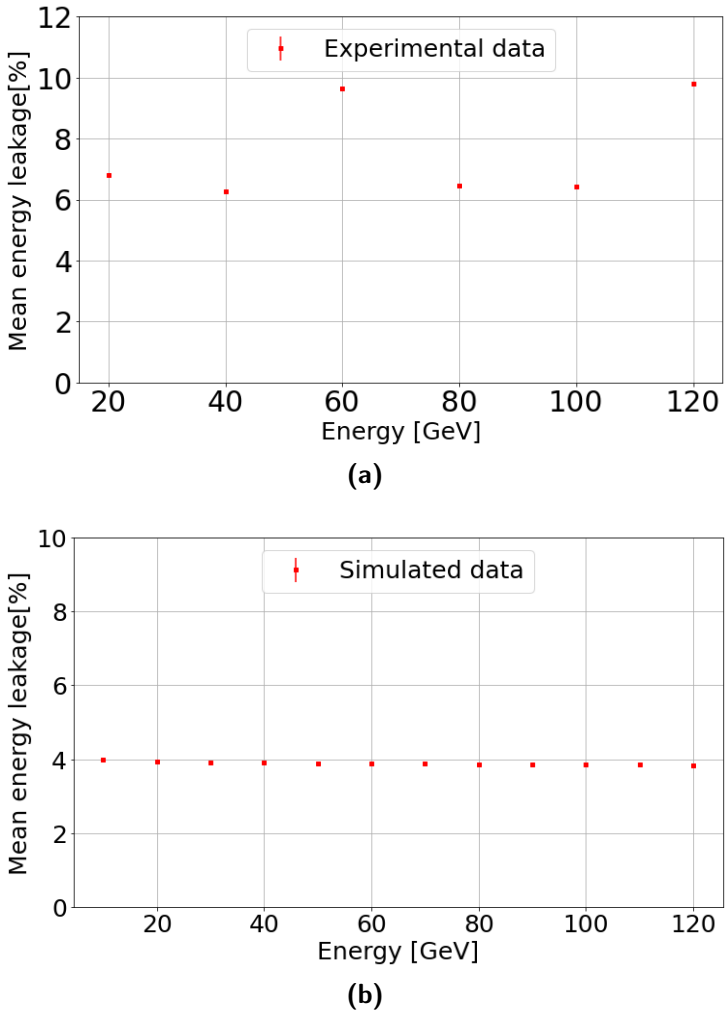

Figure 4.10: Mean lateral energy leakage of LGC as a function of the energy computed with (a) experimental data and (b) simulated data.

energy resolution as a function of the incident particle energy (E) can be modelled with the relation [37]

$$R(E) = 100 \cdot \frac{\sigma_E}{E} = \frac{a}{\sqrt{E}} \oplus \frac{b}{E} \oplus c \tag{4.6}$$

where a is the stochastic term due to fluctuations in the shower physical development, b is the noise term due to the electronic chain noise, c is the constant term which depends on the longitudinal and transverse energy leakage, the calorimeter mechanical imperfections and temperature gradients [37]. Using the 6 calibration runs, the energy resolution of the calorimeter is computed for different energies by means of equation 4.5. The values of σ_E and $\overline{E}$ are the ones extracted from the Gaussian fits of the whole calorimeter spectra, for each beam energy.

Figure 4.11 presents six experimental points, among which 5 have been fitted with equation 4.6; the 40 GeV point has been excluded because significantly off-scale. The parameters a, b and c have been obtained from the fitting procedure, resulting in the energy resolution function:

$$R(E) = \sqrt{\left(\frac{15.18\%\ \sqrt{\text{GeV}}}{\sqrt{E}}\right)^2 + \left(\frac{0.15\ \%\text{GeV}}{E}\right)^2 + 0^2} \tag{4.7}$$

The uncertainties on the parameters extracted from the fit are excessively high and with no physical meaning, since they exceed 100%. For this reason, they are not listed in equation 4.7. These uncertainties are justified by the limited degrees of freedom of the fitting procedure and by the broad energy spectra, shown in figure 4.7, which make the extrapolation of the values of σ_E and $\overline{E}$ highly dependent on the Gaussian fitting range.

Equation 4.7 features a stochastic term $a \sim 15\%$. It might seem quite high for a homogeneous electromagnetic calorimeter such as the OPAL one, which featured an overall energy resolution of $\sim 5\%/\sqrt{E(\text{GeV})}$ [37]. As already mentioned, the electron beam had a "low purity" in energy, thus presenting a very broad energy spectrum (figure 4.7). The energy fluctuations caused by the broad distribution of the energy deposit contribute to increase the stochastic term. On the other hand, the noise term is almost 0% thanks to the low noise readout chain of the calorimeter while the constant term of the whole calorimeter is null since the longitudinal and transverse energy fluctuations are negligible.

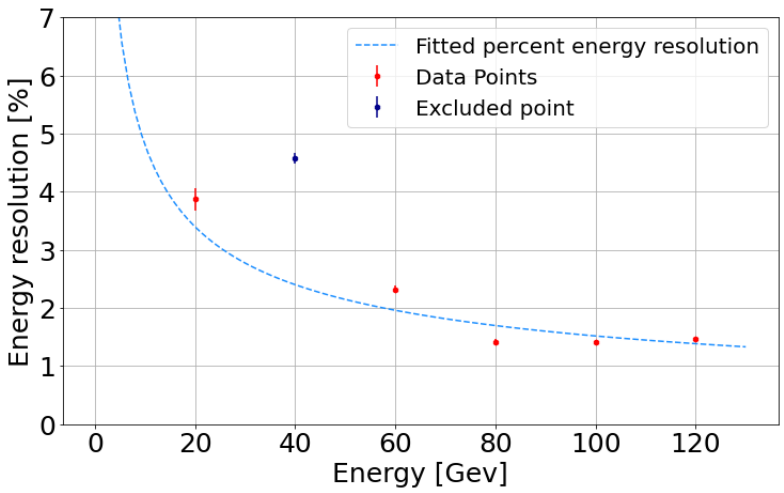

Figure 4.11: Energy resolution of the lead glass calorimeter: the red points are the experimental data used for the fit, the blue one is excluded from the fit and the dotted light-blue line is the fitted curve.

4.3 Beam purity

As previously mentioned, the electron beam was expected to be highly pure both in particle type and selected momentum. However, as shown in figure 4.7, the lead glasses energy spectra feature a broad distribution, thus highlighting a limited accuracy in the particle momentum selection. To investigate the type of particles which composed the beam, an analysis combining the information from all the detectors present on the beamline is performed: the PWO crystals and the lead glass calorimeter are used to identify the particles, while the tracking detectors to study the spatial distribution of the different components of the beam. The analysis is performed using the data acquired with a 120 GeV electron beam impinging centrally on the front face of one PWO crystal sample, readout by two SiPM matrices (Mat2 and Mat3). For this preliminary analysis only the Mat2 output is considered. Cuts in time have been applied to the SiPM output, in order to discard spurious triggers. To select the PWO central area, an efficiency map of the crystal sample is built. As shown in figure 4.12, the efficiency map reconstructs the entire beam profile, thus discarding the hypothesis that the beam hit the edge of the crystal. Figure 4.12 presents also the fiducial cuts applied to select only particles that crossed the center of the crystal front face; the fiducial area has a dimension of 0.2×0.2 cm^2.

The spectrum of such events in the calorimeter is shown in figure 4.13(a).

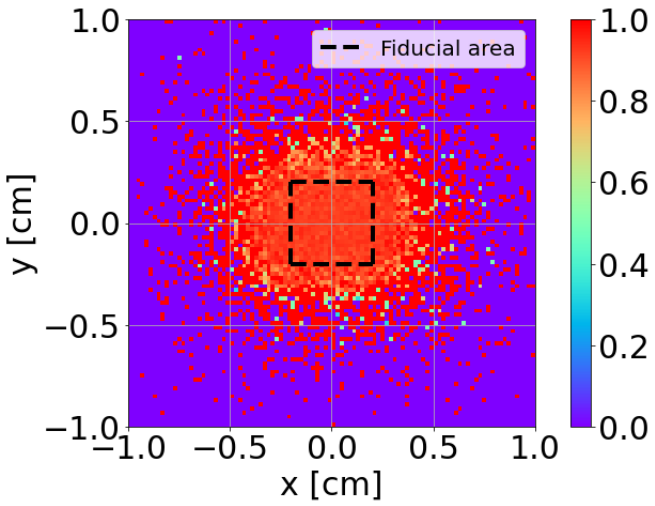

Figure 4.12: Efficiency map of the PWO crystal readout by Mat2. The black square represents the selected fiducial area.

Two different populations can be identified:

1. the first population (highlighted in cyan in figure 4.13(a)) deposited in the calorimeter energies in the 0-80 GeV range. The number of these events is several orders of magnitude smaller than the high energy peak ones; moreover they featured a very low signal in the SiPM output, as shown by the cyan curve of figure 4.13(b).

2. The second population of events (highlighted in green in figure 4.13(a)) deposited in the calorimeter energies greater than 80 GeV. The signal of these events in the crystal was significant, as shown by the green curve of figure 4.13(b).

The first population of events is due to a charged hadronic pollution, probably composed by negative charged pions. In fact, the pion interaction length (L_{int}) in PWO is $\sim 24\,\text{cm} \sim 27X_0$ (table 3.2). This means that the interaction scale length of the pions is 27 times larger than the electron one. The PWO crystal is $\sim 0.17\ L_{int}$ thick and thus pions crossing it deposited a negligible energy amount. On the other hand, the OPAL calorimeter is $24.7X_0 \sim 0.91\ L_{int}$ thick and so the hadronic particle can start a shower in such a distance, generating a significant energy deposit (up to 80 GeV). On the contrary, the second population of events is composed by electrons because they started an electromagnetic shower in the $4.6X_0$ PWO crystal and they populate the high energy peak of the calorimeter.

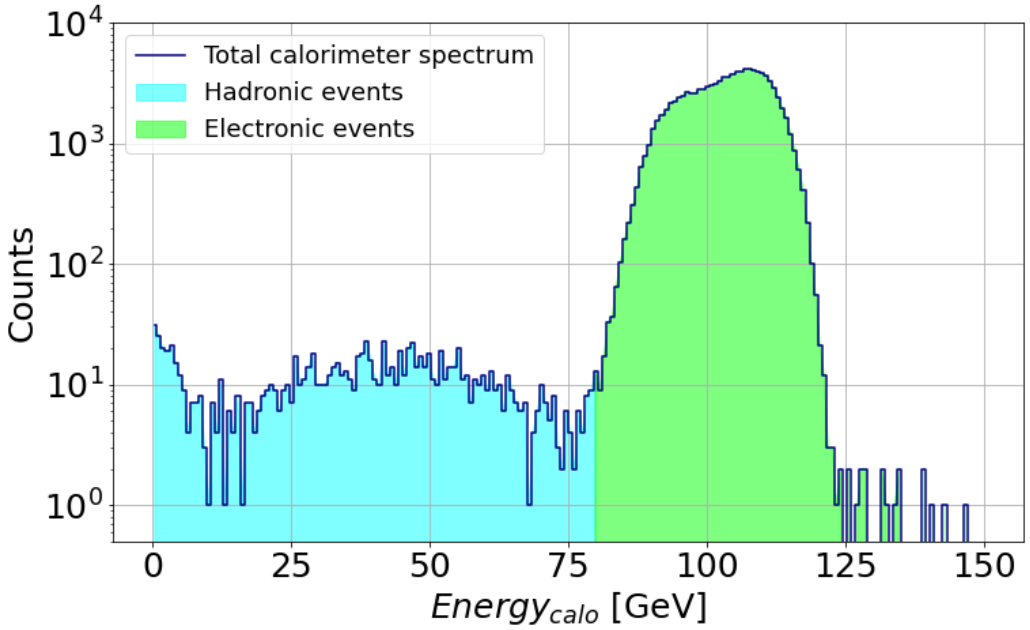

(a)

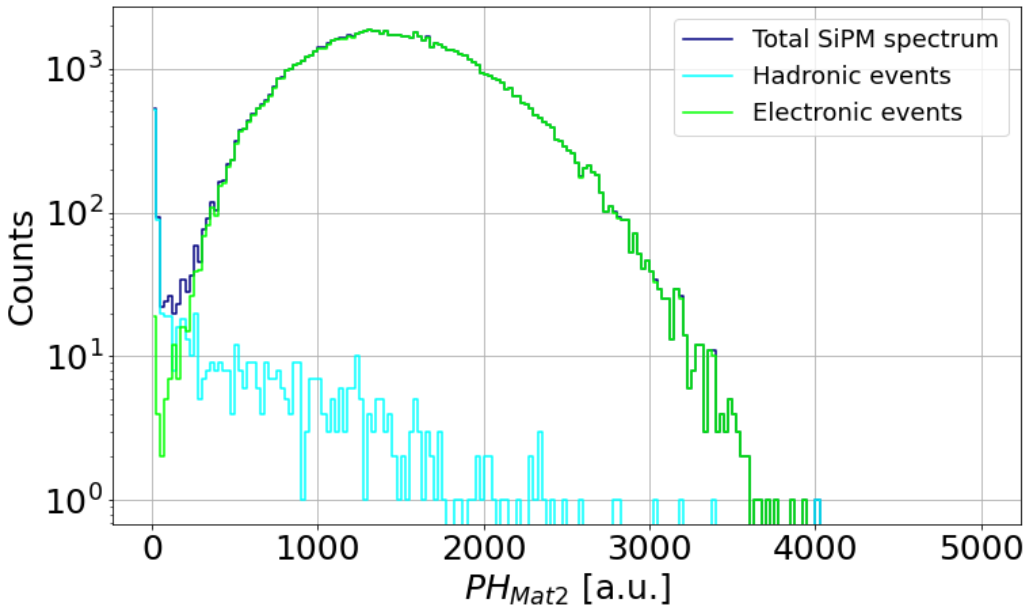

(b)

Figure 4.13: (a) Calorimeter spectrum with a 120 GeV run with the crystal on the beamline. The energy distribution is divided in two regions: the first energy range (0-80 GeV, cyan area) is due to the hadronic pollution while the second region (80-150 GeV, green area) is due to the electronic component of the beam. (b) SiPM spectrum for the different types of events selected in the calorimeter: the dark blue curve represents the total SiPM spectrum, the cyan one the events which deposit a smaller amount of energy in the calorimeter (0-80 GeV), and the green one the high-energy events of the calorimeter spectrum.

The hadronic percentage of the events is evaluated computing the fraction of the low energy events in the calorimeter spectrum (cyan area of figure 4.13(a)), with respect to the total ones: it results to be 3.05%. Moreover, the tracking detectors are used to investigate the hadrons spatial distribution: these events are uniformly distributed on all the beam area in the $x - y$ plane.

To confirm the hypothesis of the hadronic beam pollution and reproduce the broad electron energy distribution, a Monte Carlo simulation with the Geant4 toolkit has been developed. The simulated setup comprises also the PWO crystal on the beamline (figure 3.2). The beam energy input file has been defined as follows:

- 150000 events are generated with an energy distribution equal to the electron part of the 120 GeV calorimeter experimental spectrum[3];
- 3% of the total events are generated using a monoenergetic beam of 120 GeV negative pions.

Figure 4.14(a) presents the simulated and the experimental calorimeter spectra with the Gaussian fits of the high-energy peaks superimposed. In order to quantify the goodness of the simulation procedure, the Kullback-Leibler divergence is used, which is a statistical distance measuring the difference between a statistical distribution P taken as a reference, and another distribution Q. It is defined as follows [92]:

$$KL[P][Q] = \int_{-\infty}^{\infty} p(x) \log\left(\frac{p(x)}{q(x)}\right) dx \tag{4.8}$$

where $p(x)$ and $q(x)$ are the probability densities of $P(x)$ and $Q(x)$. In this case, the two distributions are Gaussian (N_{exp} and N_{sim}) and equation 4.8 becomes [92]

$$KL[N_{exp}][N_{sim}] = \sqrt{\frac{\pi}{2}} A_{exp}\sigma_{exp}\left[\log\left(\frac{A_{exp}^2}{A_{sim}^2}\right) + \frac{\sigma_{exp}^2}{\sigma_{sim}^2} + \frac{(\mu_{exp} - \mu_{sim})^2}{\sigma_{sim}^2} - 1\right] \tag{4.9}$$

where A_{exp}, σ_{exp} and μ_{exp} are the amplitude, the standard deviation and the mean value of the Gaussian high-energy peak of the experimental spectrum; A_{sim}, σ_{sim} and μ_{sim} are the ones of the simulated spectrum high-energy peak. As shown in equation 4.9, two Gaussian distributions have a null Kullback-Leibler divergence only if they are identical. On the contrary, the upper bound of KL is infinity. Thus, as the $KL[N_{exp}][N_{sim}]$ value

[3]Using the hist command of the Geant4 General Particle Source [91].

decreases, the agreement between the experimental and simulated energy distributions improves [92]. The divergence of the two Gaussian distributions of figure 4.14(a) is $KL[N_{exp}][N_{sim}] = 0.062$.

A similar procedure is followed also in the case of a 100 GeV electron beam impinging on the center of the PWO crystal face. The comparison between the experimental and the simulated calorimeter spectrum is presented in figure 4.14(b) and the relative statistical divergence is $KL[N_{exp}][N_{sim}] = 0.066$.

This section concludes the preliminary analysis of the performance of the downstream electromagnetic calorimeter and the spatial and energy features of the beam. In the next chapter, the behavior of the PWO crystal in the Strong Field regime will be studied, and the dependence of the energy deposit on the lattice-to-beam orientation will be analyzed in detail.

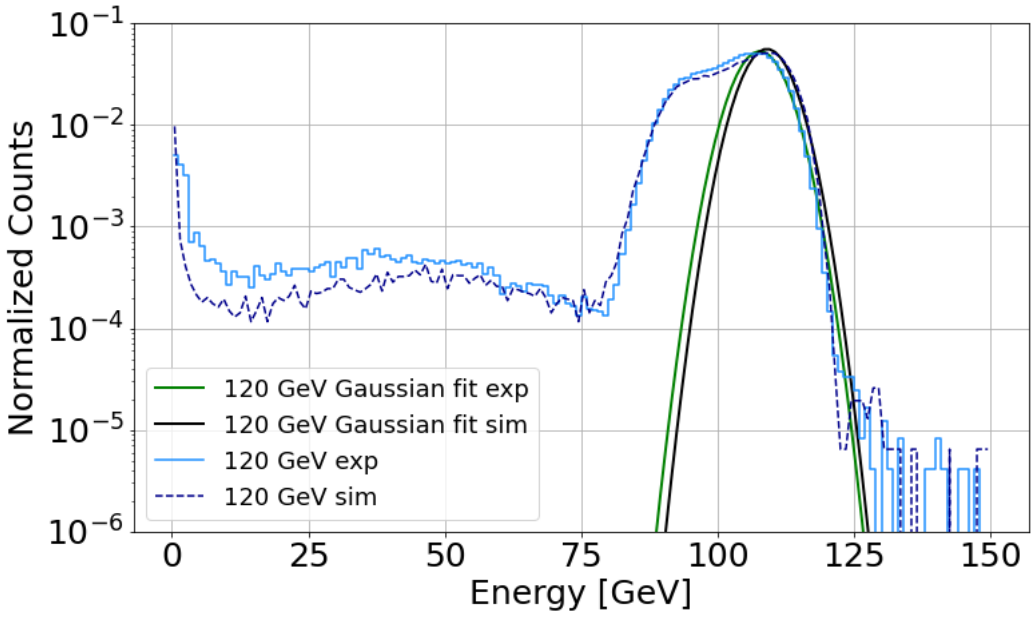

(a)

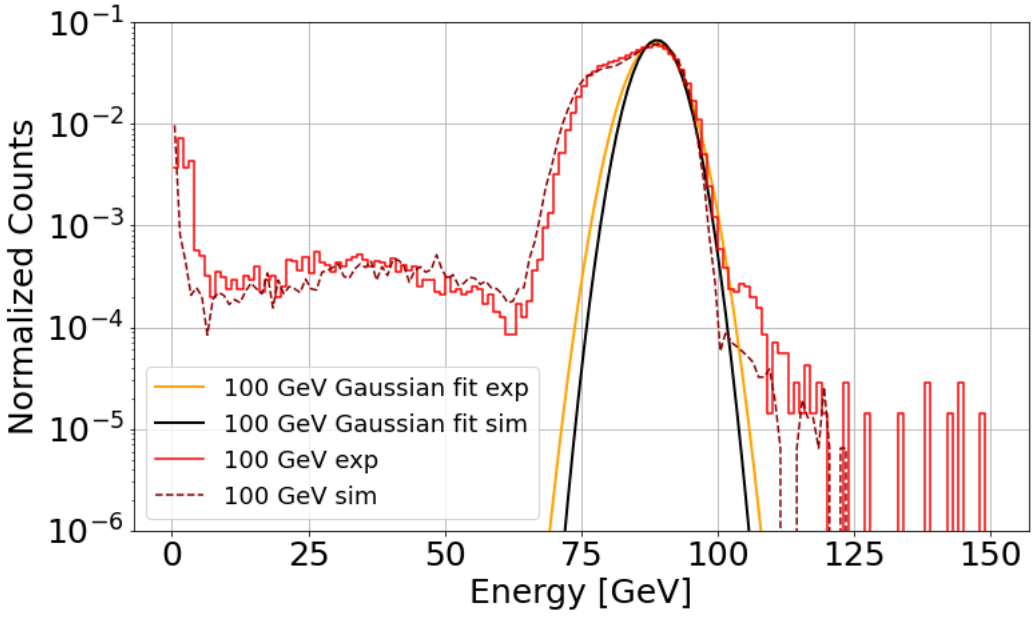

(b)

Figure 4.14: Experimental and simulated calorimeter spectrum with the Gaussian fits of the high-energy peaks superimposed, for a (a) 120 GeV run and (b) a 100 GeV run. Both spectra are normalized in order to have a unitary area.

Chapter 5

Data analysis and results

The ultimate goal of this thesis, and of the *STORM 2022* beamtest, is to characterize the light output response of the PWO crystal as a function of the lattice-to-beam alignment angle.

In order to investigate the energy deposit in the crystal sample and the acceleration of the electromagnetic shower in the Strong Field regime, when the sample is aligned with the electron beam, an efficient alignment procedure is needed. The first part of the chapter focuses on the alignment procedure, which is a multi-step process, including a manual procedure followed by a more accurate software alignment of the data. The study of the SiPMs response as a function of the particle impact angle, as it will be shown in the second part of the chapter, will help in characterizing the PWO lattice structure by revealing its crystalline planes.

In the last part of the chapter, the enhancement of the energy deposit in the crystal, due to the SF effects induced by the lattice-to-beam orientation, will be treated. A particular emphasis will be given to the reduction of the radiation length, occurring when the crystal axis (<100>) and the high energy beam are perfectly aligned between themselves.

5.1 The alignment procedure

Before characterizing the crystal behavior when oriented with the particle beam, it is necessary to align the electron beam with the crystal axis under study (<100>). The alignment starts in the experimental area with a manual pre-alignment procedure, which guarantees the crystal to be positioned aligned within few mrad with the beam (details in subsection 5.1.1).

The precise coordinates of the alignment angles will be computed by an off-line procedure, whose main task is to study the SiPMs response as a

function of the goniometer angle. The alignment is achieved building the so called stereogram (details in subsection 5.1.2), a 2D scatter plot representing the SiPMs PH as a function of both the rotation angles of the goniometer. In the end, investigating the energy deposited in the $PbWO_4$ as a function of the misalignment angles, the main lattice features, as the crystal planes, will be shown.

5.1.1 Pre-alignment

The pre-alignment of the crystals is performed exploiting the deflection of a laser beam off the crystal surface. If the sample is opaque, as in the case of the tested PWO, a small mirror is mounted on its surface, as shown in figure 5.1. However, the angular offset between the crystal and the mirror has to be computed. In order to do this, a preliminary study in the laboratory using the High-Resolution X-Ray Diffractometer (HRXRD) [5] is performed.

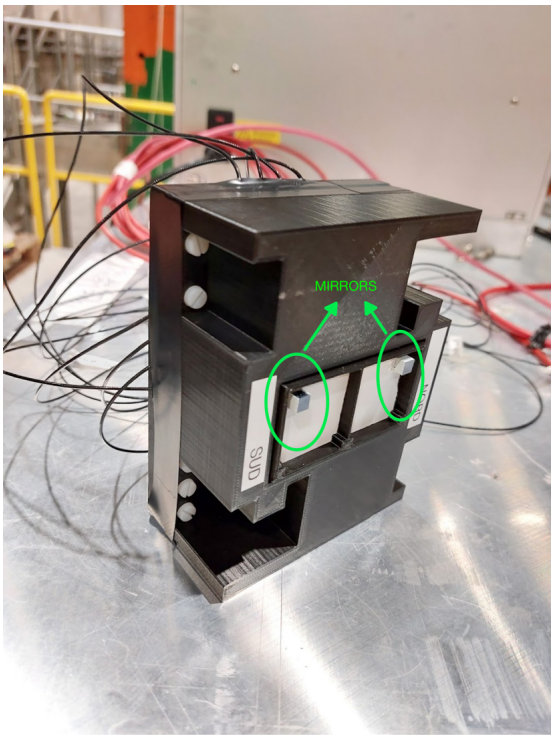

Figure 5.1: The plastic holder housing the $PbWO_4$ crystals: the mirrors are glued in the corners of their surfaces and highlighted in green.

Once the angular offset between the crystal and the mirror is computed, the pre-alignment takes place in the experimental area. The working scheme

of the procedure is represented in figure 5.2 and it consists of the following steps:

1. the plastic holder, housing the crystal samples, is placed on the goniometer;

2. a laser is located at the beginning of the beamline;

3. the laser is aligned with the z beam direction by means of a straight line drawn on the ground and two plummets;

4. a pentaprism is placed at the same height of the mirror, out of the beam trajectory. The pentaprism is a fundamental component, as it deflects the visible light by 90°, as indicated in figure 5.2. Thus, if the mirror mounted on the PWO crystal surface is not perfectly parallel to the z axis, the laser light is deflected off the initial direction, as shown in figure 5.2 (top). On the contrary, if the mirror is perfectly parallel to the beam direction, the laser light returns along the initial path, as shown in figure 5.2 (bottom);

5. the motorized system, which supports the plastic holder, rotates the goniometer by 90°, in order to place the mirror perpendicularly to the beam direction;

6. the sample is rotated by a small angle, corresponding to the angular offset between the crystal and the mirror, measured in the laboratory with the HRXRD.

This procedure allows to find the correct orientation with respect to the reference axis, with a precision of a few mrad. Since the Strong Field acceptance is of the order of ~ 1 mrad, a more precise alignment is needed. In the next section, the software alignment procedure, performed to determine the axis angular coordinates, will be described.

5.1.2 Software alignment: the stereogram

After the pre-alignment procedure, the light output of the $PbWO_4$ crystal samples has been studied as a function of the two remotely controlled angular degrees of freedom of the goniometer, with a 100 GeV electron beam. These angular degrees of freedom are defined as θ_{ang} and θ_{cradle}: the former represents the angular coordinate of the goniometer angular stage of figure 3.14(b), while the latter the angular coordinate of the cradle stage (details are provided in subsection 3.2.5).

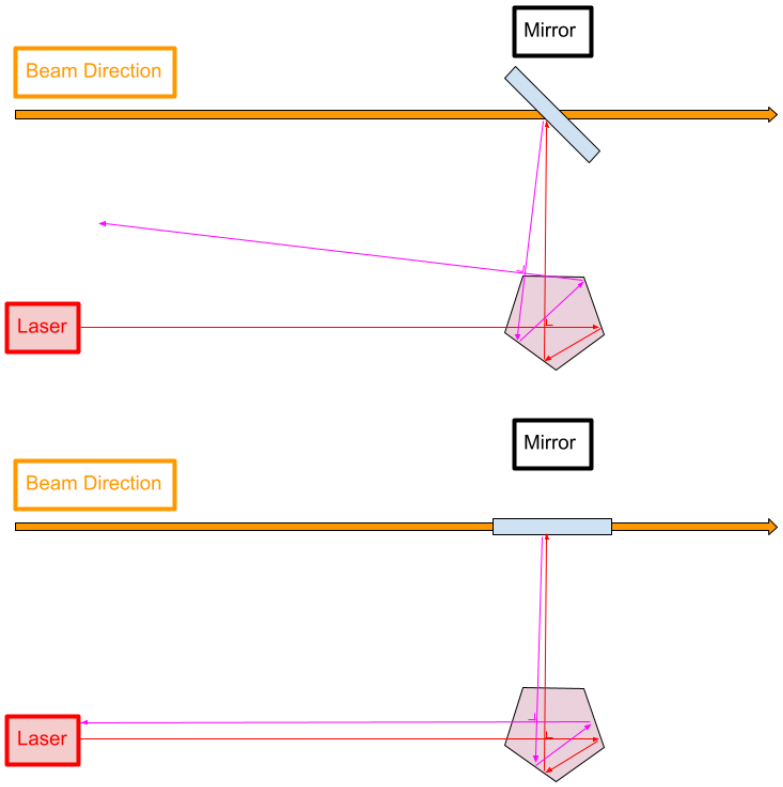

Figure 5.2: Schematic representation of the pre-alignment procedure: (top) the mirror is not parallel to the beam direction, thus the laser light is deflected off the initial laser direction; (bottom) the mirror is parallel to the beam direction, thus the laser light returns along the initial path.

This analysis allows to determine more precisely the alignment angles between the <100> axis and the particle beam direction. In fact, the maximum energy deposit in the crystal is expected when the reference axis and the particle beam are perfectly aligned with each other. In order to achieve such an alignment, several angular scans were performed starting from the pre-alignment angle values. During each angular scan, the goniometer moved along either θ_{ang}, keeping θ_{cradle} fixed, or along θ_{cradle}, keeping θ_{ang} fixed. To analyze the energy deposit as a function of the goniometer angle, the PH of the SiPM matrices which read out the light output of the crystal hit by the particle beam (Mat_2 and Mat_3 in this case) are equalized (details in subsection 5.2.1), and then summed on an event by event basis. The mean PH is computed for any couple of θ_{ang} and θ_{cradle} values and a first stereogram is built. As already mentioned, the stereogram consists in a 2D scatter plot, representing the SiPMs mean PH as a function of both the angles of the goniometer. The stereogram is represented in figure 5.3, and the alignment angles (θ_{ang}^{max} and θ_{cradle}^{max}), corresponding to the maximum mean energy deposit in the crystal, are listed in the box.

Figure 5.4 shows the mean energy deposit in two angular scans along the θ_{ang} and the θ_{cradle} directions, performed around the alignment angles: the mean energy deposit increases as the goniometer approaches the alignment condition.

The light output of the crystal sample is analyzed as a function of the misalignment angles, which are defined as follows:

$$\begin{cases} {\theta^{mis}}_x = \theta_{ang} - \theta_x \\ {\theta^{mis}}_y = \theta_{cradle} - \theta_y \end{cases} \tag{5.1}$$

where θ_x and θ_y are the angles with which the particle impinged on the crystal front face, along the x and y directions, respectively, computed with equation 4.1. Figure 5.5 shows the correlation between the mean PH measured by the two SiPM matrices and the θ_y^{mis} misalignment angle, in an angular scan on θ_{cradle}: the superimposed profile plot, which is computed as the mean value of y for each bin in x, shows a periodic structure and a multi-peaked shape. This trend of the profile plot suggests that the electrons crossed several crystalline planes along their path.

Finally, a second stereogram is built which consists in a 2D histogram of the θ_x^{mis} and θ_y^{mis} angles, weighted on the values of the equalized and summed Mat_2 and Mat_3 PHs. Each bidimensional bin represents an angular interval of the misalignment angles, while the corresponding color represents the mean value of the SiPMs PH, computed using all the events with the misalignment angles included in the aforementioned bin, and normalized at the maximum

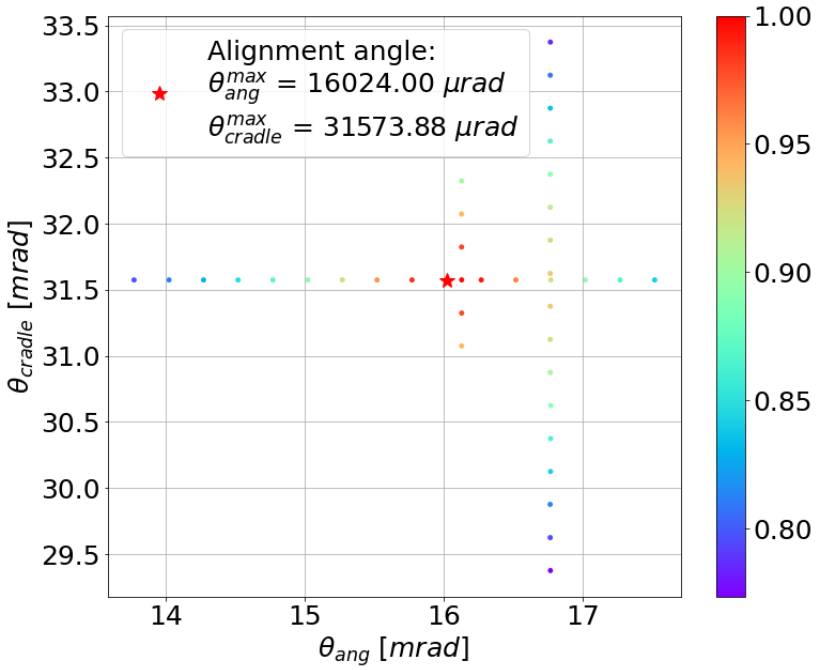

Figure 5.3: The stereogram; each colored dot represents the mean value of the PHs of Mat_2 and Mat_3 equalized and summed event by event, and normalized to the maximum value. The origin represents the angular coordinates obtained during the pre-alignment procedure.

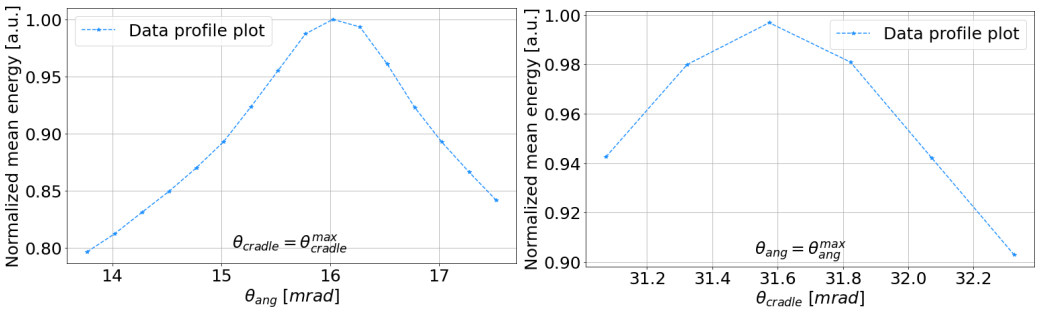

Figure 5.4: Mean values of the equalized and summed Mat_2 and Mat_3 PHs, normalized to the maximum mean PH value, during a scan along (a) θ_{ang}, keeping θ_{cradle} fixed at the alignment value, and (b) along θ_{cradle}, keeping θ_{ang} fixed at the alignment value.

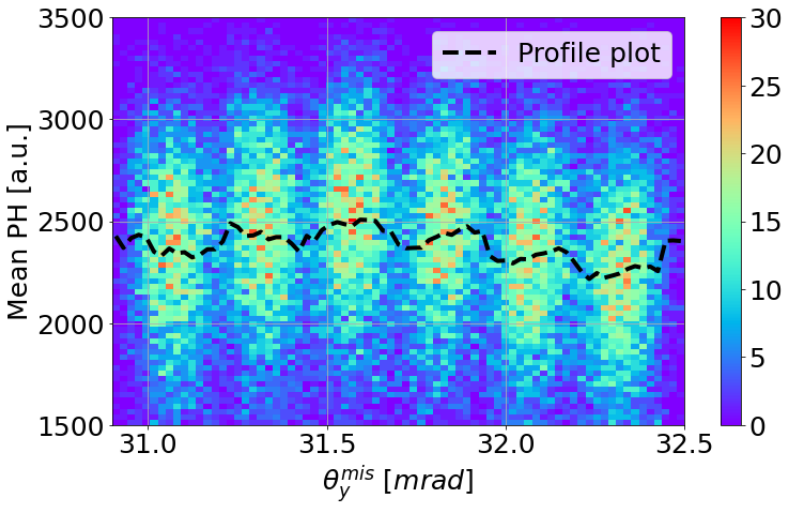

Figure 5.5: Correlation between the energy deposit in the PWO crystal sample and the θ_y^{mis} misalignment angle with the SiPMs profile plot superimposed: the periodic trend and the multi-peaked shape of the profile plot are probably due to the presence of several planes.

value.

The second stereogram is built with a broader set of angular scans with respect to the ones used for the first stereogram of figure 5.3 and it is shown in figure 5.6; the Cartesian axes origin coincides with the previously obtained alignment angles (θ_{ang}^{max} and θ_{cradle}^{max}).

Correlating both the misalignment angles with the SiPM Pulse Heights, it is possible to observe the skew planes of the lattice. The skew planes, as the name itself suggests, are not parallel nor orthogonal to any crystallographic direction, thus they appear oblique with respect to any other crystal plane or axis. These skew planes are indicated with dashed colored lines in figure 5.6 and they link the axis angular coordinates with the maximum points of the three angular scans along θ_x^{mis}, which are located in the bottom left corner of the figure. The SiPMs profile plots of these angular scans are shown in figure 5.7(a): the colored stars represent the maximum points of the energy deposited in the crystal, and the angular coordinates of each colored star are crossed by the color-associated skew plane of figure 5.6. The same procedure is performed for the calorimeter energy deposit: figure 5.7(b) shows that at the angular coordinates crossed by the skew planes, the energy deposited in the calorimeter reaches a relative minimum.

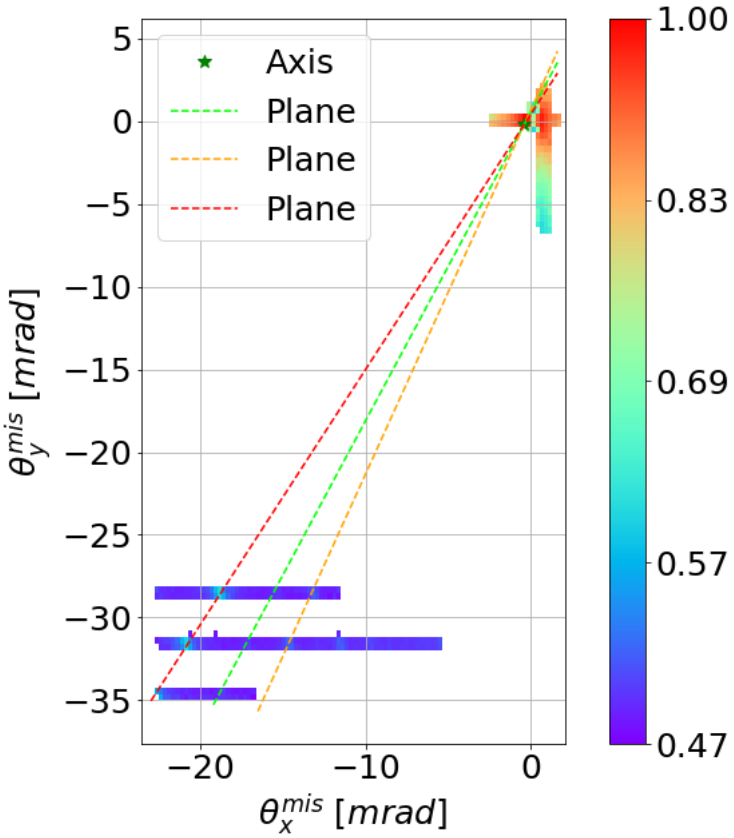

Figure 5.6: Crystallographic stereogram of the $PbWO_4$ sample: the x and y coordinates are the misalignment angles with the origin centered at $(\theta_{ang}^{max}, \theta_{cradle}^{max})$, and each bin color represents the mean PH of the SiPM matrices, computed using all the events populating the bin, and normalized to the maximum value. The green star represents the center of the bin corresponding to the maximum mean energy deposit (the axis coordinates), while the colored dashed lines indicate the skew planes.

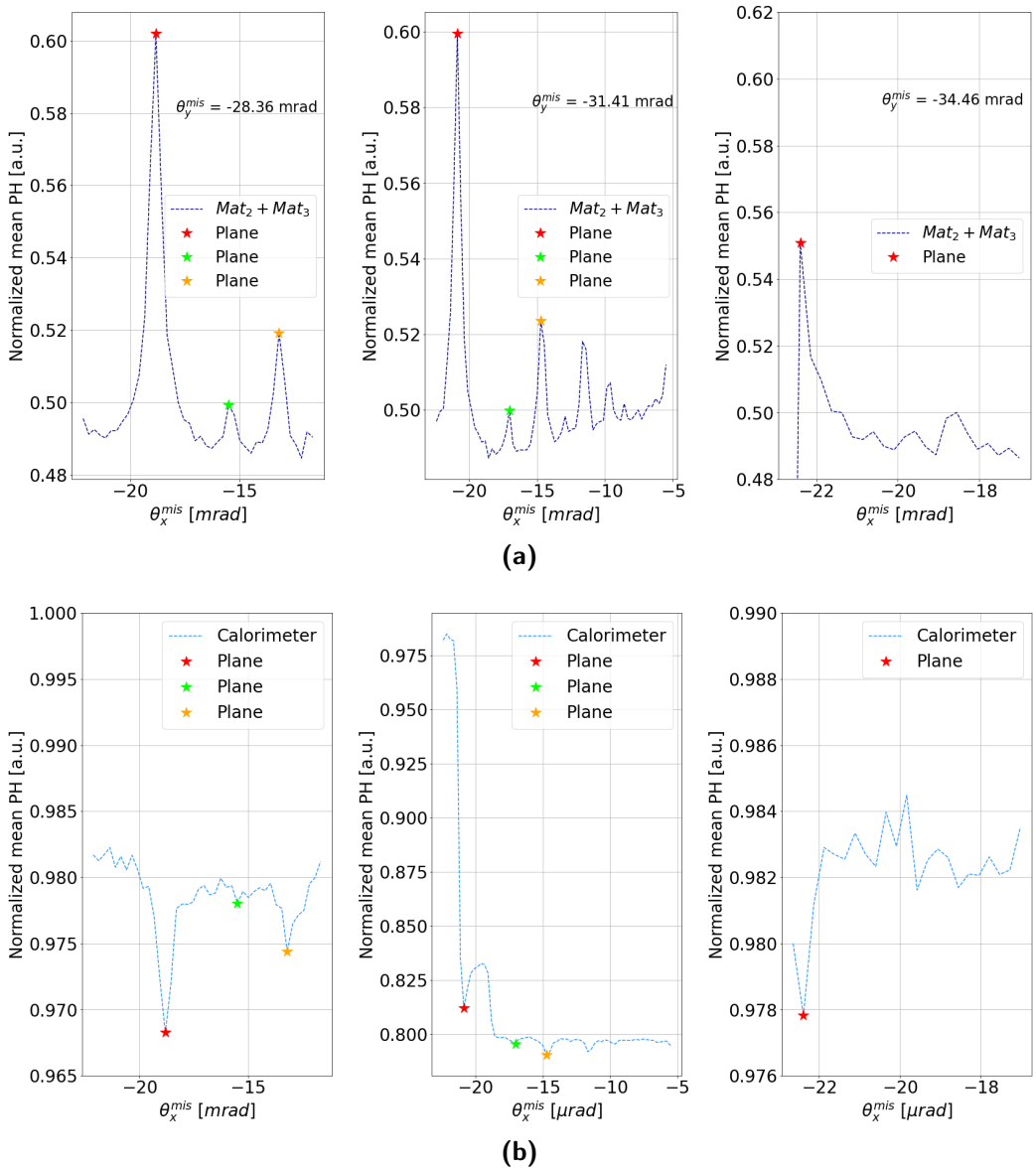

Figure 5.7: Profile plot of (a) the SiPM matrices and (b) the calorimeter, in a scan along the θ_x^{mis} angle; the fixed values of θ_y^{mis} are listed in (a). In both plots, the colored stars angular coordinates are crossed by the skew planes.

5.2 $PbWO_4$ characterization

After the alignment, dedicated high statistics runs were performed for the characterization of the PWO crystal, with 80-100-120 GeV electron beams. The PWO behavior is analyzed under the condition of axial alignment, as well as during the transition from the amorphous to the axial orientation. The main goal of this study, and of the entire thesis, is to estimate the energy deposit enhancement due to the Strong Field effects and to compute the reduction of the radiation length X_0 when the sample is oriented with the beam. During these long runs only a fraction of events has been analyzed. In order to fully characterize the PWO crystal, only particles crossing the center of the sample were selected, with a fiducial area of 0.2×0.2 cm^2, as already shown in figure 4.12. Moreover, since the very narrow angular acceptance of the SF effects, also cuts in divergence have been applied to discard all the events crossing the center of the PWO crystal with a too large angle. The fiducial interval used for the cuts in divergence is $[-125\,\mu\text{rad}, 125\,\mu\text{rad}]$; the divergence cuts are represented in figure 5.8.

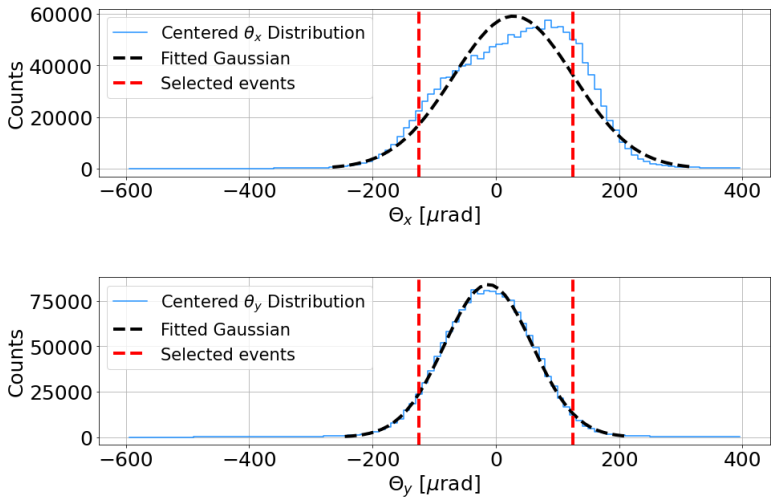

Figure 5.8: Angular distributions with their Gaussian fits superimposed (black dashed line) for a 120 GeV run, for (top) the x direction and (bottom) the y direction. In both plots the red interval indicates the selected divergence region.

5.2.1 Photodetector calibration

The energy deposited in the crystal sample under test, readout by the Mat_2 and Mat_3 matrices, is expressed in arbitrary units; in order to convert the information of the energy deposited in the sample in GeV units, a calibration procedure is needed.
Before calibrating, the equalization of the two SiPMs matrices Mat_2 and Mat_3 is performed using the data acquired with a 120 GeV electron beam. In order to equalize the two matrices, their energy spectra are fitted with a crystal ball-like function defined as follows [93]:

$$f(E; A, \overline{E}, \sigma, k_L, k_H) = A \cdot \begin{cases} \exp\left[\frac{k_L^2}{2} + k_L \frac{E-\overline{E}}{\sigma}\right] & \text{if } \frac{E-\overline{E}}{\sigma} < -k_L \\ \exp\left[-\frac{(E-\overline{E})^2}{2\sigma^2}\right] & \text{if } \frac{E-\overline{E}}{\sigma} \in [-k_L, k_H] \\ \exp\left[\frac{k_H^2}{2} - k_H \frac{E-\overline{E}}{\sigma}\right] & \text{if } \frac{E-\overline{E}}{\sigma} > k_H \end{cases} \tag{5.2}$$

where E is the function independent variable while A, $\overline{E}$, σ, k_L, k_H the function parameters. As shown in equation 5.2, the crystal ball function is essentially composed by a Gaussian core with two exponential tails, and it should correctly reproduce how the crystal energy spectrum is smeared due to an incomplete shower containment. The two SiPM matrices responses are equalized rescaling the Mat_3 PH, event by event, with the equalization factor $eq = \overline{E}_2/\overline{E}_3$, where $\overline{E}_2$ and $\overline{E}_3$ are the two Gaussian core mean values extracted from the crystal ball fit of the Mat_2 and Mat_3 spectra. The two photodetector spectra with their crystal ball fits are shown in figure 5.9, while the computed equalization factor is $eq = 1.10 \pm 0.002$.

In principle, it should be possible to calibrate the photodetectors starting from the missing energy of the calorimeter (that is, the lead glasses). In fact, in the case of a 120 GeV electron beam, the energy deposited in the PWO (E_{crys}), should satisfy the following relation:

$$E_{crys} = 120\,\text{GeV} - E_{calo} \tag{5.3}$$

where E_{calo} and E_{crys} are the energies deposited in the downstream calorimeter and in the crystal, expressed in GeV units. Figure 5.10 shows the correlation between the calorimeter energy deposit (expressed in GeV)

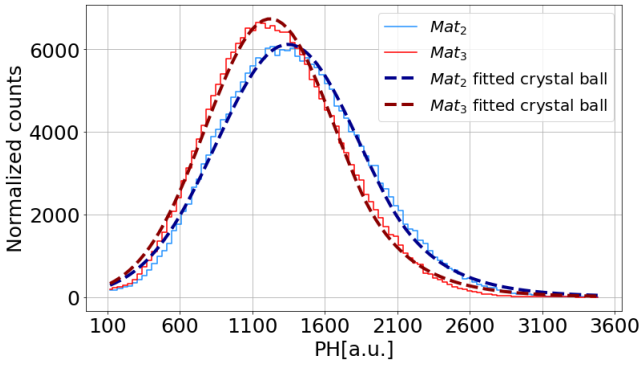

Figure 5.9: Energy spectra of the Mat_2 and Mat_3 SiPM matrices with their crystal ball fits superimposed. Both the spectra are normalized in order to have a unitary area.

and the equalized and summed PHs of the Mat_2 and Mat_3 matrices (PH_{crys}, expressed in a.u.). As equation 5.3 predicts, the energy deposited in the SiPM matrices and in the calorimeter are anticorrelated and the calorimeter end point is located at $\sim 120\,\text{GeV}$. Thus, knowing the energy measured by the calorimeter (E_{calo}), it should be possible to find the correspondence between the energy deposited in the crystal expressed in GeV ($120\,\text{GeV} - E_{calo}$) and the one expressed in a.u. (PH_{crys}), and thus calibrate the SiPMs.

However, this calibration procedure does not take into account the broad shape of the beam energy spectra already discussed, which leads to the extended shape along the y axis of figure 5.10, thus making very difficult to establish the PH_{crys} value for any fixed E_{calo}. Moreover, this calibration procedure does not take into account the energy losses due to the limited angular acceptance of the downstream calorimeter, and to the particles escaping from the lateral crystal surfaces. Thus, it has been decided to calibrate the SiPMs using a simulation based approach.

The experimental data used to calibrate the SiPMs were acquired using 80-100-120 GeV electron beams, with the crystal sample placed on the beamline in random orientation. The Monte Carlo simulations, obtained using the G4 toolkit, reproduced the spatial and the energy features of the experimental beams, as well as the experimental setup. Both the experimental and the simulated crystal energy spectra are fitted with a crystal ball function; the simulated spectra and their fits are shown in figure 5.11. The extracted mean values of the crystal ball Gaussian cores are used to perform a linear regression between the experimental and simulated data, thus establishing a correspondence between arbitrary units and GeV.

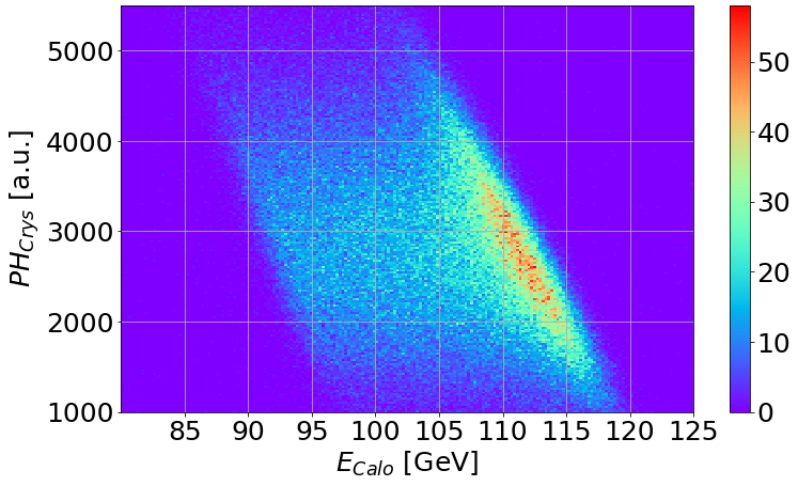

Figure 5.10: Anticorrelation plot between the energy deposited in the calorimeter (expressed in GeV) and the energy deposited in the crystal sample (expressed in arbitrary units).

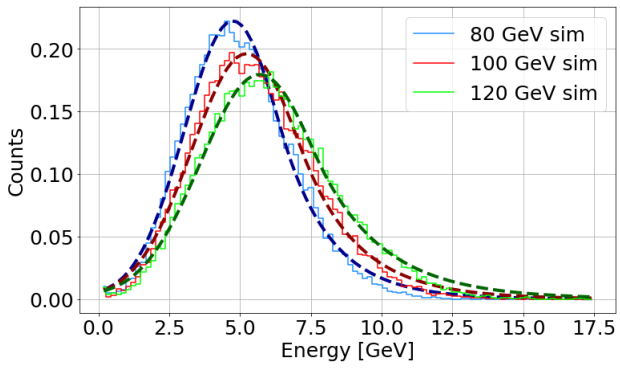

Figure 5.11: Energy spectra of the simulated energy deposit in the PWO crystal for three different beam energies. All the spectra are normalized in order to have a unitary area.

Two calibration lines are presented and compared: the first one (figure 5.12(a)) has been obtained using only the Mat_2 PH, while the second one (figure 5.12(b)) using the Mat_2 and Mat_3 PHs, equalized and summed event by event. The Mat_2 calibration line has a reduced chi square[1] $\overline{\chi^2} = 25.2$, while the calibration line computed using both the photodetector PHs has a reduced chi square $\overline{\chi^2} = 0.83$; the better fit procedure is thus the one obtained exploiting both the matrices output. Moreover, also performing the calibration using only the Mat_3 output, the reduced chi square ($\overline{\chi^2} = 4.03$) is higher than the one computed with both the matrices. This may be due to the fact that using both the matrices a larger fraction of the produced light is collected.

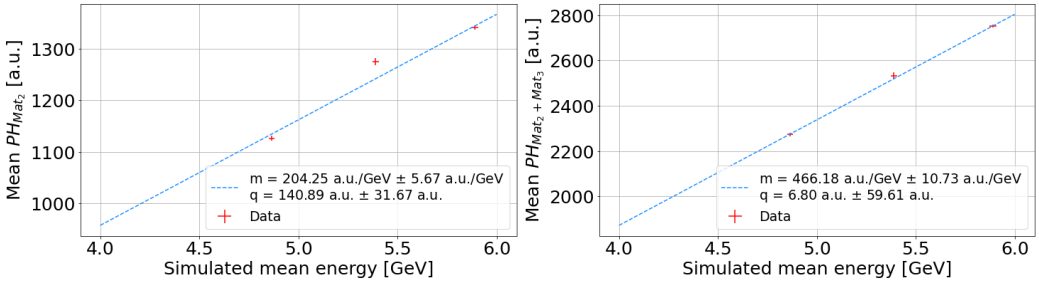

Figure 5.12: Photodetector calibration lines obtained exploiting (a) only the Mat_2 output and (b) both the Mat_2 and Mat_3 outputs, equalized and summed event by event. The line extracted parameters are listed in the boxes.

5.2.2 Energy deposit enhancement

Once the crystal lattice is aligned with the beam direction and the photodetectors are calibrated, the study on the energy deposit enhancement is performed. As already mentioned, the Strong Field effects induced by the crystal lattice, depend on the lattice-to-beam orientation and the energy deposit enhancement will be more pronounced as the misalignment angle decreases. The angular dependence of the energy deposit was studied by means of several 120 GeV long runs, performed at different goniometer angles.

[1] The reduced chi square is computed as [94] $\overline{\chi^2} = \frac{1}{N - N_p} \sum_{i=1}^{N} \frac{(y_{i,exp} - y_{i,fit})^2}{\sigma_i^2}$ where N_p is the number of the fit parameters, N the experimental points number, $y_{i,exp}$ and $y_{i,fit}$ are the experimental points and the fitted ones, and σ_i are the errors on the experimental points.

Figure 5.13(a) shows the spectra of the energy deposited in the crystal, as the misalignment angle varies; the energy deposited in the PWO sample increases as the misalignment angle approaches zero. On the other hand, the energy deposited in the calorimeter, whose spectra are shown in figure 5.13(b), behaves in the opposite way as the misalignment angle varies, which is consistent with the energy anticorrelation explained in subsection 5.2.1.

Furthermore, from figure 5.13 an anomalous behavior can be observed when the misalignment angle is 28 Θ_0, where Θ_0 indicates the Baier angle (listed in table 3.3). In fact, the mean energy, deposited in the PWO corresponding to such an angle, is larger than the one deposited at smaller misalignment angles (17 Θ_0 and 8 Θ_0). Equivalently, the mean energy deposited in the calorimeter at 28 Θ_0 is smaller than the one deposited at 17 Θ_0 and 8 Θ_0. This fact indicates that, during the angular scan, the electron beam crossed a crystal plane with a misalignment angle of 28 Θ_0.

In order to analytically compute the enhancement of the energy deposited in the PWO crystal, the spectra of the SiPMs are fitted for each misalignment angle with a crystal ball function, and the calorimeter spectra with unnormalized Gaussians. The mean values extracted from the fits are then rescaled with respect to the values corresponding to the random orientation (70 mrad), and thus the enhancement factor (e.f.) is computed. The resulting values of the e.f., with the associated propagated errors, are presented in figure 5.14; as already mentioned at 28 $\Theta_0 \sim 28$ mrad, the energy deposit enhancement shows an out-of-scale behavior due to the electron beam crossing a crystal plane, thus leading to a raising of the crystal curve.

The maximum increase in the energy deposited in the PWO sample is reached in axial orientation (0 mrad) resulting in e.f. $= 2.62 \pm 0.16$. As explained in section 2.1, the depth of the maximum energy deposit of the e.m. shower, developing within a crystal in axial orientation, is almost independent on the incident particle energy (E_0) at the GeV energy scale, while for a not oriented crystal $t_{max} \sim \log(E_0/E_c)$. For these reasons, the e.f. factor should scale as $\sim \log(E_0)$. Thus, the enhancement factor, as a function of the incident energy, can be mathematically parametrized as follows:

$$\text{e.f.}(E_0) = a \log(bE_0 + c) \tag{5.4}$$

During the beamtest, only three runs, with 80-100-120 GeV electron beams, were performed to investigate the enhancement factor as a function of the incident energy. Since equation 5.4 has three parameters (a, b and c), as well as the exploited beam energies, the fitting procedure would have zero degrees of freedom. Thus, it has been decided to use simulated data for the enhancement factor fit, whose extracted parameters are listed in table 5.1.

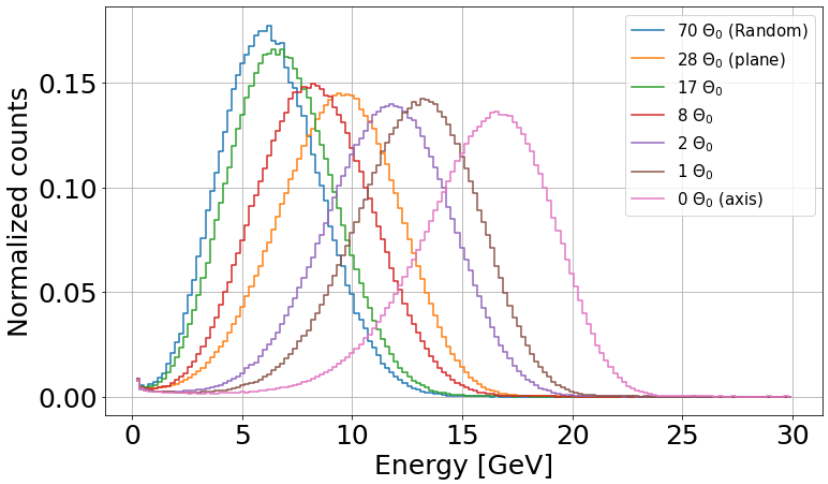

(a)

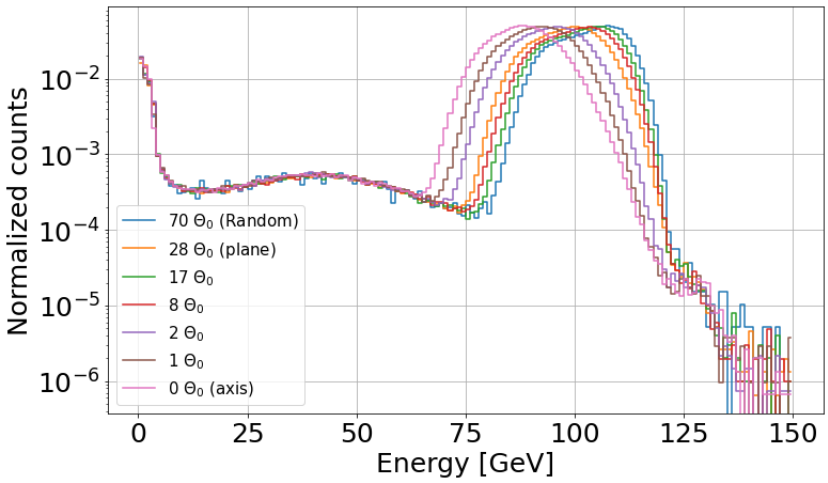

(b)

Figure 5.13: Spectra of the energy deposited in (a) the crystal and (b) the calorimeter. The different energy spectra were acquired with different misalignment angles, whose values are listed in the boxes in units of the Baier angle. All the spectra, in both the figures, are normalized in order to have unitary areas under the curves.

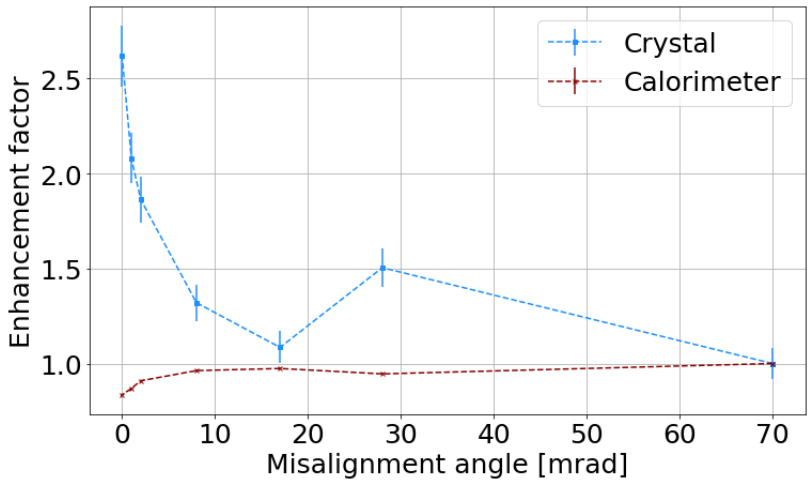

Figure 5.14: Scatter plot of the enhancement factors of the energy deposit in the crystal (light blue points) and in the calorimeter (red points), as a function of the misalignment angle.

Figure 5.15 shows the fitted curve with both experimental and simulated data; the latter are obtained reproducing the Gaussian energy spectra of the beam and the experimental setup, including the axial and the random orientations of the crystal (details in Appendix A). The fit reduced chi square is $\overline{\chi^2} = 4.4$.

Table 5.1: Enhancement factor parameters, extracted from the e.f. fitting procedure with the function defined in equation 5.4.

a	1.79 ± 0.058
b	$0.023\ \text{GeV}^{-1} \pm 0.0017\ \text{GeV}^{-1}$
c	1.91 ± 0.034

As it will be explained in the next section, the fitting procedure of e.f.(E_0) allows to numerically compute the radiation length reduction factor as a function of the incident energy. However, the introduced fit procedure of the enhancement factor, as the slightly high value of the reduced chi square ($\overline{\chi^2} \sim 4$) suggests, is based only on a semi empirical argument. This fact, and other technical aspects which will be explained in subsection 5.2.3, leads to consider another simulation based approach to estimate properly the X_0 reduction factor.

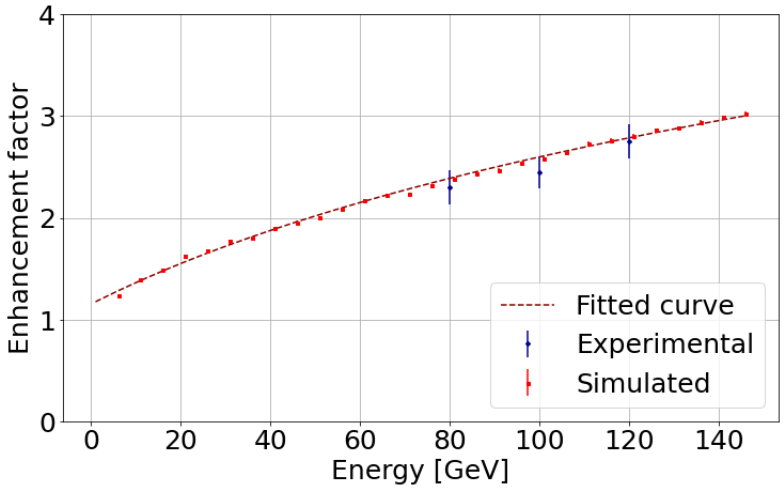

Figure 5.15: Experimental enhancement factors (blue points) and simulated ones (red points); the latter have been fitted with the function of equation 5.4.

5.2.3 The radiation length reduction

Once introduced the enhancement of the energy deposit due to the Strong Field effects, it is possible to compute the reduction of the radiation length of the crystal under test. The energy deposit enhancement within the crystal, when axially oriented, can be seen as the reduction of the PWO radiation length or, equivalently, as the stretching of the PWO thickness. The two points of view are closely related; in fact the radiation length reduction factor is defined as

$$X_0^{red}[\%] = 100 \cdot \left(\frac{L_{axial} - L_{random}}{L_{random}} \right) \tag{5.5}$$

where $L_{random} = 4.6X_0$ is the physical thickness of the crystal and L_{axial} is the equivalent thickness, expressed in units of X_0, which an impinging electron experiences when aligned with the <100> PWO axis. It has to be pointed out that this is only an estimation of the X_0 reduction, which can be accurately computed only by numerically integrating the equations of motion of the impinging particle in the crystal lattice [77, 95].

The X_0^{red} computation is performed using three different methods: a full theoretical procedure, a hybrid method which employed both theoretical aspects and simulated data, and a full simulation based approach. These methods are summarized in the following:

- **Full theoretical approach**
  The first method employs the semi empirical model (s.e.m.) of the electromagnetic shower longitudinal development. The energy deposited in matter, as a function of the longitudinal depth, can be modelled as follows [37]:

$$\frac{dE}{dt} = E_0 b^a \frac{t^{a-1} e^{-b \cdot t}}{\Gamma(a)} \tag{5.6}$$

  where E is the energy deposited in the target material, E_0 the particle initial energy, t the depth in X_0 units, a and b are model parameters depending on the target material and the incident particle type, while Γ is the gamma function[2].

  When dealing with electrons, a typical parametrization of the model parameters is [7]

$$a = \frac{1}{2}\left(1 + \log\left(\frac{E_0}{E_c}\right)\right) \tag{5.7}$$

$$b = 0.5 \tag{5.8}$$

  with E_c the $PbWO_4$ critical energy. Integrating equation 5.6, one gets the energy deposit as a function of the target thickness (t):

$$E(t) = \frac{E_0}{\Gamma(a)} \int_0^{b \cdot t} dz \; z^{a-1} e^{-z} = E_0 \gamma(a; bt) \tag{5.9}$$

  where the regularized lower incomplete gamma function $\gamma(a; bt)$ has been introduced and defined. Thus, knowing the energy deposited in the crystal (E), it is possible to compute the target thickness (t), numerically inverting equation 5.9. Similarly, once the mean energy deposited in the axially oriented PWO crystal is computed, it is possible to compute its equivalent thickness (L_{axial}), as sketched in figure 5.16, and thus the X_0^{red} factor by means of equation 5.5.

  However, this method assumes that the lateral development of the electromagnetic shower is entirely contained in the target material. This is an approximation far from reality, given the limited transverse size of the PWO crystal sample. The theoretical energy deposit curve and the simulated one, obtained reproducing the physical transverse size of the crystal and increasing progressively the longitudinal one, are compared in figure 5.17: the first curve clearly overestimates the energy deposit.

[2]The gamma function is defined as $\Gamma(z) = \int_0^\infty dt \; t^{z-1} e^{-t}$.

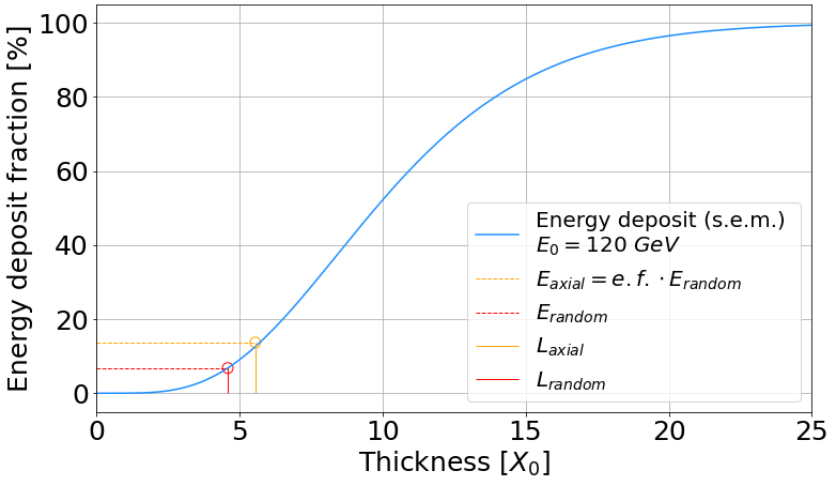

Figure 5.16: Percent energy deposit fraction, computed with the semi empirical model of equation 5.9 for a 120 GeV electron, as a function of the PWO thickness (in units of X_0). The figure presents also the computational procedure needed to obtain the X_0^{red} factor, knowing the energy deposited in the axially oriented crystal: numerically inverting the energy deposit function, L_{axial} is computed, and thus the radiation length reduction factor.

To reduce systematic errors arising from the overestimation of the energy deposit in the crystal, due to its finite transverse size, the second method is introduced.

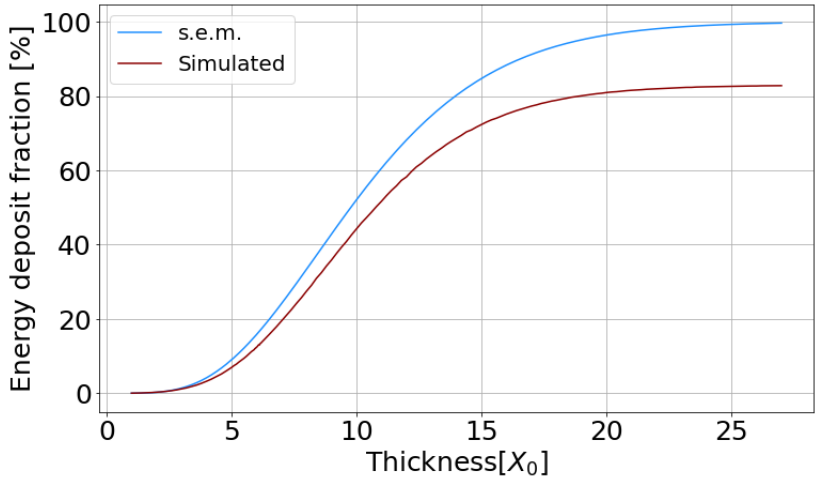

Figure 5.17: Comparison between the theoretical percent energy deposit curve (light blue solid line) and the simulated one (red solid line); the former overestimates the energy deposit, since it does not take into account the lateral energy losses due to the finite crystal transverse dimensions. Both the curves are referred to an impinging electron of 120 GeV.

- **Hybrid approach**
  The second method (e.f. method) exploits the fitted function of e.f., already shown in figure 5.15. In fact, the PWO equivalent thickness featured in axial orientation (L_{axial}) is computed numerically solving the equation

$$\text{e.f.}(E_0) = \frac{E_{axial}}{E_{random}} = \frac{\gamma(a; bL_{axial})}{\gamma(a; bL_{random})} \tag{5.10}$$

  where E_{random} and E_{axial} are the mean energy deposited in the random and axial orientation, respectively, and e.f.(E_0) is the enhancement factor as a function of the initial beam energy (E_0), whose parameters are listed in table 5.1. Thus, the radiation length reduction factor is computed using equation 5.5. This second method allows to partially mitigate the systematic errors due to the not complete transverse energy containment. As shown in the right hand side of equation 5.10, the L_{axial} computation is based on the value of the ratio between two reduced

gamma functions ($\gamma(a; bL_{axial})$ and $\gamma(a; bL_{random})$), which overestimate the energy deposit in the PWO crystal both in axial and random orientation.
Moreover, this hybrid approach, which uses the e.f. function obtained with simulated data and the s.e.m. theory, allows to obtain a numerical procedure to compute X_0^{red} as a function of the initial particle energy, as shown in figure 5.18.

- **Full simulation based approach**
  The third method (G4 method) is fully based on Monte Carlo simulations, that reproduce the energy deposit in the PWO crystal simulating all the beam and setup features, except for the PWO thickness, which was progressively increased in steps of 0.02 X_0. The performed simulations are three, with 80-100-120 GeV electron beams and with 10000 events for all the PWO thickness values. The energy deposit fraction curve is computed for each beam energy value.
  To determine the equivalent thickness of the crystal in axial orientation, and thus the X_0^{red} factor, it is sufficient to numerically solve the inverse function problem for all the three energies, as already depicted in figure 5.16.
  This method, which exploits a full simulation based approach, is considered the most reliable one, since it reproduces faithfully the transverse energy losses.

In figure 5.18 all the results, obtained with the different methods, are graphically summarized; discrepancies between the three methods are evident. The simulation based model is considered the most reliable since it reproduces the same transverse dimensions of the crystal and, therefore, the lateral energy loss that occurs experimentally. The semi empirical model is the one that differs the most from the G4 method, while the e.f. method features a smaller discrepancy from the full simulation based approach, due to the partial suppression of systematic errors thanks to the ratio of the right hand side of equation 5.10. Moreover, as far as the e.f. method is concerned, it has to be noticed that the predicted reduction length factor is different from 0% when the impinging energy approaches zero (figure 5.18). This is due to the fact that the fitted curve of figure 5.15, based on a semi empirical argument, predicts an enhancement factor different from 1 when the initial particle energy is zero, thus pointing out that this model is not reliable in the low energy range.

Table 5.2 summarizes the equivalent radiation length values obtained in axial orientation (L_{axial}) and the radiation length reduction factors (X_0^{red}),

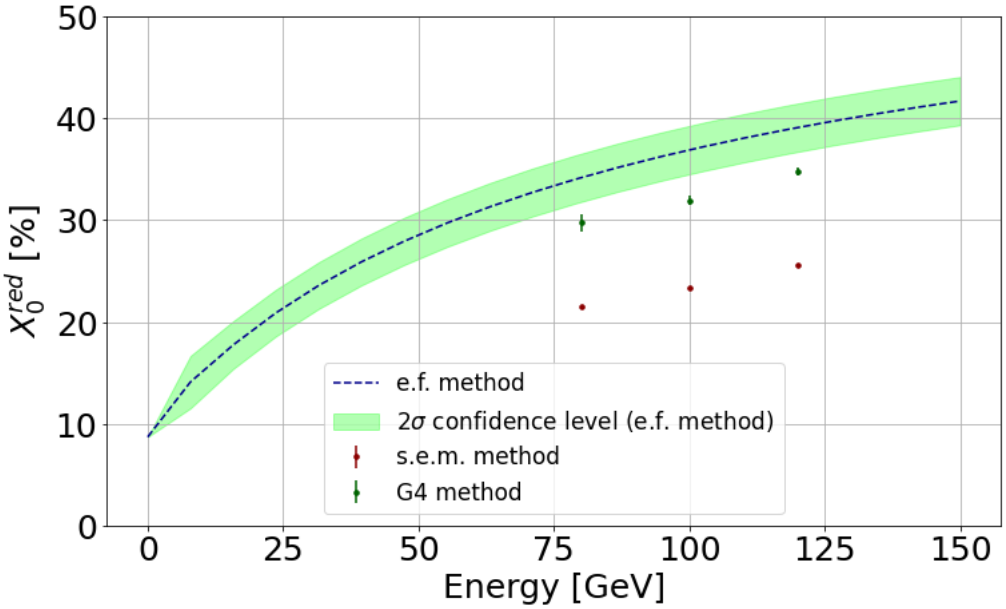

Figure 5.18: Comparison between the three different methods used to compute the X_0^{red} factor: the G4 method points are represented in green, the s.e.m. method ones in red while the e.f. method function is represented in blue with its confidence level highlighted in light green.

obtained with the G4 method; the computed values are in agreement with the results reported in [6] (i.e. $X_0^{red} \sim 35\%$, for a 120 GeV electron beam).

Table 5.2: Main experimental results obtained for three different beam energies.

Parameters	80 GeV	100 GeV	120 GeV
L_{axial} $[X_0]$	5.97 ± 0.04	6.07 ± 0.02	6.2 ± 0.02
L_{axial} [mm]	53.15 ± 0.36	53.86 ± 0.18	54.93 ± 0.18
X_0^{red} [%]	29.78 ± 0.87	31.96 ± 0.43	34.78 ± 0.43

Previous studies, performed in the framework of the AXIAL and ELIOT collaborations, demonstrated that $X_0^{red} \sim 65\%$ for a $0.45X_0$ $PbWO_4$ crystal sample, as reported in [6], thus confirming that the shorter the crystal under test, the greater the relative increase in the energy deposit and therefore the X_0^{red} factor. This fact is in perfect agreement with the theory, as explained in section 2.1, because the secondary particles of the electromagnetic shower, after the first radiation lengths, have angles extending beyond the SF angular acceptance, and thus they are progressively less affected by the Strong Field effects. However, this particular aspect must not be misunderstood: in the next-generation oriented crystal based calorimeters, only the first radiation lengths will be deeply influenced by the lattice-to-beam orientation, but this is not in contrast with the fact that the crystal based technology will feature better performances in terms of energy containment with respect to the not oriented one.

These observations conclude the characterization of the Strong Field effects in the studied PWO crystal samples.

Conclusions

This thesis work has been performed in the framework of the *STORM* project, which aimed at investigating the Strong Field effects induced by the $PbWO_4$ crystalline structure. It is well known since the 1950s that the crystal lattice may strongly modify both the pair production cross section and the bremsstrahlung emission spectrum. In the first chapter of this thesis, a comprehensive theoretical treatment has been provided on how the crystal lattice influences the charged particles trajectory and on how the radiation emission of electrons and the pair production processes of photons undergo modifications in oriented crystals. It has been shown that, in the Strong Field regime, the bremsstrahlung emission spectrum of an ultra relativistic light charged particle (such as an electron or a positron) is strongly modified by the lattice coherent effects and that its spectral features depend on the impinging particle incidence angle. It has been demonstrated that electrons (or positrons) impinging on a crystallographic direction with incidence angles smaller than the Baier one (Θ_0), emit synchrotron radiation peaked in the hard part of the spectrum, thus leading to an enhancement in the energy deposit with respect to the amorphous case.

The coherent effects induced by the lattice structures make the oriented crystals technology appealing for the development of next-generation compact electromagnetic calorimeters, which will exploit the e.m. showers acceleration to improve the current-generation calorimeters performances in terms of energy containment, as explained in the second chapter.

In order to estimate properly the acceleration of the electromagnetic shower development, that can be seen also in terms of the radiation length reduction, within a $4.6X_0$ PWO sample, efficient photodetectors reading out the crystal scintillation light are needed. The photodetection system implemented during the *STORM 2022* beamtest was based on Silicon PhotoMultipliers, consisting of four SiPM matrices model ARRAYC-60035-4P-BGA, as explained in the third chapter. During the 2022 beamtest, which took place on the CERN H2 extracted beamline, the PWO light output was studied as a function of the lattice-to-beam orientation of the sample, monitored by means of

a remotely controlled high-precision goniometer. Moreover, the particle incidence angles were computed with a high accuracy thanks to the high precision and high spatial resolution tracking system, composed by two silicon microstrip telescopes with a spatial resolution of a few microns. The energy deposited in the crystal sample was evaluated by means of the SiPM readout system, while the downstream calorimeter, composed by 7 lead glasses, measured the remaining energy.

Before characterizing the PWO behavior in the Strong Field condition, the main beam features, such as the angular divergence and the beam composition, have been analyzed in the fourth chapter, as well as the calorimeter performances in terms of energy resolution. The best angular divergence values were obtained using the 120 GeV electron beams and their values are $\sigma_x = 97.22\,\mu\text{rad} \pm 0.47\,\mu\text{rad}$ along the x direction and $\sigma_y = 71.19\,\mu\text{rad} \pm 0.35\,\mu\text{rad}$ along the y direction, which are one order of magnitude smaller than the Strong Field angular acceptance ($\Theta_0 \sim 1\,\text{mrad}$), and thus suitable to perform the PWO characterization in the SF regime.

Finally, as discussed in the fifth chapter, the PWO behavior was analyzed as a function of the lattice-to-beam orientation. In the first phase of the PWO characterization, the sample alignment procedure was performed: it consists in a first manual pre-alignment, which guarantees an angular accuracy of few mrad, followed by a more precise software alignment, performed analyzing the SiPM output as the goniometer angular degrees of freedom vary. This offline analysis allows to compute the reference axis (<100> in this thesis) angular coordinates. The SiPM output was studied also as a function of the impinging particle misalignment angles; this analysis outlined the presence of the crystal planes, included the skew ones.

The energy deposit in the PWO was studied during the transition from the random to the axial orientation; this angular scan revealed the presence of a plane corresponding to $28\Theta_0$ of the misalignment angle.

The electromagnetic shower acceleration due to the Strong Field effects was analytically quantified computing the reduction of the radiation length, using three different approaches. The most reliable one was a full simulation based approach, that exploited the energy deposit curve simulated using the Geant4 toolkit [42], a Monte Carlo simulation tool which supported the entire data analysis.

The main result of this thesis consists in the computation of the X_0 reduction factor; it turned to be $\sim 35\%$ in the case of a 120 GeV electron beam, which is consistent with the results reported in [6]. This result confirms the acceleration in the electromagnetic shower development in oriented crystals, thus validating the feasibility of the compact electromagnetic calorimeter development.

The future perspective of this work is the development of an electromagnetic calorimeter prototype with a layer of oriented $PbWO_4$ crystals for the shower acceleration and the particle identification. These studies and data analyses are being performed by the OREO collaboration, which anticipated very promising results, despite they are not yet published.

Appendix A

Geant4 Simulations

The simulation of the energy deposit in the $PbWO_4$ crystal was performed using the Geant4 toolkit [42]; the FTFP_BERT physics list [96] was employed for random simulations. However, the Strong Field effects are not included in any Geant4 physics list, thus a different approach is needed to perform the simulations in axial orientation. In order to achieve such a task, the correction coefficients to the standard e.m. cross sections, taking into account the lattice contributions to the electromagnetic processes, were computed following the steps outlined by [6, 97], and the electromagnetic cross sections were rescaled by these factors.

The simulated experimental setup featured a simplified geometry, reproducing only the active areas of the detectors, without the mechanical supports and the light-tight layers. On the other hand, the simulated geometrical beam features, listed in table A.1, reproduced the experimental ones.

Table A.1: Geometrical features of the simulated beams for three different energies.

Parameters	80 GeV	100 GeV	120 GeV
Transverse plane distribution	Rectangular	Rectangular	Rectangular
L_x [cm]	0.5 cm	0.5 cm	0.5 cm
L_y [cm]	0.5 cm	0.5 cm	0.5 cm
Angular distribution	Gaussian	Gaussian	Gaussian
σ_x [µrad]	126.74	121.18	97.12
σ_y [µrad]	86.72	77.95	71.22

As far as the simulated beam energy spectra are concerned, most of the simulations were performed reproducing the shape of the electron part of the calorimeter energy distributions, acquired during the calibration runs, by means of the Geant4 hist command [91]. Moreover, 3% of the total number

of events was composed by mono energetic negative pions. However, since the limited number of calibration runs (6), the experimental electron part of the energy spectra was available only for energies in the $20 - 120$ GeV range, in steps of 20 GeV. Thus, whenever it was necessary to simulate an energy scan, it was chosen to use a beam consisting of only electrons, with a Gaussian energy spectrum, featuring a σ/μ ratio of 2%.

The energy deposited in the crystal was simulated by reproducing the energy loss physical processes, but, for simplicity, not the scintillation light production and propagation, nor the SiPM readout chain. Figure A.1 shows the experimental and the simulated spectra of the energy deposited in the crystal sample, obtained with two different beam energies (100 GeV and 120 GeV), both in random and in axial orientation: in the former orientation the simulated spectra reproduce faithfully the experimental ones, while in the latter orientation the experimental and the simulated spectra are slightly different. In order to quantify the discrepancy between the simulated and the experimental energy distribution, the Kullback-Leibler divergences (mathematical details are provided in section 4.3) have been computed both in random and axial orientation. The statistical divergence values are listed in table A.2; for both the beam energy values the divergence computed in the axial orientation is an order of magnitude larger than the one obtained in the random configuration.

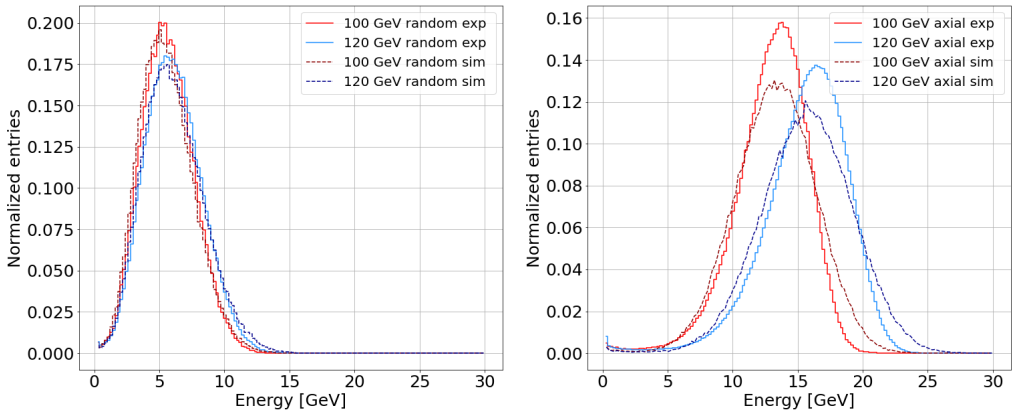

Figure A.1: Experimental and simulated spectra of the energy deposited in the $4.6X_0$ $PbWO_4$ crystal sample with 100 GeV and 120 GeV impinging electron beams, in (a) random orientation and (b) axial orientation.

The increasing statistical divergence in axial orientation is probably due to the not perfect simulation procedure. In fact, axial simulations were performed only rescaling the cross sections of electromagnetic processes by

Table A.2: Computed Kullback-Leibler divergences for two different energies (100 GeV and 120 GeV), in random and axial orientation.

Beam energy [GeV]	Orientation	K-L divergence
100	Random	0.0063
100	Axial	0.02
120	Random	0.0054
120	Axial	0.024

factors which take into account the lattice-to-beam alignment. Potential future improvements of the simulation code would consist in:

- reproducing the crystal lattice and thus the interatomic potential wells, and not only the correction factors to the standard e.m. cross sections;
- implementing the light generation and propagation processes, occurring when a particle impinges on the crystal.

Acronym list

ADC	Analog to Digital Converter
ASIC	Application Specific Integrated Circuit
AXIAL	AXIAL and quasi-axial coherent interaction between charged particle beams and crystal
BGA	Ball Grid Array
CB	Coherent Bremsstrahlung
CERN	Conseil Europeen pour la Recherche Nucleaire
CFA	Constant Field Approximation
CMOS	Complementary Metal Oxide Semiconductor
COG	Center Of Gravity
COMPASS	COmmon Muon Proton Apparatus for Structure and Spectroscopy
CR	Channeling Radiation
DAC	Digital to Analog Converter
DAQ	Data AcQuisition
e+ BOOST	intense positron source Based On Oriented crySTals
ELIOT	ELectromagnetic processes In Oriented crysTals
FCC	Face Centered Cubic
FCC	Future Circular Collider
G4	Geant4
HDF5	Hierarchical Data Format 5
HRXRD	High-Resolution X-Ray Diffractometer
ID	IDentification

INFN	Istituto Nazionale di Fisica Nucleare
LAT	Large Area Telescope
LEP	Large Electron-Positron collider
LHC	Large Hadron Collider
LINAC	LINear ACcelerator
LPM	Landau-Pomeranchuk-Migdal
NA62	North Area 62 experiment
OPAL	Omni-Purpose Apparatus for LEP
OREO	ORiEnted calOrimeter
PC	Personal Computer
PDE	Photo Detection Efficiency
PH	Pulse Height
PMT	PhotoMultiplier Tube
PS	Proton Synchrotron
PSB	Proton Synchrotron Booster
QE	Quantum Efficiency
RAM	Random Access Memory
SB	Standard Bremsstrahlung
SF	Strong Field
SFPP	Strong Field Pair Production
SiPM	Silicon PhotoMultiplier
SLAC	Stanford Linear ACcelerator
SLC	SLAC Linear Collider
SM	Standard Model
SPAD	Single Photon Avalanche Diode
SPS	Super Proton Synchrotron
SPP	Standard Pair Production
STORM	STrOng cRystalline electroMagnetic field
UF	Ultra Fast
VME	Versabus Module Eurocard
VRB	VME Readout Board

List of Figures

List of Tables

Bibliography

[1] J. Lindhard. "Influence of crystal lattice on motion of energetic charged particles". In: *Kongel. Dan. Vidensk. Selsk., Mat.-Fys. Medd.* (1965). URL: https://www.osti.gov/biblio/4536390.

[2] V. N. Baier, V. M. Katkov, and V. M. Strakhovenko. *Electromagnetic Processes at High Energies in Oriented Single Crystals*. 1998. URL: https://www.worldscientific.com/doi/abs/10.1142/2216.

[3] J. U. Andersen, E. Bonderup, and R. H. Pantell. "Channeling Radiation". In: *Annual Review of Nuclear and Particle Science* 33.1 (1983), pp. 453–504. URL: https://doi.org/10.1146/annurev.ns.33.120183.002321.

[4] C. Kittel. *Introduction to Solid State Physics*. 8th ed. Wiley, 2004. ISBN: 9780471415268. URL: https://www.wiley.com/en-us/Introduction+to+Solid+State+Physics%2C+8th+Edition-p-9780471415268.

[5] A. Selmi. "Electromagnetic Shower Development in Oriented Crystals". Master Thesis. Insubria University, 2022. URL: https://cds.cern.ch/record/2814582.

[6] M. Soldani. "Innovative applications of strong crystalline field effects to particle accelerators and detectors". PhD Thesis. Ferrara University, 2023. URL: https://cds.cern.ch/record/2864634.

[7] Particle Data Group et al. "Review of Particle Physics". In: *Progress of Theoretical and Experimental Physics* 2022.8 (Aug. 2022), p. 083C01. ISSN: 2050-3911. URL: https://doi.org/10.1093/ptep/ptac097.

[8] M. Romagnoni et al. "Bent Crystal Design and Characterization for High-Energy Physics Experiments". In: *Crystals* 12 (Sept. 2022), p. 1263. DOI: 10.3390/cryst12091263.

[9] D. Bolognini. "Study of channeling phenomena in bent crystals: the new frontiers". Master Thesis. Insubria University, 2008. URL: https://cds.cern.ch/record/1143063.

[10] L. Bandiera et al. "Strong Reduction of the Effective Radiation Length in an Axially Oriented Scintillator Crystal". In: *Phys. Rev. Lett.* 121 (2 July 2018), p. 021603. URL: https://link.aps.org/doi/10.1103/PhysRevLett.121.021603.

[11] H. Kumm et al. "Rosette motion and string scattering of 20 MeV electrons in MgO single crystals". In: *Radiation Effects* 12.1-2 (Jan. 1972), pp. 53–61. DOI: 10.1080/00337577208231121.

[12] B. R. Appleton et al. "Hyperchanneling, an Axial Channeling Phenomenon". In: *Phys. Rev. Lett.* 28 (20 May 1972), pp. 1307–1311. URL: https://link.aps.org/doi/10.1103/PhysRevLett.28.1307.

[13] V. M. Biryukov, Yu. A. Chesnokov, and V. I. Kotov. *Crystal channeling and its application at high-energy accelerators*. 1997. ISBN: 978-3-642-08238-2.

[14] H. Bethe and W. Heitler. "On the Stopping of Fast Particles and on the Creation of Positive Electrons". In: *Proceedings of the Royal Society of London Series A* 146.856 (Aug. 1934), pp. 83–112. DOI: 10.1098/rspa.1934.0140.

[15] K. Nakamura et al. "Review of particle physics". In: *J. Phys. G* 37 (2010), p. 075021. DOI: 10.1088/0954-3899/37/7A/075021.

[16] H. D. Thomsen et al. "On the macroscopic formation length for GeV photons". In: *Physics Letters B* 672.4 (2009), pp. 323–327. ISSN: 0370-2693. URL: https://www.sciencedirect.com/science/article/pii/S0370269309001026.

[17] V. N. Baier and V. M. Katkov. "Concept of formation length in radiation theory". In: *Physics Reports* 409.5 (2005), pp. 261–359. ISSN: 0370-1573. URL: https://www.sciencedirect.com/science/article/pii/S0370157304005083.

[18] U. I. Uggerhøj. "The interaction of relativistic particles with strong crystalline fields". In: *Rev. Mod. Phys.* 77 (4 Oct. 2005), pp. 1131–1171. URL: https://link.aps.org/doi/10.1103/RevModPhys.77.1131.

[19] P. L. Anthony et al. *An accurate measurement of the Landau-Pomeranchuk-Migdal effect*. Tech. rep. Berkeley, CA: Lawrence Berkeley Nat. Lab., 1995. URL: https://cds.cern.ch/record/284766.

[20] J. U. Andersen et al. "Axial channeling radiation from MeV electrons". In: *Nuclear Instruments and Methods in Physics Research* 194.1 (1982), pp. 209–224. ISSN: 0167-5087. URL: https://www.sciencedirect.com/science/article/pii/0029554X82905171.

[21] D. F. Alferov et al. "The ondulator as a source of electromagnetic radiation". In: *Part. Accel.* 9 (1979), pp. 223–236.

[22] F. Meot. "Low-frequency wiggler radiation". In: *Proceedings of the 1999 Particle Accelerator Conference (Cat. No.99CH36366)*. Vol. 4. 1999, 2445–2446 vol.4. DOI: 10.1109/PAC.1999.792719.

[23] H. Wiedemann. "Overview of Synchrotron Radiation". In: *Particle Accelerator Physics*. Cham: Springer International Publishing, 2015, pp. 815–855. ISBN: 978-3-319-18317-6. URL: https://doi.org/10.1007/978-3-319-18317-6_24.

[24] J. Schwinger. "The quantum correction in the radiation by energetic accelerated electrons". In: *Proceedings of the National Academy of Sciences* 40.2 (1954), pp. 132–136. URL: https://www.pnas.org/doi/abs/10.1073/pnas.40.2.132.

[25] A. H. Sorensen and E. Uggerhøj. "Channelling and channelling radiation". In: *Nature* 325 (Jan. 1987), pp. 311–318. DOI: 10.1038/325311a0.

[26] J. U. Andersen. "Channeling radiation and coherent bremsstrahlung". In: *Nuclear Instruments and Methods* 170.1 (1980), pp. 1–5. ISSN: 0029-554X. URL: https://www.sciencedirect.com/science/article/pii/0029554X80909763.

[27] J. T. Cremer. "Chapter 3 - Neutron Scatter Physics and Differential Cross Sections". In: *Advances in Imaging and Electron Physics*. Vol. 173. Advances in Imaging and Electron Physics. Elsevier, 2012, pp. 167–274. URL: https://www.sciencedirect.com/science/article/pii/B9780123969699000033.

[28] N. W. Ashcroft and N. D. Mermin. *Solid State Physics*. Saunders College Publishing, 1976.

[29] L. D. Landau and E. M. Lifschits. *The Classical Theory of Fields*. Vol. Volume 2. Course of Theoretical Physics. Oxford: Pergamon Press, 1975. ISBN: 978-0-08-018176-9.

[30] G. V. Dunne. *The Schwinger Effect: non-perturbative particle production from vacuum*. URL: https://dunne.physics.uconn.edu/dunne-schwinger/.

[31] G. V. Dunne. "New Strong-Field QED Effects at ELI: Nonperturbative Vacuum Pair Production". In: *Eur. Phys. J. D* 55 (2009), pp. 327–340. DOI: 10.1140/epjd/e2009-00022-0. arXiv: 0812.3163 [hep-th].

[32] R. Ruffini, G. Vereshchagin, and S. Xue. "Electron-positron pairs in physics and astrophysics: From heavy nuclei to black holes". In: *Physics Reports* 487.1 (2010), pp. 1–140. ISSN: 0370-1573. URL: https://www.sciencedirect.com/science/article/pii/S0370157309002518.

[33] C. M. Kim and S. P. Kim. *Magnetars as Laboratories for Strong Field QED*. 2021. arXiv: 2112.02460 [astro-ph.HE].

[34] ATLAS Collaboration. *ATLAS observes light scattering off light: New result studies photons interacting at high energies*. URL: https://atlas.cern/updates/briefing/atlas-observes-light-scattering-light.

[35] M. Soldani et al. "Next-generation ultra-compact calorimeters based on oriented crystals". In: *PoS* ICHEP2020 (2021), p. 872. DOI: 10.22323/1.390.0872.

[36] A. H. Sørensen. "Channeling, bremsstrahlung and pair creation in single crystals". In: *Nuclear Instruments and Methods in Physics Research Section B: Beam Interactions with Materials and Atoms* 119.1 (1996), pp. 2–29. ISSN: 0168-583X. URL: https://www.sciencedirect.com/science/article/pii/0168583X96003497.

[37] C. W. Fabjan and F. Gianotti. "Calorimetry for particle physics". In: *Reviews of modern physics* 75 (Oct. 2003). URL: https://cds.cern.ch/record/692252/files/RevModPhys.75.1243.pdf.

[38] M. Soldani et al. "Strong enhancement of electromagnetic shower development induced by high-energy photons in a thick oriented tungsten crystal". In: *Physical Journal* (2023). URL: https://link.springer.com/article/10.1140/epjc/s10052-023-11247-x.

[39] B. Ferretti. "Sulla "Bremsstrahlung" nei cristalli". In: *Il Nuovo Cimento* 7 (Mar. 1950), pp. 118–134. DOI: https://doi.org/10.1007/BF02781144.

[40] H. Uberall. "High-Energy Interference Effect of Bremsstrahlung and Pair Production in Crystals". In: *Phys. Rev.* 103 (4 Aug. 1956), pp. 1055–1067. URL: https://link.aps.org/doi/10.1103/PhysRev.103.1055.

[41] L. Bandiera et al. "Strong Reduction of the Effective Radiation Length in an Axially Oriented Scintillator Crystal". In: *Phys. Rev. Lett.* 121 (2 July 2018), p. 021603. URL: https://link.aps.org/doi/10.1103/PhysRevLett.121.021603.

[42] *Geant4 Toolkit for the simulation of the passage of particles through matter*. URL: https://geant4.web.cern.ch/.

[43] L. Bandiera et al. "Crystal-based pair production for a lepton collider positron source". In: *The European Physical Journal C* 82.8 (Aug. 2022). ISSN: 1434-6052. URL: http://dx.doi.org/10.1140/epjc/s10052-022-10666-6.

[44] X. Artru et al. "Advantages of axially aligned crystals used in positron production at future linear colliders". In: *Physical Review Special Topics - Accelerators and Beams* 6.9 (Sept. 2003). ISSN: 1098-4402. URL: http://dx.doi.org/10.1103/PhysRevSTAB.6.091003.

[45] V. K. Bharadwaj et al. "Analysis of beam induced damage to the SLC positron production target". In: *Conf. Proc. C* 0106181 (2001). Ed. by Peter W. Lucas and Sara Webber, pp. 2123–2125.

[46] CERN. *Future Circular Collider*. URL: https://home.cern/science/accelerators/future-circular-collider.

[47] M. Soldani et al. "Radiation in oriented crystals: Innovative application to future positron sources". In: *Nuclear Instruments and Methods in Physics Research Section A: Accelerators, Spectrometers, Detectors and Associated Equipment* 1058 (Jan. 2024), p. 168828. ISSN: 0168-9002. URL: http://dx.doi.org/10.1016/j.nima.2023.168828.

[48] E. Cortina Gil et al. *HIKE, High Intensity Kaon Experiments at the CERN SPS*. URL: https://arxiv.org/abs/2211.16586.

[49] L. Bandiera. *OREO*. URL: https://www.fe.infn.it/index.php/it/?view=article&id=602:oreo&catid=88.

[50] NASA. *Large Area Telescope (LAT)*. URL: https://fermi.gsfc.nasa.gov/science/instruments/lat.html.

[51] NASA. *Fermi Gamma-ray Space Telescope*. URL: https://fermi.gsfc.nasa.gov/.

[52] NASA. *Fermi*. URL: https://science.nasa.gov/mission/fermi/.

[53] L. Bandiera. "Novel type of compact satellite borne gamma-ray telescope based on oriented crystals". In: URL: https://agenda.infn.it/event/14929/contributions/27509/contribution.pdf.

[54] CERN. *CERN accelerator complex*. URL: https://home.cern/science/accelerators/accelerator-complex.

[55] C. Pralavorio. *LS2 Report: Focus on the North Area*. URL: https://home.cern/news/news/engineering/ls2-report-focus-north-area.

[56] N. Charitonidis and B. Rae. *The H2 Secondary Beam Line of EHN1/SPS*. URL: https://sba.web.cern.ch/sba/BeamsAndAreas/H2/H2_presentation.html.

[57] CSEM. *CSEM website*. URL: https://www.csem.ch/en/.

[58] E. Lund et al. *Treatment of energy loss and multiple scattering in the context of track parameter and covariance matrix propagation in continuous material in the ATLAS experiment*. Tech. rep. Geneva: CERN, 2008. URL: https://cds.cern.ch/record/1114577.

[59] INFN sezione Perugia. *Silicon Strip Detectors in Physics: From Nuclear Physics to Space Applications*. URL: https://indico.cern.ch/event/1223972/contributions/5262055/attachments/2602916/4495470/silvestre_TREDI2023.pdf.

[60] D. Lietti. "VISION: a Versatile and Innovative SIlicOn tracking system". PhD Thesis. Insubria University, 2015. URL: https://cds.cern.ch/record/2626151.

[61] IDEAS. *IDEAS website*. URL: https://ideas.no/.

[62] Analog Devices. *Analog Devices*. URL: https://www.analog.com/en/index.html.

[63] P. Musico. *Introduzione al bus industriale vme*. URL: https://www.ge.infn.it/~musico/Vme/VME_Torino.pdf.

[64] PDG. *Atomic and nuclear properties of lead tungstate*. URL: https://pdg.lbl.gov/2020/AtomicNuclearProperties/HTML/lead_tungstate.html.

[65] *VESTA: Visualization for Electronic and STructural Analysis*. URL: https://jp-minerals.org/vesta/en/.

[66] S. Gundacker and A. Heering. "The Silicon PhotoMultiplier: Fundamentals and applications of a modern solid-state photon detector". In: *Physics in Medicine and Biology* 65 (Aug. 2020). DOI: 10.1088/1361-6560/ab7b2d.

[67] *Silicon PhotoMultipliers*. URL: https://sites.gatech.edu/lanns/research/silicon-photomultipliers/.

[68] S. S. Piatek. *SiPM and SPAD: Emerging Applications for Single-Photon Detection*. URL: https://www.hamamatsu.com/content/dam/hamamatsu-photonics/sites/static/hc/resources/SiPM_SPAD_%20Emerging_Applications.pdf.

[69] S. Piatek. *What is a SiPM and how does it work?* URL: https://hub.hamamatsu.com/us/en/technical-notes/mppc-sipms/what-is-an-SiPM-and-how-does-it-work.html.

[70] P. Eckert et al. "Characterisation studies of Silicon PhotoMultipliers". In: *Nuclear Instruments and Methods in Physics Research Section A: Accelerators, Spectrometers, Detectors and Associated Equipment* 620.2-3 (Aug. 2010), pp. 217–226. ISSN: 0168-9002. URL: http://dx.doi.org/10.1016/j.nima.2010.03.169.

[71] M. R. Hampel et al. "Optical crosstalk in SiPMs". In: *Nuclear Instruments and Methods in Physics Research Section A: Accelerators, Spectrometers, Detectors and Associated Equipment* 976 (2020), p. 164262. ISSN: 0168-9002. URL: https://www.sciencedirect.com/science/article/pii/S0168900220306586.

[72] G. Collazuol. *The SiPM Physics and Technology - a Review*. URL: https://indico.cern.ch/event/164917/contributions/1417121/attachments/198512/278663/PhotoDet12_-_collazuol_-_v3.pdf.

[73] *Silicon PhotoMultiplier (SiPM) 4-Side Scaleable Arrays*. URL: https://www.mouser.it/datasheet/2/308/ARRAYC_SERIES_D-2309928.pdf.

[74] *ONSEMI website*. URL: https://www.onsemi.com/.

[75] *Silicon PhotoMultipliers (SiPM), Low-Noise, Blue-Sensitive*. URL: https://www.onsemi.com/pdf/datasheet/microc-series-d.pdf.

[76] *L'ARTE nella Micro Elettronica Electronic Manufacturing Services Original Device Manufacturing Prototyping HiTech PCB Assembly X-ray 3D Service Professional Led Lighting IOT (Internet Of Things) solutions*. URL: https://www.scen.it/.

[77] P. Monti-Guarnieri. "Beamtest characterization of oriented crystals for the KLEVER Small Angle Calorimeter". Master Thesis. Insubria University, 2023. URL: https://cds.cern.ch/record/2850897.

[78] CERN. *The OPAL detector on the Large Electron-Positron collider delivered key measurements of Z and W bosons in its 11-year lifetime*. URL: https://home.cern/science/experiments/opal.

[79] C. Luo et al. "Cerenkov Radiation in Photonic Crystals". In: *Science (New York, N.Y.)* 299 (Feb. 2003), pp. 368–71. DOI: 10.1126/science.1079549.

[80] F. Ambrosino et al. "The large-angle photon veto system for the NA62 experiment at the CERN SPS". In: *Journal of Physics: Conference Series* 404.1 (Dec. 2012), p. 012022. DOI: 10.1088/1742-6596/404/1/012022. URL: https://dx.doi.org/10.1088/1742-6596/404/1/012022.

[81] HAMAMATSU. *PhotoMultiplier tube R9880U SERIES*. URL: https://www.hamamatsu.com/content/dam/hamamatsu-photonics/sites/documents/99_SALES_LIBRARY/etd/R9880U_TPMH1321E.pdf.

[82] PDG. *Atomic and nuclear properties of lead glass*. URL: https://pdg.lbl.gov/2020/AtomicNuclearProperties/HTML/lead_glass.html.

[83] CAEN. *DT5730 / DT5730S*. URL: https://www.caen.it/products/dt5730/.

[84] CAEN. *V1724*. URL: https://www.caen.it/products/v1724/.

[85] G. Landi. "Properties of the center of gravity as an algorithm for position measurements". In: *Nuclear Instruments and Methods in Physics Research Section A: Accelerators, Spectrometers, Detectors and Associated Equipment* 485 (June 2002), pp. 698–719. DOI: 10.1016/S0168-9002(01)02071-X.

[86] *HDF5*. URL: https://docs.hdfgroup.org/hdf5/develop/_intro_h_d_f5.html.

[87] *NumPy*. URL: https://numpy.org/.

[88] *Matplotlib*. URL: https://matplotlib.org/.

[89] *SciPy*. URL: https://scipy.org/.

[90] *Geant4 Material Database*. URL: https://geant4-userdoc.web.cern.ch/UsersGuides/ForApplicationDeveloper/html/Appendix/materialNames.html#g4matrdb.

[91] *Primary particle commands*. URL: https://g4see-docs.web.cern.ch/master/macro_primaries.html.

[92] D. Belov and R. Armstrong. "Distributions of the Kullback-Leibler divergence with applications". In: *The British journal of mathematical and statistical psychology* 64 (May 2011), pp. 291–309. DOI: 10.1348/000711010X522227.

[93] D. Souvik. *A simple alternative to the Crystal Ball function*. 2016. eprint: 1603.08591. URL: https://arxiv.org/abs/1603.08591.

[94] J. R. Taylor. *An Introduction to Error Analysis. The Study of Uncertainties in Physical Measurements, Third Edition*. University Science Books,U.S., 2022. ISBN: 1940380146.

[95] A. I. Sytov, V. V. Tikhomirov, and L. Bandiera. "Simulation code for modeling of coherent effects of radiation generation in oriented crystals". In: *Phys. Rev. Accel. Beams* 22 (6 June 2019), p. 064601. DOI: 10.1103/PhysRevAccelBeams.22.064601.

[96] *FTFP_BERT*. URL: https://geant4-userdoc.web.cern.ch/UsersGuides/PhysicsListGuide/html/reference_PL/FTFP_BERT.html.

[97] V. Baryshevsky et al. "On the influence of crystal structure on the electromagnetic shower development in the lead tungstate crystals". In: *Nuclear Instruments and Methods in Physics Research Section B: Beam Interactions with Materials and Atoms* 402 (Mar. 2017). DOI: 10.1016/j.nimb.2017.02.066.